Studies on $AO\text{-}Bi_2O_3\text{-}V_2O_5$ (A = Mg, Ca, Sr, Ba) ceramics as electrolytes

Thesis submitted in partial fulfillment of the

requirement of the degree of

DOCTOR OF PHILOSOPHY

by

Sakshi Gupta
Regn. No. (901112012)

Under the Supervision of

Dr. K. Singh
Professor

School of Physics and Materials Science

Thapar University, Patiala (Punjab) India- 147004

(Declared as Deemed-to-be-University u/s of the UGC act, 1956)

December-2015

Dedicated to
my parents

CERTIFICATE

This is to certify that the thesis entitled **"Studies on AO-Bi_2O_3-V_2O_5 (A = Mg, Ca, Sr, Ba) ceramics as electrolytes"** which is being submitted by Sakshi Gupta in partial fulfilment of the requirements for the award of the degree of Doctor of Philosophy in School of Physics and Materials Science, Thapar University, Patiala (Punjab), India is an exclusive record of candidate's own research work under my guidance and supervision. The thesis in part or in full has not been submitted in any other university or institute for the award of any degree. The thesis is fit to be considered for the award of degree of Doctor of Philosophy.

Dr. K. Singh
Professor
School of Physics and Materials Science
Associate Dean Strategy
Thapar University, Patiala-147004 (INDIA)

Date: December 4, 2015

Acknowledgement

This thesis is the end of my journey in obtaining Ph.D. At the end of thesis I would like to thank all those people who made this thesis possible and an unforgettable experience for me. I would like to express my deepest gratitude to my advisor, Dr. K. Singh, Professor and Associate Dean Strategy, Thapar University Patiala for his excellent guidance, caring, patience and providing me with an excellent atmosphere for doing research.

I am highly thankful to Dr. O.P. Pandey Senior Professor, Dean Research and Sponsored Projects for providing me valuable advice and insight throughout my work. I am very thankful to my doctoral committee members Dr. B. N. Chudasama, Dr. Poonam Uniyal, Dr. Susheel Mittal for their guidance, suggestions and support during my six months progress report. My special thanks are also due to all the respective faculty of School of Physics and Materials Science, Dr. K.K. Raina, Dr. N.K. Verma, Dr. M.K. Sharma, Dr. Puneet Sharma, Dr. Suneel Kumar, Dr. S.D. Tiwari, Dr. D.P. Singh, Ms. Loveleen Kaur Brar, Dr. Alka Upadhyay, Dr. B.C. Mohanty and Dr. Soumendu Jana for their encouragement and moral supports.

My sincere thanks are due to Mr. Purushotam, Mr. Jant Singh, Mr. Ghanshyam, Mr. Mukesh Kumar, Mr. Indermani, Ms. Era Kinger, Mr. Ram Kumar, Mr. Lalji Verma, Mr. S.P. Verma Mr. Gaurav Nagpal, Ms. Parveen and Ms. Neelam Sadana for their valuable help and technical support. The thesis would not have come to a successful completion, without the help I received from the Sophisticated Analytical Instrument Facility (SAIF) of Panjab University, Chandigarh and IIT Roorkee. I am especially thankful to Sophisticated Analytical Instrument Laboratories (SAI Labs) for helping me in performing tedious experimental characterizations. I am also thankful to DST and DRDO for financial help under sanction order nos. SR/S2/CMP-0035/2011 and ERIP/ER/1103976/M/01/1411, respectively.

I warmly thank Dr. Samita Thakur for her valuable advice, constructive criticism and extensive discussions during the work. I am also grateful to Mr. Satwinder Singh for his consistent support throughout my work. I am also grateful to Dr. Gurbinder Kaur for her help and precious time which she devoted for my cause.

In my daily work I have been blessed with a friendly and cheerful group of fellow friends. My heartfelt thanks are to my friends Ms. Rajni, Ms. Rubina Bansal, Ms. Parveer Kaur, Ms. Purnima Sharma, Ms. Pooja Singla, Ms. Kamaldeep Kaur, Ms. Iman Preet Kaur, Ms. Jagdeep Kaur, Ms. Suninderjeet Kaur, Mr. Mintu Tyagi, Mr. Anoop Pratap Singh, Mrs. Samiksha Verma, Mr. Paramjyot Kumar Jha, Ms. Shivani Sharma, Ms. Navjot Kaur Dhindsa, Dr. Chandni Khurana, Mr. Gaurav Sharma, Mr. Vinoth S. Kumar, Mr. Savidh Khan, Ms. Mandeep Kaur, Dr. Bhupinder Kaur, Dr. Kapil Sood, Mr. S.K. Arya, Dr. Harjinder Singh, Mr. Suresh Kumar, Mr. Gaurav Singla, Ms. Mani Mahajan, Ms. Gitanjali Dhir, Ms. Pallavi Gupta, Ms. Sangeeta, Dr. Kamalpreet Kaur, Dr. Ranvir Panwar, Mr. Praveen Jha, Ms. Rupanjeet Kaur, Ms. Manju Middha and Mr. Devendra Kumar.

On the family front, it gives me immense pleasure to feel the blessings and support of my father- in- law Mr. B.M. Goyal and mother- in - law Ms. Kusum Lata Goyal. My husband Er. Sahil Goyal deserves special thanks who had taken extra burdens on my behalf to take care of numerous familial tasks and allowing me to focus on the current research work. I am also grateful to my mother Ms. Urmila Devi and father Mr. Darshan Kumar Gupta for their tremendous support throughout this beautiful journey of research. I am also thankful to my sister Ms. Himanshi Gupta and brother Mr. Anmol Gupta for providing me unconditional support.

Above all, I owe it all to Almighty God for granting me the wisdom, health and strength to undertake this research task and enabling me to its completion.

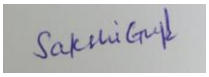

Sakshi Gupta

LIST OF PUBLICATIONS

SCI Journals

1. Structural and optical properties of melt quenched barium doped bismuth vanadate, Sakshi Gupta, K. Singh, Physica B 431 (2013) 89-93.
2. Structural and optical properties of quenched and heat-treated $Bi_4V_{2-x}Mg_xO_{11-\delta}$ ($0.0 \leq x \leq 0.20$), Sakshi Gupta, K. Singh, Ceram. Int. 40 (9) (2014) 14801-14808.
3. Effect of two different dopants (Mg^{2+} and Ca^{2+}) and processing parameters on γ-phase stabilization and conductivity of $Bi_4V_2O_{11-\delta}$, Sakshi Gupta, K. Singh, Ceram. Int. 41 (8) (2015) 9496–9504.
4. Dielectric, optical and structural properties of $Bi_4V_{2-x}Sr_xO_{11-\delta}$ ($0.05 \leq x \leq 0.20$), Sakshi Gupta, K. Singh, J. Phys. Chem. Solids 85 (2015) 18-25.
5. γ- phase stabilized $Bi_4Ba_xV_{2-x}O_{11-\delta}$ ($0.0 \leq x \leq 0.20$): structural, thermal and conducting properties, Sakshi Gupta, K. Singh, Solid State Ionics 278 (2015) 233-238.
6. Effect of dopants ionic radii on dielectric properties of $Bi_4V_{2-x}ME_xO_{11-\delta}$ (where x = 0.0 and 0.15; ME= Mg, Ca, Sr and Ba), Sakshi Gupta, K. Singh, Appl. Phys. A (2015) DOI 10.1007/s00339-015-9498-0.

Non- SCI Journals

1. Structural and optical properties of $Bi_4Mg_{0.05}V_{1.95}O_{11-\delta}$ synthesized via melt quench technique, Sakshi Gupta, K. Singh, AIP Publishing 1591 (1) (2014) 1729-1731.
2. Structural and optical study of γ–BIMEVOX; ME: Ba^{2+} and Sr^{2+}, Sakshi Gupta, K. Singh, AIP Publishing 1661 (2015) 110007 (1-6).

Papers presented in national and international conferences

1. Structural and thermal studies of Sr substituted bismuth vanadate glass ceramics, Sakshi Gupta, K. Singh, 5th National Symposium for Materials Research Scholars, MR-13 IIT Bombay 8th-10th May, 2013
2. Structural and thermal study of magnesium doped melt quenched bismuth vanadate, Sakshi Gupta, K. Singh, NCIMSF, Thapar University, Patiala, Oct 24-26, 2013
3. Structural and optical properties of $Bi_4Mg_{0.05}V_{1.95}O_{11-\delta}$ synthesized via melt quench technique, Sakshi Gupta, K. Singh, 58th DAE Solid State Physics Symposium (DAE-SSPS-2013) Thapar University, Patiala December 17-21, 2013
4. Barium Doped Bismuth Vanadate Structural and Thermal Properties for SOFC, Application, Sakshi Gupta and K. Singh, 4th International Conference on Advances in Energy Research IIT Bombay 10-12 December, 2013
5. Structural and optical study of γ–BIMEVOX; ME: Ba^{2+} and Sr^{2+}, Sakshi Gupta, K. Singh, An International Conference on Condensed Matter Physics (ICCMP-2014) HP University, Shimla November 4-6, 2014.

Index

List of figures

List of tables

ABSTRACT

An electrolyte is a majorly ion conducting material. Solid electrolytes can be employed with reactive electrodes within a wide temperature range with no leakage problems. Due to its high utility it possesses a lot of applications in the field of batteries and fuel cells particularly in solid oxide fuel cells (SOFCs). The main limitation of SOFC is their high operating (800-1000 ℃) temperature which reduces the lifetime of these devices. So, to improve the lifetime of these devices and make them cost effective, the idea is to reduce their operating temperature. Operating temperature in turn depends upon the type of materials employed in them mainly, the electrolyte. Presently, yttria stabilized zirconia (YSZ) is being used as electrolyte in SOFCs but the main limitation of YSZ is sharp decrease in conductivity below 800 ℃. So, it is essential to develop a compatible ion conducting material which can give the better ionic conductivity below 800 ℃.

Doped bismuth vanadate ($Bi_4V_2O_{11-\delta}$) ion conductors are known to represent good conductivity ~ 0.2 Scm^{-1} at 500 °C. Therefore, they can be a promising candidate as electrolytes for intermediate temperature SOFCs (IT-SOFCs). $Bi_4V_2O_{11-\delta}$ based system doped with alkaline earth metals Mg^{2+}, Ca^{2+}, Sr^{2+} and Ba^{2+} has been investigated for structural, thermal, optical and electrical properties in context of solid electrolyte. The present research work is divided into five chapters.

Chapter 1 contains the introductory part related to solid electrolytes and its applications in solid oxide fuel cells. Since, the present work is on electrolytes employed in SOFCs the advantages and disadvantages of different kinds of electrolytes are explained. The study reveals that the development of new electrolyte with high conductivity and thermal stability is required. In the end of chapter, the mechanism of ionic conduction is explained briefly.

Chapter 2 deals with structural correlated properties of $Bi_4V_2O_{11-\delta}$. It explains the detailed literature review of undoped and doped $Bi_4V_2O_{11-\delta}$. From the literature review, it can be concluded that high conducting γ- phase stabilization at room temperature depends on processing parameters, chemical nature of the dopant and their concentration. The role of different dopants, variation in their concentration and effect on conductivity are summarized. Based on literature of undoped and doped bismuth vanadate, reasons of the selection of dopants are given.

Chapter 3 describes the source of raw materials and experimental methods employed for sample preparation. It explains the techniques used for electrical and thermal characterization of as prepared samples. These techniques comprise X-ray diffraction (XRD) for phase identification, Fourier transform infra-red spectroscopy (FTIR) for the analysis of structural variations with dopant, scanning electron microscopy (SEM) for morphological study and energy dispersive spectroscopy (EDS) for semi-quantitative elemental analysis. The thermal expansion coefficient (TEC) of samples was measured to study the lattice expansion behaviour of electrolyte at higher temperatures. Thermogravimetric analysis (TGA) and differential scanning calorimetry (DSC) is used to analyse thermal stability of the synthesized samples. Two probe impedance spectroscopy (IS) was used to investigate the electrical conductivity behaviour of the synthesized samples. UV/vis spectroscopy has been used to estimate the optical band gap of the materials. On some selected quenched samples the Microwave Plasma Atomic Emission Spectroscopy (MP-AES) analysis has also been done to ascertain the composition of samples after melt quench.

Chapter 4 describes the results and discussion of the synthesized samples. The chapter is divided into four sections. In the first section, $Bi_4V_{2-x}ME_xO_{11-\delta}$ ($0.0 \leq x \leq 0.20$; ME = Mg^{2+}) is explained. All the quenched samples show γ- phase stabilization at room temperature. The γ- phase is stabilized at low dopant concentration (Mg^{2+}) than earlier reported concentration

for the similar system. The conversion of γ- phase to ordered β- phase is observed with sintering for $Bi_4V_{2-x}Mg_xO_{11-\delta}$ (x = 0.05, 0.10 and 0.20). The sintered samples exhibit smaller grain size with higher number of grain boundaries, as compared to quenched samples. Higher thermal expansion coefficients (TECs) are observed in sintered than quenched samples. The highest TEC is observed for x = 0.15 sample, i.e. 9.7×10^{-6} /K. Blue shift in FTIR spectra is also observed in sintered samples. The lowest optical band gap is observed in sintered (x = 0.0) sample, i.e. 2.27 eV. The lowest activation energy; E_a is observed for $Bi_4V_{1.85}Mg_{0.15}O_{11-\delta}$ sample ~ 0.74 eV in the temperature range 570-750 °C.

The results of $Bi_4V_{2-x}ME_xO_{11-\delta}$ ($0.0 \leq x \leq 0.20$; ME = Ca^{2+}) samples are discussed in the second section of this chapter. All the quenched samples show γ- phase stabilization irrespective of dopant concentration. Decrease in grain size is observed with the increase in amount of Ca^{2+} dopant. Thus, it can be suggested that Ca^{2+} is acting as grain growth inhibitor in $Bi_4V_2O_{11-\delta}$. The maximum value of TEC is observed for x= 0.15 sample. The conversion of γ- phase to ordered β- phase in sintered $Bi_4V_{2-x}Mg_xO_{11-\delta}$ (x = 0.05, 0.10 and 0.20) and $Bi_4V_{2-x}Ca_xO_{11-\delta}$ (x = 0.05 and 0.10) is observed. Ca^{2+} doped system, particularly at high dopant concentration (x = 0.15 and 0.20) did not show $\gamma \rightarrow \gamma'$ phase transition.

In the third series $Bi_4V_{2-x}ME_xO_{11-\delta}$ ($0.0 \leq x \leq 0.20$; ME = Sr^{2+}) samples were synthesized. X-ray diffraction patterns of all the samples show γ- phase stabilization at room temperature except x = 0.05 sintered sample. The bands in sintered samples are observed to be sharper than quenched samples. The grain size of the samples is found to increase with Sr^{2+} dopant concentration. The increase in value of conductivity is observed with the increase in amount of dopant. The optical band gap of all the samples is observed in semiconducting range. The lowest and the highest optical band gap is 2.39 eV and 2.57 eV for x = 0.10 sintered and x = 0.20 quenched samples, respectively.

Fourth series incorporates the results of $Bi_4V_{2-x}ME_xO_{11-\delta}$ ($0.0 \leq x \leq 0.20$; ME = Ba^{2+}). High conducting disordered γ- phase is stabilized at lower dopant concentration than earlier reported values. The thermal stability of the samples increases with increase in dopant concentration. Activation energies are found in the range 0.70- 1.15 eV. The conductivity increases upto x =0.05 dopant concentration. After that, as dopant concentration increases, the conductivity decreases. A maximum value of conductivity ~ 4.07×10^{-3} Scm^{-1} at 600 °C is observed for the x = 0.05 sintered sample. The optical band gap is observed in the range of 1.5 to 2.0 eV.

$Bi_4V_{1.85}Ba_{0.15}O_{11-\delta}$ sample shows the highest stability and least activation energy amongst all the γ- phase stabilized samples. So, this particular sample has also been sintered at different temperatures to investigate the effect of sintering temperature on different properties particularly conductivity. The conductivity behaviour with respect to different sintering temperature has been discussed in the light of porosity, disordering and density.

The overall conclusions drawn from the whole study are given in chapter 5. Amongst all the sintered samples, the highest conductivity and thermal expansion coefficient is observed for $Bi_4V_{1.90}Mg_{0.10}O_{11-\delta}$ and $Bi_4V_{1.95}Mg_{0.05}O_{11-\delta}$ samples, respectively. After sintering in some samples, the disordered γ- phase converts to ordered β- phase. This chapter also explains the future scope of the present work.

APPENDIX

Symbols used and their abbreviations

Symbol	Abbreviation
σ	Conductivity
TEC	Thermal expansion coefficient
SOFC	Solid oxide fuel cell
IT-SOFC	Intermediate temperature solid oxide fuel cell
XRD	X- ray diffraction
SEM	Scanning electron microscope
FTIR	Fourier transform infra-red spectroscopy
MP-AES	Microwave Plasma Atomic Emission Spectroscopy
TGA	Thermogravimetric analysis
DSC	Differential scanning calorimetry
k	Boltzmann constant
h	Planck's constant
a, b, c	Unit cell lattice parameters
V	Unit cell volume
F	Farad
CPE	Constant phase element
R	Resistance
E_a	Activation energy
E_g	Optical band gap
ΔE	Urbach energy
R_{exp}	Expected R factor
R_{wp}	Weighted profile R-factor
Å	Angstrom
χ	Chi
S	Siemens

Chapter 1
Introduction

1. Introduction to electrolytes

Total conductivity of a material is estimated from the sum of its electronic and ionic contribution as given below:

$$\sigma = \sigma_e + \sigma_h + \sigma_{ion} \quad (1)$$

where, σ, σ_e, σ_h and σ_{ion} represents the total, electronic, hole and ionic conductivity of the system, respectively. Depending on the types of charge carrier in a system, it can be categorised into either electronically or ionically conducting. However, in some systems both kinds of conduction exist and such systems are known as mixed ion conductors [1].

Generally, an electrolyte is a kind of material that can be dominated by conduction of ions instead of electrons. Thus, an electrolyte must possess large values of ionic conduction and negligible values of electronic conduction [2]. Furthermore, the electrolytes can also be categorized as liquid electrolytes and solid electrolytes. Anyhow, researchers are focussing on the solid electrolytes due to their utility in various regimes.

Solid ion conductors came into existence with the development of electric lightning devices. The biggest advantage of solid electrolytes over liquid electrolytes is absence of leakage problem. Additionally, they can be employed along with highly reactive electrodes over a wide range of temperature [3]. Due to their advantages and applications in batteries, fuel cells and other devices electrolytes have become popular. The ionic conductivity of an electrolyte determines the operating temperature as well as efficiency for an electrochemical cell. For an electrochemical cell application electrolytes should be leakage free, efficient with high ionic and low electronic conductivity.

1.1 Basic requirements for ionic conductors

The following properties are required for ionic conductor to be employed as an electrolyte in cell application.

i It should have high ionic conductivity ~ 0.01 Scm $^{-1}$ at 700 °C.

ii It must be an insulator electronically.

iii It must possess high density to limit the ohmic resistance.

iv It must be stable under oxidizing and reducing atmospheres.

v It should be chemically and mechanically compatible with the adjacent components of a cell [4].

1.2 Types of solid electrolytes

Solid electrolytes are the ionic conductors which support the fast ion conduction. The application of these electrolytes depends upon the nature of reactants in an electrochemical cell. Solid electrolytes can be classified based on their structure as follows:

1.2.1 Polymer electrolytes

Polymer electrolytes are solid solutions of alkali metal salts in polymers. In polymer electrolytes the electrical transport occurs mainly due to ions. These electrolytes represent applications in rechargeable batteries due to their shape, versatility and ability of miniaturization [5]. The polymer electrolytes have been developed via three stages namely; dry solid polymer electrolyte, gel polymer electrolyte and composite polymer electrolyte. The dry polymer electrolytes have very low ionic conductivity ~ 10^{-6} Scm^{-1} at room temperature. Thus, research is going on to develop the polymer electrolyte with high conductivity values [6]. Another difficulty with these electrolytes is to maintain their dimensional stability during electrolyte preparation and cell assembly [7].

1.2.2 Glass ceramics electrolytes

Glass ceramics electrolytes offer high ion conductivity as compared to crystalline materials due to their open structure. Their structure corresponds to that of melt glass. Thus, they possess very low activation energies and high conductivities [8]. Usually, the glass ceramics are obtained by melt quench followed by controlled heat treatment. With the help of

mechanical milling, a fine powder of glass is obtained which provides a close contact between electrolyte and electrode [9]. From Li_2S based glasses very high ion conducting superionic phases are obtained by heating these glasses beyond their transition temperature. The phases thus obtained offer very high conductivity values [10].

1.2.3 Crystalline electrolytes

Crystalline electrolytes represent very high ionic conductivity values. The conduction takes place in these kinds of electrolytes through defect formation. The defects (particularly vacancies) are introduced in the crystal lattice via doping of some aliovalent metals. The oxide ion conduction in these systems is carried out by oxide ion jumps via these vacancy sites. There exist numerous crystalline solid electrolytes such as yttria stabilized zirconia, bismuth and ceria based electrolytes etc. [11, 12].

1.3 Applications of solid electrolytes

Due to unique properties, solid electrolytes can be used in various devices particularly electrochemical devices. The interest in this field is rapidly growing due to their excellent chemical and physical stability in wide temperature ranges. The various applications of solid electrolytes are listed below:

1.3.1 Solid electrolyte batteries

Solid electrolyte batteries have long life in comparison to conventional batteries. Solid electrolyte containing batteries can be easily miniaturized which makes them suitable for electronic devices [13, 14].

For rechargeable electric power sources, the lithium solid polymer electrolyte battery, due to its highest predicted energy density has gained a lot of attention. These kinds of batteries possess least environmental and health hazards. Also, the materials employed in them are relatively economical. There is also a great freedom in selection of battery configuration. Li-ion batteries have replaced the conventional batteries like alkaline, Ni-Cd and lead acid

batteries in a wide range of applications. The basic reason behind the popularity of solid electrolyte batteries is attributed to their two times higher output voltage (~3.6 V) compared to aqueous batteries (~1.2-2.0 V). Nowadays, the solid electrolyte batteries are widely used in rechargeable power generation systems [15].

1.3.2 Oxygen sensors

There is an increasing need for chemical sensors that can work in extreme conditions. In other words, the materials with high stability at high temperature and/or in corrosive media to fabricate sensors are required. Oxygen sensors are required for sensor applications to measure oxygen at high temperatures in internal combustion engines, industrial burners and metallurgical processes in controlling emissions. Chemical sensors based on solid electrolytes for detection of pollutant gases have also attracted wide attention of researchers. Potentiometric sensors based on solid ionic conductors can exhibit sensory advantages for gases other than oxygen. These sensors can be characterized by the measurement of their sensitivity, selectivity, and detection range [16, 17]. The main requirements of a solid electrolyte for application in SO_2/SO_3 gas sensing is that it should undergo reversible electrochemical reaction with SO_2/SO_3 and have minimum electronic conductivity [18].

1.3.3 Air separators

The process of air separation is the reverse of oxygen sensors. For example, oxygen free nitrogen or argon gases can be generated by the use of air separators. Solid electrolytes exhibit usually only one type of charge carrier so it can be used for air separators. A device based upon this is used to separate oxygen from air particularly from gases. The dense ceramic membranes can also be used for *in situ* utilization of oxygen for partial oxidation of light hydrocarbons [19].

1.3.4 Solid oxide electrolyser

Solid oxide electrolyser (SOE) is a device which converts the electrical energy into chemical energy. SOE technology can be thought as the reverse of solid oxide fuel cell technology. In SOE the steam is electrolysed into H_2 and O_2 using external electricity. SOEs are expected to provide the higher efficiency for steam electrolysis [20, 21]. SOEs consist of anode, cathode and solid electrolyte. Generally, 8 mol% yttria stabilized zirconia is employed as an electrolyte in them.

1.3.5 Fuel cells

Fuel Cells are the energy conversion devices which can convert the electrochemical energy directly into electricity. No mechanical work is introduced in their operation therefore their efficiency is not limited by Carnot cycle. Fuel cells promise high efficiency, reliability, modularity, fuel adaptability and very low levels of greenhouse gases emission [22]. Based on the electrolytes, the fuel cells can be categorised in various categories namely:

i. Phosphoric acid fuel cell (PAFC).
ii. Alkaline fuel cell (AFC).
iii. Proton exchange membrane fuel cell (PEMFC).
iv. Direct methanol fuel cell (DMFC).
v. Molten carbonate fuel cell (MCFC).
vi. Solid oxide fuel cell (SOFC).

Out of these fuel cells, solid oxide fuel cell has received wide attention due to its high efficiency and use of solid electrolyte. Solid oxide fuel cells can be the best possible candidate to increase the energy supply in an eco-friendly manner. During SOFCs operation only water and heat is generated as a byproduct along with electricity. The efficiency of SOFCs can reach upto 70% with regeneration. Therefore, these can be considered as clean and efficient source of energy. Another advantage of SOFCs is fuel flexibility as any kind of

hydrocarbon can be used as fuel for SOFC operation. The reformation of hydrocarbons to hydrogen gas can take place inside the cell. Thus, SOFCs can be cost effective and viable energy source in near future. However, the main limitation of SOFCs is their high operating temperature which reduces the lifetime of these devices. So, to improve the lifetime of these devices the idea is to reduce the operating temperature. Operating temperature in turn mainly depends on the electrolyte employed in them [23-27].

1.4 Basic characteristics of solid electrolyte for SOFCs

For satisfactory performance, the electrolyte must meet some requirements that limit the choice of the material. Good electrolyte is supposed to have crystal structure with open channels, layers so as to provide pathways for easy ionic transport via hopping mechanism. High conducting electrolytes are required to fulfil the following conditions [28-30]:

i. Availability of large number of free ions so that oxide-ion conductivity is greater than 10^{-2} Scm^{-1} at the operating temperature.
ii. Large number of vacancies for hopping as well as same energies of the occupied and vacant sites.
iii. Three dimensional networking through open channels for the migration of ions.
iv. Thermodynamic stability over a wide range of temperature and oxygen partial pressure.
v. Thermal expansion coefficient (TEC) compatible with that of the electrodes and other cell materials from ambient temperature to cell operating temperature.
vi. Negligible chemical interaction with electrode materials under operation and fabrication conditions to avoid formation of blocking interface phases.
vii. High density to promote gas impermeability.

1.5 Different electrolytes for SOFCs

From the above discussion it is clear that for good performance, an electrolyte should have high ionic conductivity and low electronic conductivity. Moreover, it should be stable in both reducing and oxidizing environments, exhibit good mechanical properties and long term stability with respect to dopant segregation [31]. There are large numbers of electrolytes which have been developed. Depending on their structure or kind of raw materials the solid electrolytes can be grouped into following main categories:

1.5.1 Zirconia based electrolytes

Yttria Stabilised Zirconia (YSZ) has good mechanical and chemical stability over a wide range of temperature. Therefore, consequent efforts are being made to improve the overall properties of YSZ at intermediate temperature ranges. 8 mol% yttria stabilised zirconia (8YSZ) with cubic structure possesses highest ionic conductivity and stability over a wide range of temperature as well as oxygen partial pressure (Figure 1.1) [32]. The conduction mechanism for YSZ is represented in Figure 1.2. 3 mol% yttria stabilised zirconia (3YSZ) has been mixed in different composition with 8YSZ to find whether the conductivity increases by Ghatee *et al.* [33]. Anyhow, 3YSZ in 8YSZ acts as grain inhibitor and caused the reduction in electrical conductivity.

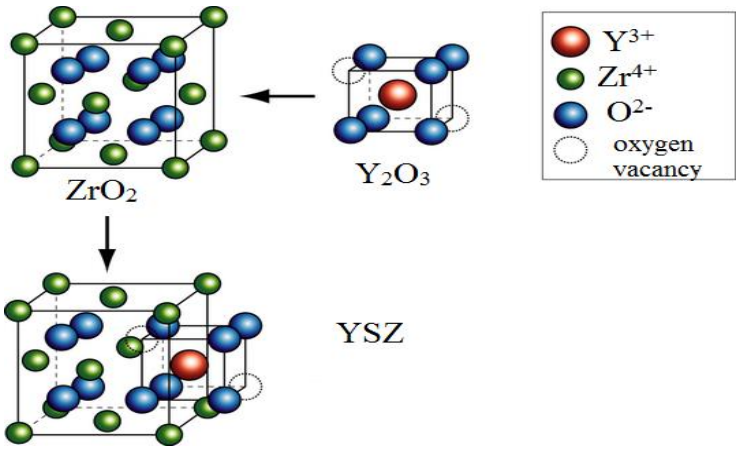

Figure 1.1 Crystal structure of YSZ [43].

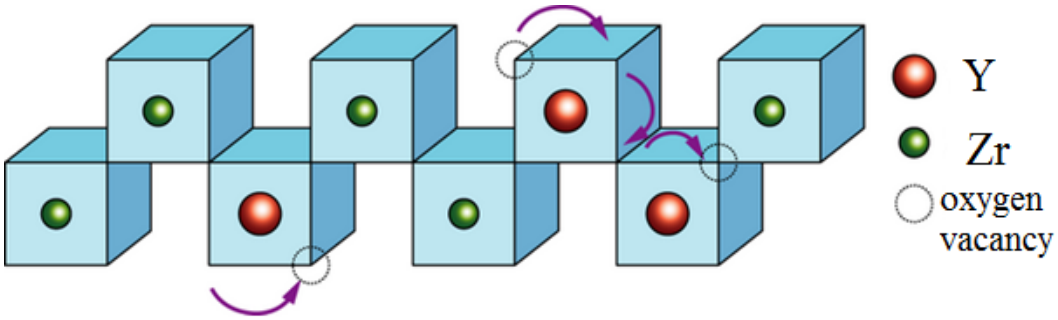

Figure 1.2 Schematic diagram for vacancy transport mechanism in YSZ [43].

On doping ZnO in 8YSZ the sintering temperature can be reduced with better density of the sample. Liu *et al.* [34] have reported that 0.5 wt. % ZnO doped sample exhibited higher conductivity as compared to that of 8YSZ at 800 °C. Shimosono *et al.* [35] reported the decrease in conductivity of YSZ upon incorporation of NiO in it. 1 at. % doping of Si containing 8YSZ and undoped 8YSZ with transitional metal oxides promote the densification as well as grain growth of both Si containing 8YSZ and undoped 8YSZ.

Chao-feng *et al.* [36] prepared the composite electrolyte based on YSZ with 15 wt. % of $La_{9.33}Si_6O_{26}$ (LSO) by modified coprecipitation method. It has been found that increase in conductivity takes place with such type of composition. At 700 °C the value of conductivity is reported ~ 0.125 Scm^{-1}. The observed value of conductivity is one order higher in magnitude than YSZ and two orders higher than $La_{9.33}Si_6O_{26}$. Scandia stabilized zirconia is an alternative to YSZ at intermediate temperature range as it possesses higher conductivity than YSZ [37]. Spirin *et al.* [38] prepared the composition $[xY_2O_3\text{-}(10\text{-}x)\ Sc_2O_3]90ZrO_2$ (x = 2, 3, 4, 5 mol %) and 10-11 mol% Sc_2O_3 - ZrO_2 (ScSz; scandia stabilized zirconia). It has been found that on decreasing the yttria content the conductivity of the samples decreased. The highest conductivity and stability is found for 10ScSZ and 11ScSZ samples.

Rahmawati *et al.* [39] synthesized the composite electrolyte of $CaO\text{-}Y_2O_3\text{-}ZrO_2$ (CYZ) - 8 mol% YSZ via solid state reaction. Doping of Y_2O_3 in ZrO_2 makes the phase transformation from tetragonal to cubic with small percentage of monoclinic phase. While doping of CaO-

Y_2O_3 allows the phase transformation from tetragonal to single cubic phase. This phase transformation enhances the conductivity of the sample. Hence more efforts should be done to stabilize the cubic phase of ZrO_2. Yttria-stabilized zirconia (YSZ) thin films with thickness between the range 6 nm to 100 nm were prepared by radio frequency (RF) sputtering on (0001) Al_2O_3 substrates. It is observed that with the decrease in film thickness from 100 nm to 6 nm the activation energy of the films decreased from 0.99 eV to 0.69 eV. The 100 nm thick film represented similar conductivity values as that of single crystal and behaved like bulk YSZ [40]. Lee *et al.* [41] studied the effect of CuO doping in 8YSZ and found that CuO acts as sintering aid and promotes the densification of YSZ. Also, the slight increase in conductivity is observed upon addition of CuO. Similarly, the cell performance with CuO added YSZ electrolyte is 1.5 times higher than the cell based on the pure YSZ electrolyte. Khare *et al.* [42] synthesized the 6 mol%, 10 mol% and 16 mol% YSZ nanoparticles of different average sizes (10-16 nm) via CO_2 laser based laser vaporization method. The particles have been generated using two different modes continuous and pulsed laser mode. The particle size generated via continuous mode is greater than pulse mode. It is observed that the grain and grain boundary ionic conductivity of samples made from large sized nanoparticles is two orders of magnitude lower as compared to sample made of smaller average size nanoparticles. Below 800 °C, the total conductivity drastically decreases which prevents its application as an electrolyte in IT-SOFCs.

1.5.2 Ceria based electrolytes

Doped ceria can be considered as a promising electrolyte for IT-SOFCs. Ceria (CeO_2) has fluorite structure and number of oxygen vacancies can be increased by substituting Ce^{4+} with trivalent rare earth ions or divalent alkaline earth ions (Figure 1.3). Gd, Y and Sm stabilized ceria electrolytes are the most interesting candidates for IT- SOFCs working between the

temperature ranges 550-650 °C. All of them show good compatibility and high conductivity when incorporated with high performance electrodes [44].

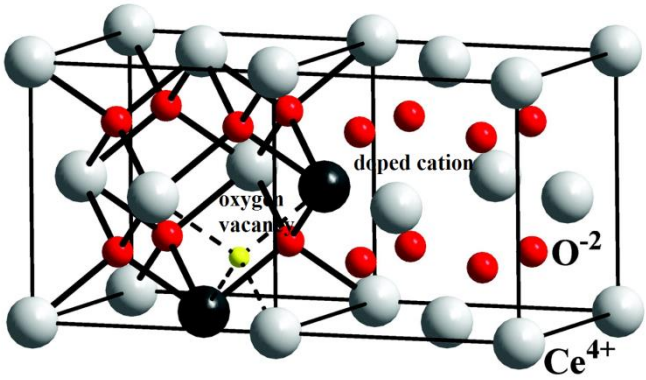

Figure 1.3 Crystal structure of doped ceria [54].

Arabaci *et al.* [45] reported that 10 mol% Gadolinium doped Ceria ($Gd_{0.1}Ce_{0.9}O_{1.95}$, GDC10) represents the conductivity ~ 3.4×10^{-2} Scm^{-1} at 500 °C and very high relative density ~ 98% after sintering at temperature of 1400 °C for 6 hours. The effect of doping of transition metal oxides Fe_2O_3 and CoO in GDC10 has been studied by Fu *et al.* [46]. Co doping decreases the rate of oxygen ion surface transport while that of Fe increases the oxygen ion surface transport. Similarly, doping of Pr in GDC leads to the enhancement of conductivity [47]. It has also been reported that the conductivity, of nano sized SDC (samaria doped ceria) is on the higher side than bulk SDC [48]. Wang *et al.* [49] reported that co-doping of Sm^{3+} and Gd^{3+} in CeO_2 has higher values of conductivity than singly doped CeO_2. Though single phase doped CeO_2 represents good ionic conductivity but the main limitation of this electrolyte is that it represents mixed ionic and electronic conductivity, which leads to the degradation of cell performance and poor mechanical properties. In order to avoid this problem, two-phase nano-composite ceria-based materials are being investigated extensively. It is expected that nano- composite ceria- based electrolyte can exhibit improved ionic conductivity as well as fuel cell performance in comparison to the single-phase doped ceria below 600 °C [50]. The composite electrolytes in this case are synthesized with alkaline earth carbonate salts. When these salts melt, ions generated from them move freely from one electrode to another. The

Li_2CO_3- K_2CO_3- GDC composite represents the conductivity ~ 10^{-3} to 0.2 Scm^{-1} at 400 to 600 °C. It is also expected that the composite electrolytes can represent the conductivity about two orders magnitude higher than single phase SDC electrolytes [51]. Hao *et al.* [52] observed that the composite synthesized through glycine nitrate process $Ce_{0.85}Sm_{0.15}O_{1.9}$ (SDC)-$La_{0.9}Sr_{0.1}Ga_{0.8}Mg_{0.2}O_{2.85}$ (LSGM) exhibits the enhanced conductivity. Y_2O_3- SDC based nano - composite also displays the higher conductivity values than single phase SDC. Most of the ceria based nano- composites exhibit superionic phase transition depending on the composition and operational condition [53]. Though much research has been done on ceria based electrolytes, still work is required for its densification. In addition to this, in reducing conditions the Ce^{4+} reduces to Ce^{3+}, which enhances the electronic conductivity and degrades the fuel efficiency [31].

1.5.3 Apatites

Rare earth apatite materials with general formula; $A_{10-x}M_6O_{26\pm\delta}$, (where A is generally rare earth metal and M= Si, Ge)) have been reported as high oxide ion conducting electrolytes at moderate temperature as well as at low oxygen partial pressures [55, 56]. As the doping of A-site can be done using various methods, research is going on to develop an electrolyte system working at intermediate temperatures efficiently [57]. Doping at A- site with different elements has been reported by various groups. Arikawa *et al.* [58] reported that the conductivity of apatites $La_{10}M_6O_{27}$ (M: Si, Ge) with the doping of Sr at La site despite of lack of crystals symmetry, increases the conductivity. In the similar composition, the doping of Fe increases the ionic conductivity as well as the sinterability [59]. The doping of Pr along with Fe i.e. the composition $La_{9.83-x}Pr_xSi_{4.5}Fe_{1.5}O_{26-\delta}$ has also been studied and observed that incorporation of Pr does not affect the ionic conductivity [60]. On the other hand, the doping of Mg in $La_{10}Si_6O_{27}$ remarkably increases the conductivity and reaches upto 30 × 10^{-3} Scm^{-1} for composition $La_{9.6}Si_{5.7}$ Mg $_{0.3}O_{26.1}$ [61]. As reported by Nijori *et al.* [62] the doping of Ba

at A site also increases the conductivity. Xiang *et al.* [63] studied the effect of In doping at Si site in $La_{10}Si_{6-x}In_xO_{27-\delta}$ (x = 0.1, 0.2, 0.3, 0.4 and 0.5). The maximum conductivity ~ 3.14×10^{-2} Scm^{-1} for x = 0.2 sample is observed. In another report, the comparative study of the effect of Al, Fe and Mg dopants at Si- site has been performed. The conductivity enhancement for all the samples is observed. The maximum conductivity is observed for Mg doped sample among all the synthesized samples [64]. Co-doping of Sr and Al or Fe at A and Si- site, respectively not only decreases the grain and grain boundary resistances but also increases the density and sinterability of the system [65].

Nowadays, in addition to above discussed electrolytes, composite electrolytes also draw a lot of attention. A composite LSO ($La_{10}Si_6O_{27}$) - SDC ($Sm_{0.2}Ce_{0.8}O_{1.9}$) has been synthesized via conventional solid state reaction process. It is found that the conductivity increases in the concentration range between 10- 40 wt% SDC [66]. It has also been seen that there is a large difference between conductivity values of similar composition samples prepared by different synthesis techniques. It has been reported by Jiang *et al.* [67] that the composition $La_{10}Si_6O_{27}$ prepared by water - gel casting route shows much higher conductivity than prepared by solid state route. In the case of development of apatite ceramics better synthesis method than conventional methods are needed to be developed.

1.5.4 $La_2Mo_2O_9$ (LAMOX)

$La_2Mo_2O_9$ (LAMOX) is an oxygen ion conductor which shows oxygen ion conductivity greater than that of YSZ [68]. At temperature higher than 580 °C the structural phase transition in $La_2Mo_2O_9$ (LAMOX) occurs. With the phase transition the nonconductive monoclinic phase 'α' gets converted to conductive cubic phase 'β' with conductivity 6×10^{-2} Scm^{-1} conductivity at 800 °C [69, 70]. A wide range of substitutions for La have been reported to stabilize the high temperature conductive phase. For Nd substitution, the phase α is stable at all studied composition range. For Gd and Y substitution the cubic 'β' form is

stable at room temperature. Marozau *et al.* [71] studied the stability of bismuth and molybdate doped LAMOX and found that the compositions obtained are stable at room temperature. Tungsten doping in $La_2Mo_2O_9$ compositions show sufficiently high ionic conductivity and stability at 600 °C ensuring its applicability as solid electrolytes [72]. The application of tungsten doped $La_2Mo_2O_9$ materials is limited because of high chemical reactivity. Moreover, the high thermal expansion coefficient for this electrolyte makes it less compatible with the electrodes. Therefore, the strong need to develop electrode compatible $La_2Mo_2O_9$ materials still persists. Subramania *et al.* [73] have prepared the samples by doping Pr in LAMOX and reported that α→β transition is suppressed with lowering of sintering temperature. It is found that the conductivity of the samples increases with the increase in Pr content.

It has also been reported that by doping Ca^{2+}, Sr^{2+}, Ba^{2+} and K^{+} in LAMOX series the conductivity decreases with the increase in dopant content. Lopez *et al.* [74] have found that the conductivity is highest for Sr^{2+} doped LAMOX systems. Baijun *et al.* [75] reported that Sr doping in LAMOX increases the electrical conductivity with decreasing ionic conductivity, by keeping the predominant conduction through oxide ions. Even in some Sr doped systems the ion transport number reach upto 0.99. Single-phase ultrafine $La_{1.9}Ba_{0.1}Mo_{1.9}Mn_{0.1}O_9$ (LBMMO) nanopowder has been prepared from the sol-gel auto-combustion method after calcination at 600 °C. The conductivity and activation energy of LBMMO is found to be 6.7×10^{-3} Scm^{-1} and 1.32 eV at 700 °C, respectively [76]. Another co-doped system namely $La_{2-x}K_xMoWO_{9-\delta}$ (x=0, 0.01, 0.03, 0.05, 0.07) has been synthesized via a solid state reaction method. Single β-$La_2Mo_2O_9$ phase is obtained after calcination at 950 °C, and the solid solubility limit of K doping is $x < 0.07$. The sample with $x = 0.03$ represented the maximum value of conductivity among all the synthesized samples [77].

1.5.5 Perovskite related systems

Perovskite ABO_3 kind of structure forms a major category of electrolyte materials. Perovskite structures consist of corner sharing metal oxygen octahedral, BO_6 with a larger cation, A, occupying interstices between these units (Figure 1.4). The ionic conductivities of large number of compounds having perovskite structure have been obtained. The oxygen stoichiometry for these materials is varied by doping either on A site or on B site. Barium based perovskite materials are being studied extensively to serve the purpose of solid electrolytes. $BaCeO_3$ based materials show high conductivity as well as good sinterability, on the other hand, $BaZrO_3$ based materials are chemically stable but are having low density [78-82]. Doping of elements R = Sc, Y, Ho, Dy, Gd has also been done in $BaCeO_3$ [83]. It is found that conductivity in air decreases and followed the sequence Y > Ho > Sc > Dy. The maximum conductivity is found with Y and is equal to 3.6×10^{-4} Scm^{-1}. Sharova *et al.* [84] doped Sc, Y, La in $BaCe_{0.85}R_{0.15}O_{3-\delta}$ and observed that nature of doped elements do not affect the conductivity of materials. Azad *et al.* [85] used solid state route to prepare the rare earth doped compounds with composition $Ba(Ce, Zr)_{1-x}Sc_xO_{3-\delta}$ where x = 0.1 and 0.2. The conductivity is found to be higher for x = 0.2. It has been reported by Hung *et al.* [86] that the conductivity of $BaCeO_3$ increases with the doping of Y at B site whereas the Sr doping at A site along with Y at B site decreases the conductivity.

$BaCe_{0.7}Sn_{0.1}Gd_{0.2}O_{3-\delta}$ (BCSG) and $BaCe_{0.8}Gd_{0.2}O_{3-\delta}$ (BCG) were prepared by solid state technique [87]. It is observed that the conductivity of both the samples is ~ 0.01 Scm^{-1} at 700 °C in humid H_2. The density of BCSG is greater than the density that of BCG. The perovskite $BaCe_{0.9-x}Zr_xY_{0.1}O_{3-\delta}$ where $0.2 < x < 0.8$ has been synthesized by Ricote *et al.* [88] via solid state route followed by sintering at 1700 °C. It is observed that the conductivity of the sample prepared decreases with the increase in cerium content.

$La_{0.88}Sr_{0.12}Ga_{0.82}Mg_{0.18}O_{2.85}$ (LSGM) is another kind of perovskite class of electrolytes. Fukui *et al.* [80] prepared the thin film of LSGM and measured the value of conductivity equal to 0.113 Scm^{-1} at 800 °C. The single cell performance of the cell gives the power density of 0.4 W cm^{-2} at 700 °C. The conductivity of LSGM with transport number ~1 is reported to be stable over extended period.

The system $SrZrO_3$- $SrFeO_3$ system has been synthesized and studied by Unemoto [89]. The composition $SrZr_{0.99}Fe_{0.1}O_{3-\delta}$ has been fabricated via solid state reaction. The activation energies of protonic conduction and deuteron ion conduction are 0.64 eV and 0.66 eV respectively. They reported that protonic conduction in the sample is predominant in the lower temperature region in humidified oxygen as well as in humidified H_2. Transport number of protons is equal to 0.75 in H_2-1.9% H_2O at 900 °C.

The effect of the La:Y ratio on the conductivity of doped $LaYO_3$, has been studied with composition $0.995\ [(1-x)YO_{1.5} + xLaO_{1.5}] + 0.005\ CaO$ (x = 0.1-0.6). The transport numbers reach 1.0 for ions and 0.8 for protons. The conductivity increases in the series as $La_{0.97}Ca_{0.03}YO_{3-\delta} < LaY_{0.97}Ca_{0.03}O_{3-\delta} < La_{0.985}Ca_{0.03}Y_{0.985}O_{3-\delta}$. The maximum conductivity is observed for the stoichiometric composition with the ratio 1:1. Any deviations in the composition lead to a disordering of $LaYO_3$ and decreases conductivity. The conductivity of the sample also decreases with the decrease in PO_2. The ion and proton transport numbers increase with the air humidity. The composition $0.995\ LaYO_3 + 0.005\ CaO$ had the highest part of ionic conduction [91].

It has been reported by Bao *et al.* [92] that protons are the dominant charge carriers in Al - doped $CaZrO_3$ in both oxygen and hydrogen rich atmospheres ranging from 600 to 1100 °C. It is found that electrical conductivity of $CaZr_{0.995}Al_{0.005}O_{3-\delta}$ is higher than that of $CaZr_{0.9}Al_{0.1}O_{3-\delta}$. Zajac *et al.* [93] carried out the comparative study of Gd-doped $BaZrO_3$, $SrZrO_3$, $SrZrO_3$, $BaCeO_3$ and $SrCeO_3$ perovskites. They remarked that the grain boundary

resistance, is the limiting factor of total proton conductivity. The highest proton conductivity is observed for $BaCeO_3$ sample but with lower stability in reducing atmosphere than $BaZrO_3$ and $SrZrO_3$.

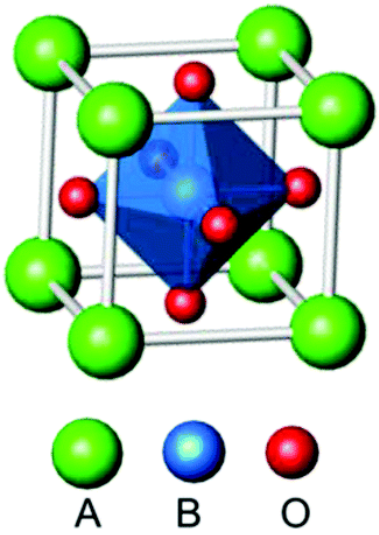

Figure 1.4 ABO_3 perovskite structure [86].

Thus, from the above discussion it can be concluded that many ceramic electrolytes have been studied by various groups. There are many factors like phase stabilization, density, chemical stability in both reducing and oxidising atmospheres etc. which should be taken care while selecting a material to be employed as an electrolyte in SOFCs.

1.5.6 Bismuth based electrolytes

Bi_2O_3 consists of three different phases with respect to temperature and only one phase called δ-Bi_2O_3 has the highest conductivity i.e. >1 Scm^{-1} at 800 °C. The δ-Bi_2O_3 has the fluorite type structure with random distribution of ions. Takahashi *et al.* [94, 95] has reported that δ-Bi_2O_3 can be stabilised by partial substitution at Bi site. It has also been reported that electrodes with stabilized bismuth oxide electrolytes exhibit lower interfacial resistance than zirconia electrolytes. Berezovsky *et al.* [96] reported that the composite electrolyte with composition $(Bi_2O_3)_{0.75}(Y_2O_3)_{0.20}(Nb_2O_5)_{0.05}$ represents higher values of conductivity than stabilized zirconia electrolytes. Dysprosium tungsten stabilized bismuth oxide (DWSB),

dysprosium gadolinium stabilized bismuth oxide (DGSB), and dysprosium cerium stabilized bismuth oxide (DCSB) have been synthesized via solid state and wet chemical method. DGSB shows the maximum conductivity ~ 0.94 Scm^{-1} at 650 °C [97]. The effect of TiO_2 doping on Bi_2O_3 has also been reported [98]. The samples have been prepared with the composition (1-x) Bi_2O_3- x TiO_2 where x = 0.05, 0.10, 0.15, 0.20. The highest conductivity is obtained for x = 0.15 i.e. 9×10^{-7} Scm^{-1}. Since, Bi_2O_3 based compounds are not stable in reducing conditions, Er stabilized Bi_2O_3 (ESB) has been combined with Nd doped CeO_2 and 38 wt% $(Li\text{-}0.5Na)_2CO_3$ by Baek *et al.* [99]. It is observed that only 2% addition of ESB increases the conductivity and stability of the system. Another composite, $(Bi_2O_3)_{1-x-y}(Tm_2O_3)_y$ (where x = 20 and y = 5, 10, 15, 20 mol%) has been reported by Durmus *et al.* [100]. The maximum value of conductivity is observed for x = 20 and y = 5 mol% at 1000 °C.

Taninouchi *et al.* [101] studied the behaviour of bismuth vanadate (BIMEVOX) by doping different transition metals. The composition $Bi_2(V_{0.95}TM_{0.05})O_{5.5+\delta}$ where (TM: transition metal) has been studied. It is found that incorporation of transition metals slightly increase the conductivity and thermal stability of material.

Bismuth vanadate has also been studied extensively by different researchers. $Bi_{4+y}V_{2-x-y}M_xO_{11-y-x}$ where M = Nd, Gd, Er and Yb has been prepared [102]. The highest conductivity is obtained for y = 0.0 and x = 0.2 with conductivity values upto 2×10^{-4} Scm^{-1} at 300 °C. The conductivity behavior of BIMEVOX on doping Ti^{3+} at V^{5+} has been studied by Kant *et al.* [103]. It is observed that the conductivity of the prepared samples increases and the activation energy decreases with increase in Ti content. The main problem with these kinds of electrolytes is that they lack of stability under reducing conditions. The use of bilayer structure with a more stable electrolyte layer on the anode side has been suggested to solve

the above problem [104]. The conductivity of these compounds depends on the chemical nature of the dopants, their concentration and processing parameters.

Therefore, from the above discussion, it can be concluded that the substantial research is required to obtain an electrolyte fulfilling all the requirements for their applicability in SOFCs.

1.6 Ionic conduction mechanism

For ionic conductivity in a solid, transport of one or more types of ions across the lattice takes place. In an ideal crystal, all the ions are arranged in regular manner or closed packed form. Thus, they are not free to move within the lattice only a little space for diffusion or vibration around is available. With the increase in temperature the free energy of the system tends to minimize through an increase in entropy. The entropy of the system is the measure of degree of disorderdness in the system. The conductivity of the system increases with the introduction of two types of defects namely; Schottky and Frenkel. Collectively, these are called point defects. In Schottky crystal, imperfection arises in a way that a pair of ions, one cation and anion, disappears leaving their positions vacant. On the other hand, in Frenkel defect a single ion is missing from its lattice position. Thus, both Frenkel and Schottky defects result into vacant sites in the crystal. Any ion in the immediate vicinity can jump to one of the vacant sites. This leaves the previous site of the ion vacant which could now host another ion. This process can lead to transport of ions across the solid giving rise to conductivity and this mechanism is termed as vacancy migration. The ion that moves to the interstitial site, gives rise to the Frenkel defect. In Frenkel defect, an ion can subsequently jump to a neighbouring interstitial site and so on, resulting in long distance motion of the ion. This kind of migration of ions is known as interstitial migration. Apart from these two mechanisms, there is another mechanism called interstitialcy mechanism which refers to the conduction mechanism through cooperative movement of two or more ions. The disorder in crystalline solids is

significantly less than that in liquids. The defects in the solids in order to increase the ionic conductivity can be increased in a number of ways out of which doping of parent system with different atoms is the most popular one.

References

1. E. Ivers-Tiffe'e, Solid: Oxygen Ions, Elsevier B.V. (2009) 81.
2. J. Tolchard, Solid: Protons, Elsevier B.V. (2009) 88.
3. S. Chandra, Superionic solids: Principles and Applications, Elsevier Science Ltd. North Holland, Amsterdam, 1981.
4. N. Preux, A. Rolle, R.N. Vannier, Functional Materials for Sustainable Energy Applications**,** France Woodhead Publishing Limited (2012) 370.
5. A.K. Nath, A. Kumar Electrochim. Acta 129 (2014) 177.
6. A. M. Stephan, K.S. Nahm, Polymer 47 (2006) 5952.
7. Eun-Hye Kil, Keun-Ho Choi, Hyo-Jeong Ha, S. Xu, J.A. Rogers, M.R. Kim, Young-Gi Lee, Kwang Man Kim, Kuk Young Cho, Sang-Young Lee Adv. Mater. 25 (2013) 1395.
8. T. Minami, A. Hayashi, M. Tatsumisago, Solid State Ionics 177 (2006) 2715.
9. A. Hayashi, T. Ohtomo, F. Mizuno, K. Tadanaga, M. Tatsumisago, Electrochem. Commun. 5 (2003) 701.
10. M. Tatsumisago, F. Mizuno, A. Hayashi, J. Power Sources 159 (2006) 193.
11. J. Maier, Solid State Ionics 75 (1995) 139.
12. E. Kendrick, J. Kendrick, A. Orera, P. Panchmatia, M.S. Islam, P.R. Slater, Fuel Cells 11, (1) (2011) 38.
13. http://www.google.com/patents/US3057945.
14. J. W. Fergus, J. Power Sources 195 (2010) 4554.
15. P. Verma, P. Maire, P. Novák, Electrochim. Acta 55 (2010) 6332.
16. E. B. Makovos, Cbung-Cbhm Liu, Sensors Actuat. B 3 (1991) 15.
17. W. Weppner, Sensors Actuat. 12 (1987) 107.
18. P. Gopalan, S. Saha, S. Bobade, A. Kulkarni J. Solid State Chem. 155 (2000) 154.

19. H. Bouwmeester, A.J. Burggraaf, The CRC Handbook of Solid State Electrochemistry, CRC Press, Boca Raton, FL (1997) 481.
20. Q. Cai, C.S. Adjiman, N.P. Brandon, J. Power Sources 268 (2014) 212.
21. S. Xu, S. Chen, M. Li, K. Xie, Y. Wang, Y. Wu, J. Power Sources 239 (2013) 332.
22. B. Ku, Y. Zhang, J. Univ. Sci. Technol. B. 15(1) (2008) 84.
23. M.S. Dresselhaus, I. L. Thomas, Nature 332 (2001) 332.
24. B.C.H. Steele, H. Angelika, Nature 345 (2001) 414.
25. R.B. Cervera, Y. Oyama, S. Yamaguchi, Solid State Ionics 178 (2007) 569.
26. S.M. Gheno, V.L. Pimentel, M.R. Morelli, P.I.F. Paulin, Microscopy and Microanalysis 19 (2013) 688.
27. A.B. Stambouli, E. Traversa, Renew. Sust. Energ. Rev. 6 (2002) 433.
28. S.C. Singhal, K. Kendall, High temperature solid oxide fuel cells: fundamentals, design, and applications, Elsevier Science Ltd. Oxford, UK (2003).
29. J. Fergus, R. Hui, X. Li, D. P. Wilkinson, J. J. Zhang, Solid oxide fuel cells: materials properties and performance, CRC Press, London, NY (2009).
30. EG&G Technical services, Fuel Cell Handbook (5th), Parsons, Inc., Morgantown, West Virginia, EUA (2000).
31. A.J. Jacobson Chem. Mater. 22 (2010) 660.
32. S.P.S. Badwal, Solid State Ionics 52 (1992) 23.
33. M. Ghatee, M.H. Shariat, J.T.S. Irvine, Solid State Ionics 180 (2009) 57.
34. Y. Liu, L.E. Lao, Solid State Ionics 177 (2006) 159.
35. T. Shimosono, H. Kishimoto, K.Yamaji, M.E. Brito, T. Horita, H. Yokokawa, Solid State Ionics 225 (2012) 61.
36. T.S. Zhang, Z.H. Du, S. Li, L.B. Kong, X.C. Song, J. Lu, J. Ma, Solid State Ionics 180 (2009) 1311.

37. L. Chao-feng, Z. Hong, Z. Zhe, X. Jun-xiao, L. Zhi-cheng, J. Cent. South Univ. 19 (2012) 22.
38. A. Spirin, V. Ivanov, A. Nikonov, A. Lipilin, S. Paramin, V. Khrustov, A. Spirina, Solid State Ionics 225 (2012) 448.
39. F. Rahmawati, B. Prijamboedi, S. Soepriyanto, Ismunandar, Int. J. Min. Meta. Mat. 19 (9) 2012 863.
40. J. Jiang, X. Hu, W. Shen, C. Ni, J. L. Hertz, Appl. Phys. Lett. 102 (2013)143901.
41. J.G. Lee, O.S. Jeon, K.H. Ryu, M.G. Park, S. H. Min, S.H. Hyun, Y.G. Shul, Ceram. Int. 41 (6) (2015) 7982.
42. J. Khare, M.P. Joshi, S. Satapathy, H. Srivastava, L.M. Kukreja, Ceram. Int. 40 (2014) 14677.
43. http://www.doitpoms.ac.uk/tlplib/fuel-cells/sofc_electrolyte.php.
44. B.C.H Steele, Solid State Ionics 129 (2000) 95.
45. A. Arabaci, M.F. Oksuzomer, Ceram. Int. 38 (2012) 6509.
46. C. Fu, X. Ge, S.H. Chan, Q. Liu, Int. J. Hydrogen Energ. 38 (2013) 16524.
47. S. Ramesh, K.C. James Raju, Int. J. Hydrogen Energ. 37 (2012) 10311.
48. J. Ju, F. Chen, C. Xia, Electrochim. Acta 136 (2014) 422.
49. Feng-Yun Wang, S. Chen, S. Cheng, Electrochem. Commun. 6 (2004) 743.
50. M.A. Khan, R. Raza, R.B. Lima, M. Asharf Chaudhry, E. Ahmed, G. Abbas, Int. J. Hydrogen Energ. 38 (2013) 16524.
51. M. Benamira, A. Ringuedé, V. Albin, R. N. Vannier, L. Hildebrandt, C. Lagergren, M. Cassir, J. Power Sources 196 (2011) 5546.
52. G. Hao, X. Liu, H. Wang, H. Be, L. Pei, W. Su, Solid State Ionics 255 (2012) 81.
53. L. Fan, C. Wang, M. Chen, B. Zhu, J. Power Sources 234 (2013) 154.
54. K. Schwarz, PNAS 103 (10) (2006) 3497.

55. P.R. Slater, J.E.H. Sanson, J.R. Tolchard, Cem. Rec. 4 (2004) 373.

56. E. Kendrick, M.S. Islam, P.R. Slater, J. Mater. Chem. 17 (2007) 3104.

57. A.L. Shaula, V.V. Kharton, F.M.B. Marques, J. Solid State Chem. 178 (2005) 2050.

58. H. Arikawa, H. Nishiguchi, T. Ishihara, Y. Takita, Solid State Ionics 136-137 (2000) 31.

59. J. McFarlane, S. Barth, M. Swaffer, J.E.H. Sansom, P.R. Slater, Ionics (2002) 149.

60. A.A. Yaremchenko, A.L. Shaula, V.V. Kharton, J.C. Waerenborgh, D.P. Rojas, M.V. Patrakeev, F.M.B. Marques, Solid State Ionics 171 (2004) 51.

61. H. Yoshioka, S. Tanase, Solid State Ionics 176 (2005) 2395.

62. Y. Nojiri, S. Tanase, M. Iwasa, H. Yoshioka, Y. Matsumura, T. Sakai, J. Power Sources 195 (2010) 4059.

63. J. Xiang, Zhan-Guo Liu, Jia-Hu Ouyang, Fu-Yao Yan, J. Power Sources 251 (2014) 305.

64. C. Argirusis, E. Jothinathan, G. Sourkouni, O. Van der Biest, F. Jomard, Solid State Ionics 257 (2014) 53.

65. X.G. Cao, S.P. Jiang, Int. J. Hydrogen Energ. 39 (2014) 19093.

66. S. Qingle, Z. Hua, L. Tianjing, Y. Fangli, H. Haijun, J. Rare Earths 33(3) (2015) 304.

67. S.P. Jiang, L. Zhang, H.Q. He, R.K. Yap, Y. Xiang, J. Power Sources 189 (2009) 972.

68. P. Lacorre, F. Goutenoire, O. Bohnke, R. Retoux, Y. Laligant, Nature 404 (2000) 856.

69. S. Georges, F. Goutenoire, F. Altorfer, D. Sheptyakov, F. Fauth, E. Saurd, P. Lacorre J. Mater. Chem. 161 (2003) 231.

70. S. Georges, F. Goutenoire, Y. Laligant, J. Mater. Chem. 13 (2003) 2317.

71. I.P. Marozau, D.M. Lopez, A.L. Shaula, V.V. Kharton, E.V. Tsipis, P. Nunez, J.R. Frade, Electrochim. Acta 49 (2004) 3517.

72. D.M. Lopez, J.P. Martinez, J.C.R. Morales, D.P. Coll, M.C.M. Sedeno, P. Nunez, Solid State Ionics 178 (2007) 1366.
73. A. Subramania, T. Saradha, S. Muzhumathi, J. Power Sources 167 (2007) 319.
74. D.M. Lopez, D.P. Coll, J.C.R. Morales, J.C. Vazquez, M.C.M. Sedeno, P. Nunez Electrochim. Acta 52 (2007) 5219.
75. Y. Baijun, L. Ming, Z. Jiayun, J. Rare Earths 31(4) (2013) 428.
76. T. Changan, Y. Qiyi, X. Jinsong, Y. Jie, S. Hong, J. Bifa, B. Weitao, J. Rare Earths 32 (5) (2014) 423.
77. H. Liu, J. Zhang, Z. Wen, J. Han, Solid State Ionics 276 (2015) 90.
78. Y. Liu, Y. Guo, R. Ran, Z. Shao, J. Membrane Science 209 (2012) 423.
79. L. Bi, E. Fabbri, Z. Sun, E. Traversa, Solid State Ionics 196 (2011) 59.
80. T. Fukui, S. Ohara, K. Murata, H. Yoshida, K. Miura, T. Inagaki, J. Power Sources 106 (2002) 142.
81. E. Fabbri, A. D'Epifanio, E. Di Bartolomeo, S. Licoccia, E. Traversa, Solid State Ionics 179 (2008) 558.
82. L. Chao-Feng, Z. Hong, Z. Zhe, X. Jun-Xiao, L. Zhi-Cheng, J. Cent. South Univ. 19 (2010) 22.
83. V.P. Gorelov, V.B. Balakireva, Y.N. Kleshchev, V.P. Brusentsov, Inorg. Mater. 37 (5) (2001) 535.
84. N.V. Sharova, V.P. Gorelov, Russ. J. Electrochem. 39 (5) (2003) 461.
85. A.K. Azad, J.T.S. Irvine, Solid State Ionics 178 (2007) 635.
86. I. Hung, H. Peng, S. Zheng, C. Lin, J. Wu, J. Power Sources 193 (2009) 155.
87. R. Yan, Q. Wang, K. Xie, Ionics 15 (2009) 501.
88. S. Ricote, N. Bonanos, M.C. Marco de Lucas, G. Caboche, J. Power Sources 193 (2009) 189.

89. A. Unemoto, A. Kaimai, K. Sato, K. Sato, N. Kitamura, K. Yashiro, H. Matsumoto, J. Mizusaki, K. Amezawa, T. Kawada, Solid State Ionics 181 (2010) 868.

90. F. A. Rabuffetti, R. L. Brutchey, Dalton Trans. 43 (2014) 14499.

91. V.B. Balakireva, A.Y. Stroeva, V.P. Gorelov, Russian J. Electrochem. 41, 5 (2005) 535.

92. J. Bao, H. Ohno, N. Kurita, Y. Okuyama, N. Fukatsu Electrochim. Acta 56 (2011) 1062.

93. W. Zając, D. Rusinek, K. Zheng, J. Molenda, Cent. Eur. J. Chem. 11(4) (2013) 471.

94. T. Takahashi, H. Iwahara, Y. Nagai, J. Appl. Electrochem. 2 (1972) 97.

95. T. Takahashi, H. Iwahara, T. Arao, J. Appl. Electrochem. 5 (1975) 187.

96. J. Berezovsky, H.K. Liu, S.X. Dou, Solid State Ionics 66 (1993) 201.

97. A. L. Ruth, K.T. Lee, M. C. Clites , E. D. Wachsman, ECS Trans. 64 (2) (2014) 135.

98. G. Singla, P.K. Jha, J.K. Gill, K. Singh, Ceramics Int. 38 (3) (2012) 2065.

99. Seung-Seok Baek, N. Lee, Byung-Kook Kim, H. Chang, Sun-Ju Song, Jun-Young Park, Int. J. Hydrogen Energ. 37 (2012) 16823.

100. S. Durmus, V. Corumlu, T. Cifci, I. Ermis, M. Arı, Ceram. Int. 39 (2013) 5241.

101. Y. Taninouchi, T. Uda, T. Ichitsubo, Y. Awakura, E. Matsubara, Solid State Ionics 181 (2010) 1279.

102. C.K. Lee, C.S. Ong, Solid State Ionics 117 (1999) 301.

103. R. Kant, K. Singh, O.P. Pandey, Mat. Sci. Eng. B 158 (2009) 63.

104. J.Y. Park, H. Yoon, E.D. Wachsman, J. Am. Ceram. Soc. 88 (2005) 2402.

Chapter 2

Literature review

Present work is focussed on the bismuth vanadate based systems and their structural, thermal and electrical properties for possible use as an electrolyte in SOFCs. So, in this chapter literature review regarding bismuth vanadate system has been presented.

2.1 Structural aspects and properties

The parent material $Bi_4V_2O_{11-\delta}$ (BIVOX) is a member of Aurivillus family of compounds, it consists of alternate layers of $(Bi_2O_2)^{2+}$ and oxygen deficient perovskite $(VO_{3}\square_{0.5})^{2-}$ layers as shown in Figure 2.1. Depending on temperature, $Bi_4V_2O_{11-\delta}$ exhibits three reversible structural polymorphs i.e. α, β and γ. All these polymorphs can be explained on the basis of mean orthorhombic unit cell of dimensions $a_m \approx 5.53$, $b_m \approx 5.61$, $c_m \approx 15.28$ Å. Superstructure α (monoclinic) $a_m \approx 3\ a_m$, $b_m \approx b_m$, and $c_m \approx c_m$; β (orthorhombic) $a_m \approx 2\ a_m$, $b_m \approx b_m$, and $c_m \approx c_m$ and γ (tetragonal) $a_m \approx a_m/\sqrt{2}$, $b_m \approx b_m$, and $c_m \approx c_m$ [1, 2]. The phase transitions α → β and β → γ take place around 447 and 567 °C, respectively. Out of these phases, the γ- phase is most disordered and hence it represents the highest total conductivity in comparison to the other two phases. Substitution of vanadium ions by aliovalent cations can lead to the stabilization of the highly conducting γ- phase at room temperature [3]. The X-ray diffraction pattern of all the three phases is similar except for the split and superlattice diffraction peaks. The appearance of weak reflection at ~ 24.4˚ is an indication of the superstructure of α- phase. Similarly, the absence of splitting in XRD peak at ~ 32˚ indicates the stabilization of γ- phase. The doped cation modifies the symmetry and connectivity of polyhedral inside the perovskite layer thus, the ionic conductivity depends strongly on the nature of doped cation [4, 5]. Various compounds with family named as BIMEVOX have been developed with the substitution of Bi^{3+} and/ or V^{5+} by divalent, trivalent and pentavalent cations on both the sites in order to stabilize the γ- phase at room temperature.

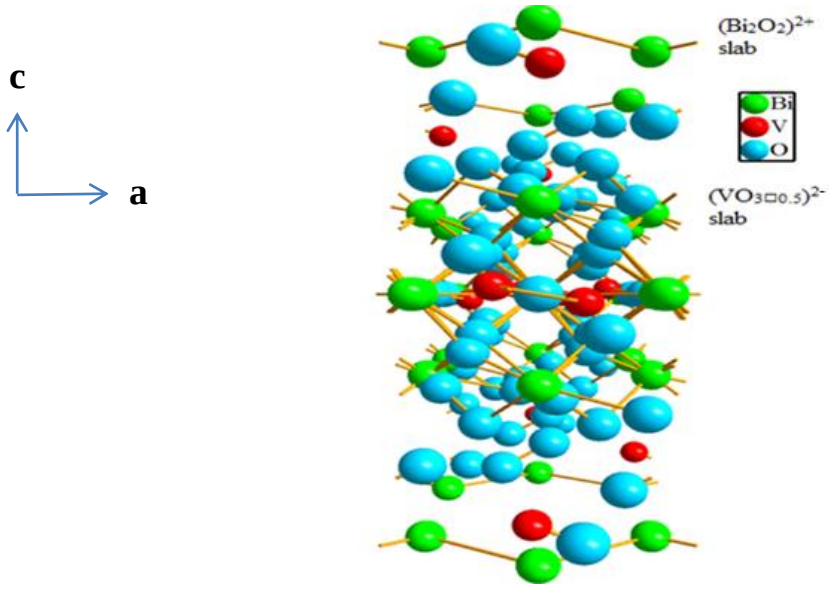

Figure 2.1 Unit cell of $Bi_4V_2O_{11-\delta}$ created with the help of cell parameters obtained from Rietveld refinement of XRD data (Diamond Software).

Kim *et al.* [6] synthesized the single and polycrystalline $Bi_4V_{2-x}Co_xO_{11-\delta}$ (x = 0.0–0.2). It is observed that high temperature γ- phase gets stabilized at room temperature for x = 0.2. It is also found that there exists large electrical anisotropy between the directions parallel and perpendicular to $(Bi_2O_2)^{2+}$ layers, the conductivity of the samples in the direction parallel to $(Bi_2O_2)^{2+}$ layers is three times higher than that of perpendicular direction demonstrating that the conductivity in $Bi_4V_2O_{11-\delta}$ is two dimensional. Kezionis *et al.* [7] studied the relaxation mechanism in $Bi_2V_{0.9}Co_{0.1}O_{5.35}$ sample and attributed the relaxation mechanism to diffusional polarization which in turn can be related to the short range jumping of oxygen vacancies in the crystal lattice. According to other report, small grain size in $Bi_2V_{0.9}Co_{0.1}O_{5.35}$ stabilizes the γ- phase at room temperature [8]. Similarly, $Bi_2V_{1-x}Ni_xO_{5.5-\delta}$ system γ- phase stabilization is found to take place above x = 0.10 with no discontinuity between the high and low temperature regions in the range 0.10 < x < 0.20. The conductivity value at 300 °C for x = 0.12 is ~ 1.71×10^{-3} Scm^{-1} [9]. Krok *et al.* [10] analysed the γ- $Bi_2V_{0.9}Ni_{0.10}O_{5.5-\delta}$ sample, with the help of X- ray and neutron powder diffraction patterns and observed that oxide ion vacancies are exclusive to equatorial position around Ni/V atoms. Percentage of V/Ni

distorted tetrahedra is 68%. The remaining portion is due to distorted octahedra. It has also been reported that doping of La and Ni in $Bi_{2-x}La_xV_{1-y-z}Cu_yNi_zO_{5.5-\delta}$ (x=0.10–0.20; y=0.0–0.10; z=0.0–0.20) reduces the ionic conductivity, which can be related to the decrease in thermal expansion coefficient with increase in doping. As according to phenomenological theory of ion transport, the mobility of point defects decreases with decrease in TEC [11]. Another family of compounds BIMEVOF (where ME = ZnF_2; BIZNVOF) has been generated by Jacobsoone *et al.* [12] with the substitution of oxygen by flourine in order to obtain a mixed anion phase. This study revealed that doping of fluoride like ZnF_2 does not bring too much fluorine in perovskite layers. While, doping of fluorides, with similar valence like Nb or Sb as that of V brings higher amount of fluorine in perovskite layers. ZnF_2 doping though decreases the number of vacancies in the system but increases the stability. In $Bi_2V_{1-x}Zn_xO_{5.5-x/2}$ ($0.05 \leq x \leq 0.27$), system, the x= 0.10 composition is found to have the highest low temperature conductivity i.e. ~ 4.09×10^{-3} Scm $^{-1}$ at 300 °C [13]. Doping of rare earth elements like Nd, Gd, Er and Yb in $Bi_4V_2O_{11-\delta}$ gives rise to a new composition $Bi_{4+y}V_{2-x-y}M_xO_{11-y-x}$. It is observed that irrespective of dopant the maximum value of conductivity ~ 2×10^{-4} Scm $^{-1}$ at 300 °C is observed for composition with y = 0.0 and x = 0.2 [14]. The substitution of Ge at V site in $Bi_2V_{1-x}Ge_xO_{5.5-x/2}$ (where x = 0.2, 0.4 and 0.6) showed the fine tuning between orthorhombic → tetragonal → orthorhombic phase transitions with the increase in amount of doping. The γ- phase stabilization occurs only at x = 0.4 [15]. $Bi_4V_{2-x}Cu_xO_{11-x}$ ($0.07 \leq x \leq 0.20$) composition has been synthesized via melting process. High electrical conductivity is observed in the temperature range 100 – 400 °C. x = 0.15 has been reported as the optimized composition. Above this value of 'x' the interaction between the defects increases and decreases the conductivity [16]. Paydar *et al.* [17] synthesized the composite of $Bi_2V_{0.9}CO_{0.1}O_{5.35}$ with 3 mol% Y_2O_3 stabilized ZrO_2 (3YSZ). It has been reported that with the addition of 0.5 to 1 wt. % of 3YSZ, the grain size reduces to lower than

1 μm and increases the microhardness and toughness by more than 15%. However, at low temperature the total conductivity decreases as 3YSZ content increases. In addition to this, the decrements at higher temperatures are less significant. The relationship between the conductivity and structure of CuF_2 substituted BIMEVOX; $Bi_2V_{1-x}Cu_xO_{5.5-5x/2}F_{2x}$ (BICUVOF) (where $0.10 \leq x \leq 0.20$) has also been developed. It is found that in BICUVOF samples the conductivity drops and can be related to the fact that fluorine does not enter into the defect layers as that of BIZNVOF. Also, the mixed anion effect analogous to mixed ion effect seen in cation conducting system as observed for BICUVOF system [18]. The comparison study of $Bi_4Me_{0.2}V_{1.8}O_{11-x}$ (Me = Cu, Co) composition has been carried out by Guillodo *et al.* [19]. Total electrical conductivity with respect to temperature, oxygen partial pressure, thermal history and nature of dopant has been reported. It is observed that Cu doped sample behaves as a pure oxide ionic conductor whereas Co doped system exhibits p- type conductivity. Also, the electrical conductivity of Cu doped sample is found to be 2 to 3 times higher than Co doped sample. Guillodo *et al.* [20] studied the same composition to determine their oxygen exchange coefficients and bulk oxygen tracer diffusion coefficients. It has been found that, though, the conductivity of $Bi_4Me_{0.2}V_{1.8}O_{11-x}$ (Me = Cu, Co) system is higher than conventional electrolytes such as YSZ or GDC, but their oxygen surface exchange coefficients are low. According to another report, on reducing the partial pressure to 10 k Pa the n- type electronic conductivity in $Bi_4Cu_{0.2}V_{1.8}O_{11-x}$ increases and then finally the γ- phase decomposes. On the other hand, annealing at 12 M Pa of oxygen partial pressure neither the decomposition in γ- phase nor the electron – hole conduction is observed. However, further increase in pressure leads to partial ordering in the oxygen vacancies and thus lowering in the value of conductivity [21]. In another study, the effect of higher doping of Mg in $Bi_2Mg_xV_{1-x}O_{5-3x/2}$ ($0.05 \leq x \leq 0.40$) has been studied. The solid solution limit, indicated by the emergence of secondary phase at x = 0.40. In this system the γ- phase stabilization occurs in

the range $0.13 \leq x \leq 0.25$. Below and above this range the orthorhombic phase (β- phase) is observed [22]. Dygas *et al.* [23] reported the impedance analysis of $Bi_2V_{1-x}Mg_xO_{5.5-1.5x-\delta}$ (x = 0.13) composition in the frequency range from 10 MHz to 0.01 Hz at temperatures between 20 and 680 °C. The difference between values of activation energy for conductivity of grains and grain boundaries indicates the grain boundary polarization and the charge carrier relaxation within the grains. It has also been found that ion transport properties of the intergranular regions are different than those of grains. Zr doped BIMEVOX system with composition $Bi_2Zr_xV_{1-x}O_{5.5-x/2}$ ($0.05 \leq x \leq 0.50$) revealed α- phase formation below x = 0.10. The stabilization of β- phase is observed in between x = 0.10 and 0.16. On increasing the amount of Zr upto x = 0.19, γ- phase is stabilized whereas for $x \geq 0.22$ a secondary phase $Bi_8V_2O_{17}$ appears along with γ- phase. The study of Zr doped BIMEVOX system revealed that solid solution limit depends on the valence of dopants and it prefers coordination number in oxide environment [24]. The analysis of Zr doped BIMEVOX system with neutron diffraction method revealed that the increase in Zr content increases the low temperature stability upto x = 0.10 and completely replace α- phase at room temperature. During this study, the γ- phase is stabilized for x = 0.20 at room temperature [25].

In the case of $Bi_4V_{2-x}P_xO_{11}$ ($0.05 \leq x \leq 0.50$) series, α- phase is stabilized for $0.05 \leq x \leq 0.20$. With the increase in value of 'x' the secondary phase indexed as $BiPO_4$ appears along with α- phase. Thus, the doping of P does not lead to stabilization of γ- phase alike other pentavalent ions. The conductivity values are also found to be less dependent on value of 'x' [26]. Paydar *et al.* [27] synthesized the Ti and Ti- Cu double substituted $Bi_4V_2O_{11}$ compound with composition $Bi_2V_{1-x}Ti_xO_{(11-x)/2}$; (BITIVOX) ($0.085 \leq x \leq 0.15$) and $Bi_2V_{0.9}Cu_{(0.1-x)}Ti_xO_{5.35+x}$; (BICUTIVOX) ($0 \leq x \leq 0.1$). For the composition BITIVOX γ- phase stabilization occurs for $x > 0.125$ whereas for BICUTIVOX sample the γ- phase is found to get stabilized for all the samples. In the case of BICUTIVOX series of samples the conductivity values increase and

activation energy decrease with decreasing the amount of Ti. At low temperature, the highest conductivity is observed for $Bi_2V_{0.9}Cu_{0.1}Ti_xO_{5.35}$. Whereas, maximum value of conductivity at high temperature is observed for $Bi_2V_{0.9}Cu_{0.05}Ti_{0.05}O_{5.4.}$ It is also expected that electronic contribution to total conductivity at high temperature is higher for Ti-Cu double substituted compounds. For Nb doping in the composition $Bi_4V_{1.8}Cu_{0.2-x}Nb_xO_{10.7+3x/2}$ (x = 0.05, 0.1, 0.15) with the increase in doping the conductivity decreases. The maximum value of conductivity is observed for x = 0.5 sample. The value of conductivity is supposed to be on higher side than $Bi_4V_{1.8}Cu_{0.2}O_{10.7}$. The γ- phase is also found to get stabilized for x = 0.05 sample while the others being β- stabilized [28].

Emel'yanova *et al.* [29] discussed the synthesis, stable existence regions, structure, and migration characteristics of the BIMEVOX family experimentally and theoretically both. The dependence of conductivity on the temperature, composition and oxygen partial pressure has been reported. Synthesis of the samples with composition $Bi_4V_{2-2x}Me_{2x}O_{11-\delta}$ where Me^{n+} is a charged cation with n = 2-6 has been done via solid state reaction method. Theoretically, the interactions in β and γ- phase of undoped $Bi_4V_2O_{11}$ have been identified with the help of extended Huckel method. The covalent component of chemical bonds are obtained which shows the strength of bonds increases in way; Bi-V < Bi-O < V-O. The mean V-O bond population is found to be 1.3 times higher for the β than for γ- phase. On the similar grounds the total energy of β- $Bi_4V_2O_{11}$ is –1.822 k eV and decreases to –1.817 k eV for γ- phase. The differential V-O bond overlap theory proved that addition of transition metal cations like Cr, Mn, Vo, and Ni decreases the stability of γ- $Bi_4V_2O_{11}$ whereas, the substitution of isovalent cations like Nb and Ta increases the stabilization of γ- $Bi_4V_2O_{11}$. Theoretically, it can be concluded that fourfold and fivefold charged cations can be used as stabilizers of the crystal structure of γ-$Bi_4V_2O_{11}$. This conclusion has also been substantiated by experimental data. In order to obtain high values of conductivity at lower temperature thin film with composition

$Bi_2V_{0.9}Cu_{0.1}O_{5.35}$ has been deposited by spray pyrolysis technique on glass substrates. The electrical conductivity of thin film is observed ~ 5.7×10^{-2} Scm $^{-1}$ at 475 °C, which can be the onset temperature for low temperature SOFC applications [30]. Similarly the thin films of same composition $Bi_2V_{0.9}Cu_{0.1}O_{5.35}$ are deposited on alumina substrates, TGA-DTA studies confirmed that desired phase formation completes at 650 °C. The analysis of impedance spectroscopy revealed that most of the contribution to electrical conductivity is of grains. Also, the temperature dependent conductivity proved that the films synthesized can be used in low temperature SOFCs [31]. However, on comparing the electrical conductivity of the film on glass and alumina substrate, it is found that alumina substrate proves to be better candidate for SOFC application [32]. On increasing the amount of La_2O_3 in $Bi_4V_2O_{11}$ the melting point of the system as well as conductivity increases. The electrolytes synthesized are observed to be thermodynamically stable when placed in pure nitrogen and vacuum (0.133 Pa) and in pure reducing atmosphere (propane–butane at 650 °C) for 2 h [33]. Beg *et al.* [34] reported the effect of increase in Cd doping in the molecular formula $Bi_4V_{2-x}Cd_xO_{11-\delta}$; $0 \leq x \leq 0.25$. The γ- phase stabilization is occurred for $x \geq 0.175$. The maximum value of conductivity has been reported for x = 0.20 sample ~1.30×10^{-4} Scm $^{-1}$ at 420 °C. The conductivity studies of $Bi_4V_{2-x}Al_xO_{11-\delta}$ ($0 \leq x \leq 0.4$) samples exhibits that x = 0.2 composition shows the highest value of conductivity and further increase in amount of dopant decreases the value of conductivity. Since, the processing conditions like sintering temperature and time effects the conductivity so in order to optimize the sintering conditions x = 0.2 sample has been sintered at 750, 800 and 825 °C. The maximum conductivity is shown by the sample sintered at 800 °C for 12 h [3]. Another series of samples $Bi_4(V_{1-x}Me_x)_2O_{11-y}$ (x = 0-0.3, Me = Zr, Ga, Fe) synthesized via solid state route has also been reported. With the increase in value of 'x' the decrease in value of electrical conductivity is observed. Malys *et al.* [36] studied the effect of temperature on heavily doped $Bi_2V_{0.7}Mg_{0.3}O_{5.395-\delta}$,

system. No γ- phase transition is observed after the heat treatment. However, it leads to the phase separation above 650 °C. $Bi_2V_{0.7}Mg_{0.3}O_{5.395-\delta}$ reappears at 840 °C and is preserved on cooling as well. The lower values of conductivity in $Bi_2V_{0.7}Mg_{0.3}O_{5.395-\delta}$ system have been attributed to the oxide ion trapping in V^{5+} and Mg^{2+} environments. Phase transitions in $Bi_4V_{2-x}Ce_xO_{11-x/2-\delta}$ ($0.0 \leq x \leq 0.30$) series of samples have been investigated using XRD and High temperature XRD by Beg *et al.* [38]. It has been found that x = 0.15 sample shows $\alpha \rightarrow \beta$ and $\beta \rightarrow \gamma$ transitions whereas x = 0.25 presents only $\gamma \rightarrow \gamma'$ transition in the temperature range 450 -500 °C. According to another report no difference in crystal symmetry of undoped and doped system upto x = 0.15 is observed. At low temperatures, the conductivity of the samples decreases upto x = 0.25. This drop in conductivity reflects a strong anisotropic interaction between highly charged Ce^{4+} ion and oxide ion vacancy. On the other hand, at high temperature, conductivity decreases with dopant concentration [39]. The effect of doping of Hf with same valence as that of Ce has also been studied. $Bi_4V_{2-x}Hf_xO_{11-x/2-\delta}$ ($0.0 \leq x \leq 0.40$) has been synthesized through solid state route. The drop in value of low temperature conductivity accompanying the increase in activation energy is observed. At higher amount of dopant (x = 0.40), the distortion of γ- phase along with some β′- phase has been reported. La and Gd elements have been doped at Bi site for composition $Bi_{4-x}M_xV_2O_{11}$ ($0 \leq x \leq 0.4$). The samples have been synthesized via solid state reaction method. No γ- phase stabilization occurs for any of the composition synthesized. But, the increase in value of total conductivity as compared to parent compound suggests the increase in disorder and strain with doping which lead to increase the conductivity [40].

For Ti^{3+} doped bismuth vanadate samples ($Bi_4V_{2-x}Ti_xO_{11-\delta}$; $0 \leq x \leq 0.4$), the conductivity behavior is observed to follow the order $\sigma_{0.1} < \sigma_{0.2} < \sigma_{0.3} < \sigma_{0.4}$. Again the optimization of sintering temperature in the series proves that $Bi_4V_{1.6}Ti_{0.4}O_{11-\delta}$ compound sintered at 800 °C for 12h exhibits highest conductivity [41]. Taninouchi *et al.* [42] studied the behavior of

$Bi_2VO_{5.5}$ system with the doping of Li and Ag (monovalent atoms). The γ- phase is stabilized for x = 0.1 sample for both the dopants. From AC impedance spectroscopy the increase in conductivity of the samples is reported with doping. It has been observed that conductivity of Li and Ag doped system ~ 500 °C is better than that of $La_{0.8}Sr_{0.2}Ga_{0.8}Mg_{0.115}Co_{0.085}O_3$ which is one of the best known ionic conducting systems. However, the co-doping usually increases the thermal expansion coefficient.

Transition metal doping (M= Ti, Zr, Hf, Nb, Ta, Cr, Mo, W) doping in $Bi_2VO_{5.5}$ system effects the phase transitions largely. It has been observed that except for Cr, the β→γ transition temperature decreases as compared to parent compound. Also, with the transition metal doping, the thermal decomposition of $Bi_2VO_{5.5}$ into $BiVO_4$ and $Bi_3V_{1.2}O_{8.25}$ phases is suppressed in intermediate temperature [43].

$Bi_4Ba_xV_{2-x}O_{11—3x/2-\delta}$; $0.07 \leq x \leq 0.30$ samples have been synthesized and analyzed by Beg *et al.* [44]. It has been observed that γ- phase stabilization occurs for $0.17 < x \leq 0.30$. Higher values of conductivity are obtained for doped samples than undoped $Bi_4V_2O_{11-\delta}$. The highest value of conductivity ~ 4.45×10^{-5} Scm^{-1} at 300 °C is observed for x = 0.17. Beg *et al.* [45] also reported the effect of doping of Na in bismuth vanadate system. $Bi_2V_{1-x}Na_xO_{5.5-2x}$ ($0 \leq x \leq 0.20$) samples have been synthesized via sol- gel citrate route. In this case, the γ- phase is stabilized with $x \geq 0.15$ composition. The highest conductivity is observed for x = 0.13 sample. The value of conductivity is ~1.34×10^{-5} Scm^{-1} at 300 °C. $Bi_2V_{1-x}Cr_xO_{5.5+x-\delta}$ ($0.0 \leq x \leq 0.20$) series of samples have been prepared via microwave assisted solid state reaction method. γ- phase stabilization is not observed for any present doping. Also, the ac impedance spectroscopy analysis reveals that the electrical conductivity of microwave prepared samples is on the lower side. However, from the dielectric permittivity, it has been concluded that the charge accumulation at grain boundaries is significantly reduced [46]. Doping of Ca in

$Bi_4Ca_xV_{2-x}O_{11—3x/2-\delta}$; $0.07 \leq x \leq 0.30$ indicated that the stabilization of γ- phase at room temperature for $x \geq 0.17$. The conductivity of the samples is found to get increase with doping due to increase in disordering of the system. However, the maximum value of conductivity is obtained for x = 0.17 sample [47]. Structural and electrical conductivity behavior of $Bi_4V_{2-x}\ Ga_xO_{11-\delta}$; $0 \leq x \leq 0.4$ series as function of Ga^{3+} doping has also been reported. The conductivity values increase with doping. However, on increasing the doping above x = 0.2 the lower conductivity is observed due to introduction of impurity phases i.e. secondary phases [48]. Solid solutions of the general formula $Bi_4V_{2-x}Me_xO_{11-\delta}$,(Me=Fe, Cr, Nb) have been synthesized by means of hydrochemical, citrate-nitrate, mechanochemical and pyrolysis of polymeric-salt compositions methods. The stabilization of γ- phase is observed for Fe (x=0.2–0.5) and Nb (x=0.2–0.6) doped systems. From the analysis of impedance spectroscopy results, it is clear that Fe doped samples represents the maximum values of conductivity [49]. Solid solutions $Bi_4V_{2-x}Cu_{x/2}Ti_{x/2}O_{11-x}$ ($0.025 \leq x \leq 0.5$) known as BICUTIVOX have been synthesized by conventional solid-state synthesis, solid-state synthesis enhanced by mechanical activation, and through liquid precursors. The samples synthesized via conventional solid state reaction method exhibits the maximum value of electrical conductivity 2.5×10^{-2} Scm^{-1} at 750 °C [50]. According to Shao *et al.* [51] the doping of magnetic ions in $Bi_2VO_{5.5-\delta}$ has a large effect on electronic contribution to the total conductivity of the system. Both V and Bi site doped compounds with composition $Bi_2(V_{1-x}Mn_x)O_{5.5-\delta}$ and $(Bi_{2-x}Mn_x)VO_{5.5-\delta}$ (x=0.10–0.30) have been prepared via solid-state reaction. Results show that partial substitution on the V-site stabilizes γ- phase for compositions in the range of $0.10 \leq x \leq 0.25$. The solid solution limit obtained in this case is in accordance with equatorial vacancy model. In another study γ- phase stabilized, $Bi_2V_{1-x}\ Mn_xO_{5.5-x/2}$; $0.13 \leq x \leq 0.20$ samples have been synthesized by an ethylene glycol–citrate sol–gel route. The obtained xerogels are then calcined by the microwave heating using a modified domestic microwave

oven operated at 2.45 GHz. It is found that the microwave-assisted calcination route produces crystalline γ-BIMNVOX samples. It is observed that, these samples can be used as solid electrolyte in oxide-ion based electrochemical applications [52]. The optical, structural, and mechanical properties of $Bi_4V_{2-x}M_xO_{11-\delta}$ ($0 \leq x \leq 0.4$, M = Mn, Ga, As) oxides have also been investigated. After certain percent of doping, the secondary phase is formed in Mn, Ga and As doped $Bi_4V_{2-x}M_xO_{11-\delta}$ system. The band gap of the samples studied is found to get decrease upto the value of x = 0.2, on further increase in amount of doping, the band gap increases. The lowest band gap is observed for $Bi_4V_{1.8}Mn_{0.2}O_{11-\delta}$ sample. The fracture toughness and hardness of the samples increases with doping [53]. $Bi_4V_{2-x}Cd_xO_{11-3x/2-\delta}$; $0.0 \leq x \leq 0.25$ have been studied to derive a correlation between phase stability and oxide ion performance. The substitution of V^{5+} by Cd^{2+} represents different phase transitions for different compositions. It is observed that slow V^{4+}/V^{5+} re- oxidation results in increased defect trapping effects in the system at higher temperatures [54]. BICUVOX/ GDC composites have been synthesized with doped nano-ceria particulates $(Ce_{0.9}Gd_{0.1})O_2$ (GDC). The BICUVOX powder has been synthesized by a co-precipitation process which resulted in a homogenous, fine-grained powder with an average particle size of ~0.6 μm. It has been observed that GDC doping in BICUVOX matrix slows down the grain boundary mobility and hence restricts the grain size. The flexural strength level of the composite is found to be higher than BICUVOX systems [55]. $Bi_4V_{2-x}Nb_xO_{11}$ (BINBVOX) samples have been synthesized via ceramic and co-precipitation methods. The high-temperature γ-$Bi_4V_{2-x}Nb_xO_{11-\delta}$ is formed at $0.3 \leq x \leq 0.9$ irrespective of the synthesis method. The lowest partial oxygen pressure value within the stability range of BINBVOX at 750 °C is determined to be about $lgPO_2 = -12$ atm. Further, lowering of the partial oxygen pressure leads to the decomposition of the solid solutions. Higher values of conductivity are observed for $x < 0.3$ samples [56]. Similarly, $Bi_4V_{2-x}Me_xO_{11}$ (Me = Nb, Zr, Y and Cu and x = 0.0 and 0.02) have

been synthesized via solid state reaction method. The dielectric study revealed that materials are highly lossy and behave as ionic conductor [57]. Cu and Ti co- doped bismuth vanadate solution have been synthesized via hot forging technique. The relative density of hot forged $Bi_4(Cu_{0.05}Ti_{0.05}V_{0.90})_2O_{11}$ (BICUTIVOX) is ~ 98- 99%. Total conductivity of the samples is two orders greater in direction parallel to that of forging axes. Thus, impedance spectroscopy proves the thermal isotropic nature of the samples synthesized [58]. In another study, films of the above discussed composition have been prepared via aerosol deposition on alumina substrate. With the increase in temperature up to 500 °C, the particle size remains nano-scale while microstrain decreases rapidly resulting into the coarsening and texturing. Impedance measurements of films deposited on inter-digital electrodes revealed an annealing effect on the ionic conductivity, approaching that of bulk ceramic [59]. $Bi_2V_{0.9}Cu_{0.10-x}Mg_xO_{5.35}$; Mg and Cu co-doped series of samples has been synthesized via citrate sol- gel method by Beg *et al.* [60]. It is observed that double substitution leads to the stabilization of the tetragonal γ′-phase for x=0.06 and x=0.08. It is expected that, like single substitution, double substitution can also enhance the phase stabilization and oxide–ion conductivity of the BIMEVOX family. The highest value of conductivity is observed for x=0.06 ~ 1.5×10^{-3} Scm^{-1} at 300 °C. Khaerudini *et al.* [61] discussed the effect of sintering temperature on the conductivity of $Bi_4Mg_xV_{2-x}O_{11-\delta}$; $0.2 \leq x \leq 0.3$. It is found that for the samples sintered at 750 °C the conductivity behavior followed the trend $\sigma_{0.1} < \sigma_{0.2} < \sigma_{0.3}$, whereas for the samples sintered at 810 °C the trend followed is $\sigma_{0.1} < \sigma_{0.3} < \sigma_{0.2}$. Piva *et al.* [62] reported the synthesis and properties of composite solid electrolytes by varying the addition of 3 mol% yttria-stabilized zirconia (3Y-TZP) from 3 to 26 wt. % using a matrix of copper-substituted bismuth vanadate $Bi_2V_{0.9}Cu_{0.1}O_{5.35}$ (BICUVOX.1). It is observed that addition of 3Y-TZP in BICUVOX.1

inhibits the $\gamma \rightarrow \gamma'$ transition [63]. The conductivity values of different doped bismuth vanadate systems along with references are given in Table 2.1.

Table 2.1 Conductivity values of different doped bismuth vanadate system along with references.

Composition	T (˚C)	σ (Scm^{-1})	Remarks	Reference
$Bi_2V_{1-x}Ni_xO_{5.5-3x/2}$ ($0.06 \leq x \leq 0.25$)	300 (x = 0.12)	1.71×10^{-3}	• γ- phase stabilization is found to take place above x = 0.10	[9]
$Bi_2V_{1-x}Zn_xO_{5.5-x/2}$ ($0.05 \leq x \leq 0.27$)	300 (x = 0.10)	4.09×10^{-3}	• The low temperature conductivity increases with x over the whole composition, but small drop between x = 0.07 and 0.13 region is obtained.	[13]
$Bi_{4+y}V_{2-x-y}M_xO_{11-y-x}$ (M= Nd, Gd, Er, Yb)	300 (y = 0.0 and x = 0.2)	2.0×10^{-4}	• The conductivity of the samples is found to be independent of kind of dopant.	[14]
$Bi_4V_{2-x}Cu_xO_{11-x}$ ($0.07 \leq x \leq 0.20$)	300 (x = 0.15)	2.58×10^{-3}	• Above x = 0.15, the conductivity of the samples decreases due to interaction between defects.	[16]
Composite of $Bi_2V_{0.9}CO_{0.1}O_{5.35}$ and 3YSZ	300 (1 wt. % of YSZ)	2.2×10^{-2}	• The addition of 3Y-TZP (0.5 or 1 wt. %) can improve the mechanical properties of BICUVOX.1 ceramic without degrading its oxide-ionic conductivity.	[17]
$Bi_2V_{1-x}Cu_xO_{5.5-5x/2}F_{2x}$ ($0.10 \leq x \leq 0.20$)	300 (x = 0.10)	1.4×10^{-3}	• Drop in conductivity is observed which can be mainly due to the clustering or uniform distribution of F in vanadate layer at oxygen sites.	[18]
$Bi_4V_{2-x}P_xO_{11}$ $0.05 \leq x \leq 0.50$	300 Almost independent of x	1.0×10^{-5}	• The doping of P does not lead to stabilization of γ- phase alike other pentavalent ions.	[26]
$Bi_2V_{0.9}Cu_{0.1}O_{5.35}$ thin films	475	5.7×10^{-2}	• The obtained conductivity value suggests that this can be an onset temperature for low temperature SOFC applications.	[30]
$Bi_4V_{2-x}Cd_xO_{11-\delta}$ ($0 \leq x \leq 0.25$)	420 (x = 0.20)	1.3×10^{-4}	• It is observed that grain boundary contribution to the total conductivity of the samples decreases with increase in temperature.	[34]
$Bi_4V_{2-x}Ti_xO_{11-\delta}$ ($0 \leq x \leq 0.4$)	300 (x = 0.4)	2.6×10^{-5}	• The conductivity behavior is observed to follow the order $\sigma_{0.1} < \sigma_{0.2} < \sigma_{0.3} < \sigma_{0.4}$.	[41]
$Bi_4V_{2-x}Ba_xO_{11-3x/2-\delta}$ ($0.07 \leq x \leq 0.30$)	300 (x = 0.17)	4.4×10^{-5}	• Higher values of conductivity are obtained for doped samples than undoped $Bi_4V_2O_{11}$.	[44]
$Bi_2V_{1-x}Na_xO_{5.5-2x}$ ($0 \leq x \leq 0.20$)	300 (x = 0.13)	1.3×10^{-5}	• The γ- phase is stabilized with $x \geq 0.15$ composition.	[45]

As discussed above many researchers have reported the effect of dopants and their processing conditions on conductivity and thermal stability of γ- $Bi_4V_2O_{11-\delta}$. It has been reported that number of oxygen vacancies is more in case of quenched samples than in slow cooled samples [2]. As quenching from high temperature to room temperature prevents the re-oxidation of vanadium and stabilizes the high temperature disordered γ- $Bi_4V_2O_{11-\delta}$ at room temperature [22]. In most of the cases, these systems have been synthesized by solid state reaction method. Few reports have appeared in the literature for synthesis of $Bi_4V_2O_{11-\delta}$ by melt quench technique followed by the sintering at appropriate temperature. The objective of the present study is to investigate the effect of melt quench technique followed by sintering on γ- phase stabilization, phase transitions and conductivity with respect to the temperature. It is expected that the melt quench will not only increase the solid solubility limit of dopant but also easily stabilize the γ- phase at room temperature [16, 64].

Objectives

I. To synthesize $AO\text{-}Bi_2O_3\text{-}V_2O_5$ glass ceramics where A = Mg, Ca, Sr, Ba by Splat Quenching Method.

II. Physical parameters of these glass ceramics will be characterized to check their structural, thermal and topographical properties.

III. Electrical and transport measurement on these materials will be done for fuel cell applications.

To achieve the above mentioned objectives, the samples in the present study are synthesized by melt quench technique followed by sintering. These as prepared compounds are characterized by different techniques. The synthesis conditions and characterization techniques used in this work are discussed in the chapter 3. Chapter 3 incorporates the details of the materials used in synthesis of the selected composition. The chapter also explains the synthesis procedure and the characterization techniques applied to characterize the

synthesized samples. The results of selected system and discussions related to them are presented in chapter 4. The results obtained from characterization techniques namely X- ray diffraction (XRD), Fourier transform infra-red spectroscopy (FTIR), differential scanning calorimetry (DSC), scanning electron microscopy (SEM), ac impedance spectroscopy, UV/vis spectroscopy and Microwave Plasma Atomic Emission Spectroscopy (MP-AES) are discussed in detail. In the end of thesis, the conclusion and future scope of the present studied systems is given. Rietveld refinement for the quenched and sintered samples has been performed, in order to confirm the stabilized phase and calculate the unit cell parameters. FTIR spectroscopy of all the samples has also been carried out to observe the structural changes with dopant. The thermal stability of the samples has been evaluated with the help of dilatometry, differential thermal analyser and thermogravimetric analysis. The microstructural study of the sintered samples has been done to correlate the structure with the conduction behaviour of the prepared samples. MP-AES analysis of the selected quenched samples has also been done to confirm to initial and final stoichiometry of the samples synthesized. The conductivity of the samples is estimated with the help of two probe set up using impedance analyser. The obtained results are discussed in the light of structural ordering and disordering with the oxygen vacancy creation as the amount of doping changes. The substitution of vanadium by various alkaline earth metals has been prescribed. The sintering temperature effect has investigated on the selected system.

References

1. I. Abraham, F. Krok, Solid State Ionics 157 (2003) 139.
2. I. Abrahams, A.J. Bush, F. Krok, G.E. Hawkes, K.D. Sales, P. Thornton, W. Bogusz, J. Mater. Chem. 8(5) (1998) 1213.
3. Ravi Kant, K. Singh, O.P. Pandey, Int. J. Hydrogen Energ. 33 (2008) 455.
4. C. Vernochet, R.N. Vannier, M. Huve, C. Privano, G. Nowogrocki, G. Mairesse, G.V. Tendeloo, J. Mat. Chem. 10 (2000) 2811.
5. I. Abraham, F. Krok, J. A. G. Nelstrop, Solid State Ionics 90 (1996) 57.
6. S. Kim, M. Miyayama Solid State Ionics 104 (1997) 295.
7. A. Kezionis, W. Bogusz , F. Krok , J. Dygas, A. Orliukas, I. Abrahams, W. Gebicki Solid State Ionics 119 (1999) 145.
8. M.C. Steil, J. Fouletier, M. Kleitza, P. Labrune, J. Eur. Ceram. Soc.19 (1999) 815.
9. F. Krok, I. Abrahams, D. Bangobango, W. Bogusz , J.A.G. Nelstrop, Solid State Ionics 111 (1998) 37.
10. I. Abrahams, J.A.G. Nelstrop, F. Krok, W. Bogusz, Solid State Ionics 110 (1998) 95.
11. A.A. Yaremchenko, V.V. Kharton, E.N. Naumovich, V.V. Samokhval, Solid State Ionics 111 (1998) 227.
12. V. Jacobsoone , C. Follet-Houttemane, J.C. Boivin, Solid State Ionics 113–115 (1998) 607.
13. C.K. Lee, C.S. Ong, Solid State Ionics 117 (1999) 301.
14. K. Sooryanarayana, T.N. Guru Row, K.B.R. Varma, Mater. Res. Bull. 34 (3) (1999) 425.
15. F. Krok , I. Abrahams , A. Zadrozna , M. Małys , W. Bogusz , J.A.G. Nelstrop, A.J. Bush, Solid State Ionics 119 (1999) 139.
16. P.I. Paulin F., M.R. Morelli, S.C. Maestrelli, Mat. Res. Innovat. 3 (2000) 292.

17. M.H. Paydar, A.M. Hadian, K. Shimanoe, N. Yamazoe, J. Mater. Sci. 37 (2002) 2273.
18. I. Abrahams, J.A.G. Nelstrop, F. Krok, Solid State Ionics 136–137 (2000) 61.
19. M. Guillodo, J. Fouletier, L. Dessemond, P. Del Gallo, J. Eur. Ceram. Soc. 21 (2001) 2331.
20. M. Guillodo, J.M. Bassat, J. Fouletier, L. Dessemonda, P. Del Gallo, Solid State Ionics 164 (2003) 87.
21. A.A. Yaremchenko, M. Avdeev, V.V. Kharton, A.V. Kovalevsky, E.N. Naumovich, F.M.B. Marques, Mater. Chem. Phys. 77 (2002) 552.
22. F. Krok, I. Abrahams, M. Malys, W. Bogusz, J.R. Dygas, J.A.G. Nelstrop, A.J. Bush, Solid State Ionics 136–137 (2000) 119.
23. J.R. Dygas, M. Malys, F. Krok, W. Wrobel , A. Kozanecka , I. Abrahams, Solid State Ionics 176 (2005) 2085.
24. F. Krok, I. Abrahams, W. Wrobel, S.C.M. Chan, M. Malys, W. Bogusz, J.R. Dygas, Solid State Ionics 154–155 (2002) 511.
25. W. Wrobel, I. Abrahams, F. Krok, A. Kozaneck, S.C.M. Chan, M. Malys, W. Bogusz, J.R. Dygas, Solid State Ionics 176 (2005) 1731.
26. M. Alga, A. Ammar, R. Essalim, B. Tanouti, F. Mauvy, R. Decourt, Solid State Sci. 7 (2005) 1173.
27. M.H. Paydar, A.M. Hadian, G. Fafilek, J. Mater. Sci. 39 (2004) 1357.
28. M. Alga , A. Ammar , B. Tanouti , A. Outzourhit , F. Mauvy , R. Decourt, J. Solid State Chem. 178 (2005) 2873.
29. Y.V. Emel'yanova, R.R. Shafigina, E.S. Buyanova, V.M. Zhukovski, V.M. Zainullina, S.A. Petrova, Russ. J. Phys. Chem. 80 (11) (2006) 1725.
30. R.K. Nimat, C.A. Betty, S.H. Pawar, Appl. Surf. Sci. 253 (2006) 2702.
31. R.K. Nimat, R. S. Joshi, S.H. Pawar, Mater. Sci. Eng. B 137 (2007) 93.

32. R.K. Nimat, R.S. Joshi, S.H. Pawar, J. Alloy. Compd. 466 (2008) 341.
33. J. Chmielowiec, G.Pa´sciak, P. Bujło, J. Alloy. Compd. 451 (2008) 676.
34. S. Beg, N. A.S. Al-Areqi, Sadaf Haneef, Solid State Ionics 179 (2008) 2260.
35. E.A. Fortal'nova, V.V. Murasheva, M.G. Safronenko, N.U. Venskovskii, G.M. Kaleva, E.D. Politova, Russ. J. Phys. Chem. A (2008) 82 (10) 1633.
36. M. Malys, I. Abrahams, F. Krok, W. Wrobel, J.R. Dygas, Solid State Ionics 179 (2008) 82.
37. S. Beg, N.A.S. Al-Areqi, J. Phys. Chem. Solids 70 (2009) 1000.
38. N.A.S. Al-Areqi, S. Beg, Mater. Chem. Phys. 115 (2009) 5.
39. S. Beg, N.A.S. Al-Areqi Mater. Chem. Phys. 118 (2009) 15.
40. Deepti, Ravi Kant, M.L. Singla, K. Singh, Curr. Appl. Phys. 9 (2009) 1467.
41. Ravi Kant, K. Singh, O.P. Pandey, Mater. Sci. Eng. B 158 (2009) 63.
42. Yu-ki Taninouchi, T. Uda, T. Ichitsubo, Y. Awakura, E. Matsubara, Solid State Ionics 181 (2010) 719.
43. Yu-ki Taninouchi, T. Uda, T. Ichitsubo, Y. Awakura, E. Matsubara, Solid State Ionics 181 (2010) 1279.
44. S. Beg, Shehla Hafeez, N.A.S. Al-Areqi, Physica B 405 (2010) 4370.
45. S. Beg, A. Al-Alas, N.A.S. Al-Areqi, Mater. Chem. Phys. 124 (2010) 305.
46. S. Beg, A. Al-Alas, N.A.S. Al-Areqi, J. Alloy. Compd. 493 (2010) 299.
47. S. Beg, S. Hafeez, N. A. S. Al-Areqi, Phase Transitions 83 (3) (2010) 169.
48. Ravi Kant, K. Singh, O. P. Pandey, Ionics 16 (2010) 277.
49. M.V. Morozova, E.S. Buyanova, Ju. V. Emelyanova, V.M. Zhukovskiy, S.A. Petrova, Solid State Ionics 192 (2011) 153.
50. M.V. Morozova, E.S. Buyanova, Yu.V. Emelyanova, V.M. Zhukovskiy, S.A. Petrova, R.G. Zakharov, N.V. Tarakina, Solid State Ionics 201 (2011) 27.

51. Gang-Qin Shao, Xiao-Hua Yu, W. Cai, Hong-Xing Gu, J. Li, B. Li, Bo-Lin Wu, Shi-Xi Ouyang, Solid State Ionics 219 (2012) 20.
52. N.A.S. Al-Areqi, S. Beg, A. Al-Alas, S. Hafeez, J. Alloy. Compd. 581 (2013) 79.
53. G. Kaur, O. P. Pandey, K. Singh, Phys. Status Solidi A 209 (7) (2012)1231.
54. A. Al-Alas, S. Beg, N.A.S. Al-Areqi, Mater. Chem. Phys. 136 (2012) 15.
55. E. M. Sabolsky, S. Razmyar, K. Sabolsky, Mater. Lett. 76 (2012) 47.
56. E.S. Buyanova, M.V. Morozova, Ju.V. Emelyanova, S.A. Petrova, R.G. Zakharov, N.V. Tarakina, V.M. Zhukovskiy, Solid State Ionics 243 (2013) 8.
57. M. Roy, S. Sahu, S.K. Barbar, S. Jangid, J. Therm. Anal. Calorim. 113 (2013) 873.
58. P. Fuierer, M. Maier, J. Exner, R. Moos, J. Eur. Ceram. Soc. 34 (2014) 943.
59. J. Exner, P. Fuierer, R. Moos, Thin Solid Films 573 (2014) 185.
60. S. Beg, S. Hafeez, N.A.S. Al-Areqi, Solid State Ionics 261 (2014) 125.
61. D.S. Khaerudini, G. Guan, P. Zhang, X. Hao, Y. Kasai, K. Kusakabe, A. Abudula, J. Alloy. Compd. 589 (2014) 29.
62. R.H. Piva, D.H. Piva, J. Venturini, R. Florianoc, M.R. Morelli, Ceram. Int. 41(1) (2015) 171.
63. F. Krok, I. Abrahams, M. Malys, W. Bogusz, J.R. Dygas, J.A.G. Nelstrop, A.J. Bush, Solid State Ionics 136-137 (2000) 119.
64. F.M.L. Figueiredo, F.M.B. Marques, WIREs Energ. Environ. 2 (2013) 52.

Chapter 3
Experimental procedure

3.1 Raw materials

The appropriate amount of chemicals Bi_2O_3, MgO, CaO, SrO, $BaCO_3$ and V_2O_5 (Loba Chemie) were used for preparing the samples. The purity of all the chemicals was ~ 99.0%, and these chemicals were used, without further purification.

3.2 Sample preparation

The samples were synthesized via melt quench technique followed by sintering. The powders were taken according to the stoichiometric ratio $Bi_4ME_xV_{2-x}O_{11-\delta}$ (where x = 0.0, 0.05, 0.10, 0.15 and 0.20; ME= Mg^{2+}, Ca^{2+}, Sr^{2+} and Ba^{2+}). The chemicals were mixed thoroughly in an agate mortar pestle for 1 hour (h) in acetone media to obtain a homogeneous powder. The ground powder was allowed to melt at 1250 °C in recrystallized alumina crucible in a high temperature electric furnace. The furnace was held at intermediate temperatures 300, 600 and 900 °C for 0.5 h at each temperature, in order to increase the inter diffusion of constituents and avoid the loss of bismuth due to its high vapor pressure. The melt was held at 1250 °C for 0.5 h for homogeneous melting. After that, the melt was quenched in the air using two copper plates. The quenched sample was ground to form a fine powder. The obtained powder was pelletized into circular discs of diameter 1.5 cm by applying pressure ~ 10 kN cm^{-2}. The pellets obtained were sintered at 800 °C for 12 h in air ambient pressure followed by furnace cooling. Selected samples were also sintered at different temperatures 700, 750 and 800 °C to study the effect of sintering temperature on their conductivity.

3.3 Characterization

Both quenched and sintered samples were characterized to determine the phase stability, structural morphology, thermal stability and ac conductivity. The synthesized samples were characterized by X- ray diffraction (XRD), Fourier transform infra-red spectroscopy (FTIR), differential scanning calorimetry (DSC), scanning electron microscopy (SEM), ac impedance

spectroscopy, Microwave Plasma Atomic Emission Spectroscopy (MP-AES) and UV/vis spectroscopy. The details of these techniques are given in the following sections.

3.3.1 Density measurements

Density of the samples was measured on the basis of the fact that whenever an object is immersed in a liquid it experiences a force called buoyant force. It is an upward force which is equal to the weight of the liquid displaced by the immersed object. Thus, the weight of the sample is reduced by the buoyancy force when immersed in the liquid. The weight of the sample in air, w_a and weight of sample in liquid, w_b were used to calculate the density of the sample. The weight of the sample in air and liquid was measured by a precision balance. Xylene was used as a reference liquid in the experiment. The density of the sample was measured using the relation:

$$\rho_{sample} = \frac{w_a}{w_a - w_b} \times \rho_{xylene} \quad (3.1)$$

where ρ_{sample} is the density of the sample, ρ_{xylene} is the density of xylene i.e. 0.863 gcm^{-3}. The relative density (in %) is given by $\frac{\rho_{sample}}{\rho_{theoretical}} \times 100$; ρ_{sample} and $\rho_{theoretical}$ are experimental and theoretical densities, respectively. The theoretical density is measured by; $\rho_{theortical} = \frac{MZ}{N_a V}$, where, M is molar mass of material, N_a is Avogadro constant, Z is number of atoms per unit cell and V is volume of unit cell. In the present system 'Z' was taken equal to 6 for monoclinic superstructure and 1 for orthorhombic and tetragonal unit cell, respectively.

3.3.2 X-ray diffraction

Each crystalline solid has its unique characteristic X- ray diffraction pattern. X- ray diffraction technique can be used to identify crystal structure, interatomic distances, crystallite size, lattice parameters, lattice strain and crystal orientation of a crystalline solid. X-ray diffractometer consists of three elements X- ray tube, sample holder and an X- ray detector. A beam of electrons is generated in a cathode ray tube by heating a tungsten

filament. This beam of electrons is targeted towards a metal target commonly molybdenum, copper, cobalt and chromium. In the present study, copper target was used to obtain X-rays. The accelerated beam ejects the core electrons from the metal target and in result the outer shell electrons jump to the inner shell. During this process the emission of X- ray photon with the characteristic energy of the targeted material takes place. These X- rays are directed on the sample and the intensity of the reflected X-rays is recorded. The angle of the scattered beam can be used determine the distance between among different planes of atoms in a sample using Bragg's law: which is $2d \sin\theta = n\lambda$; where, d is lattice spacing (Å), θ is angle of incidence (degree), λ is wavelength of X-rays (Å) and n is an integer [1]. X-ray powder diffraction study was performed at room temperature using a PANalytical X'Pert PRO system with Cu Kα radiations (1.54 Å) and Ni filter. All the XRD patterens were taken on powder samples and the step size was 0.017°/ min.

3.3.3 Rietveld refinement

In rietveld analysis, a model is fitted to the experimental data. The rietveld algorithm optimizes the model function to minimize the weighted sum of squared differences, S_y between the observed intensities Y_{obs} and simulated or calculated intensities, Y_{calc}.

$$S_y = \sum w_i \left[y_{i(obs)} - y_{i(calc)} \right]^2 \tag{3.2}$$

Here, w_i is the weight and it is equal to $1/y_{i(obs)}$.

The goodness of fitting is estimated from the difference between observed and calculated reference patterns. There are other numerical terms which can also be used to estimate the goodness of the least square refinements. These residual values are defined as:

$$R_p = \sum \left[\frac{y_{i(obs)} - y_{i(calc)}}{y_{i(obs)}} \right]^2 \tag{3.3}$$

$$R_{wp} = \left| \frac{\sum w_i \left(y_{i(obs)} - y_{i(calc)}\right)^2}{\sum w_i \left(y_{i(obs)}\right)^2} \right|^{\frac{1}{2}} \quad (3.4)$$

$$\chi^2 = \frac{\sum w_i \left(y_{i(obs)} - y_{i(calc)}\right)^2}{n - p + c} = \left[\frac{R_{wp}}{R_{exp}}\right]^2 \quad (3.5)$$

where, *n* is number of observation, *P* is number of parameters and *c* is number of constraints in the definition of goodness of fit.

During the refinement process, all the residual parameters starts out large when the model is poor and decreases as the model produces better agreement with the experimental data [2]. In the present study, the structural parameters from XRD were refined by Rietveld refinement using FULLPROF setup.

3.3.4 Fourier transform infrared spectroscopy (FTIR)

Total energy of the molecule is estimated from the sum of its rotational, vibrational and electronic energy. Infrared spectroscopy is the study of the interactions between matter and electromagnetic field in the IR region. In the infra-red region, the molecule is excited after absorbing IR radiation. In general, a frequency will be absorbed if its photon energy coincides with the vibrational energy of the molecule. Thus, the peaks appearing in the FTIR spectra correspond to frequency of a vibration of a part of a sample molecule. For a molecule to show infrared absorptions it must possess a specific feature, i.e. an electric dipole moment of the molecule must change during the vibration [3]. Fourier Transform Infrared (FTIR) absorption spectra of the samples were taken by Perkin Elmer- Spectrum-RX FTIR spectrometer in 400 - 1600 cm^{-1}. The samples were prepared by mixing 5 mg of sample to be analyzed with 20 mg of KBr. The spectrum of each sample was normalized to the spectrum of the blank KBr. All the spectra were taken at room temperature with resolution ~ 0.8 cm^{-1}.

3.3.5 Thermal analysis

Thermal analysis comprises of the techniques that involve the measure of material's response during heating and cooling. During thermal analysis the main aim is to establish relation between temperature and physical properties of the material. The main characterization techniques performed in the present study are listed below [4, 5]:

3.3.5.1 Dilatometry

Dilatometry measures the expansion or contraction behavior of the solid materials with respect to temperature. The change in length per unit starting length is conventionally recorded as a function of temperature. The slope of the measurement is the coefficient of linear thermal expansion, $\alpha_{l;}$

$$\alpha_l = = \frac{1}{l_o}\left(\frac{\partial l}{\partial T}\right) \tag{3.6}$$

Where l_o is the original length and $\partial l/\partial T$ denotes the change in length of specimen. The TEC of a material depends on the attractive and repulsive forces between the atoms in a solid. The energy of the system increases with increase in temperature and the atoms vibrate to greater and shorter distances about a mean position. The repulsive forces between the atoms increase more rapidly than attractive ones. Thus, at a particular energy (i.e. temperature) the atoms can move farther apart more rapidly than they are pushed together. Weakly bonded atoms expand at higher rates with temperature and show higher TECs. The thermal expansion coefficient (TEC, α_l) is an important parameter for any material to be used in SOFC. The thermal expansion mismatch can cause thermal stresses in the materials and degrade its overall performance. The thermal expansion coefficient of the samples was determined by using pushrod Netzsch DIL 402 PC dilatometer in the temperature range 30 - 750 °C at a heating rate of 5 °C/min in air at atmospheric pressure. The polished rectangular bars of dimensions 1.5-2 mm were used for the measurements. The resolution limit of the instrument is 9 nm.

3.3.5.2 Differential scanning calorimetry (DSC)/ Thermal gravimetric analysis (TGA)

In DSC analysis, the temperature difference between the sample and reference sample is determined as a function of time. The reference sample is a material, which does not undergo any kind of transformation in the temperature range of interest. DSC setup consists of two separate containers for reference and sample. They are associated with individual heating elements and temperature measuring devices. The sample and reference materials are heated equally; as the sample temperature deviates infinitesimally from the reference sample the temperature measuring device detects it. The heating element reduces the heat input to one cell while adding heat to other in order to maintain a zero temperature difference called 'null balance' between the sample and reference. In order to maintain the null balance the amount of electrical energy supplied per unit time is proportional to the heat released per unit time by the sample. TG analysis is used to determine the weight gain or loss in the sample due to gas release or absorption as a function of temperature.

DSC/TGA analysis of the present samples was carried out with the help of NETZSH Zupiter STA 449 F3 simultaneous thermal analyzer in commercial argon (Ar) atmosphere with 20 °C/min heating rate.

3.3.6 Scanning electron microscopy (SEM)/ Energy dispersive spectroscopy (EDS)

SEM is an important tool for microstructural and morphological analysis of a sample. Magnification ~ 10^6 times can be obtained from scanning electron microscope. Thus, larger area can be focused at one time. Scanning electron microscope produces images by using a beam of electron beam generated by a tungsten filament or lanthanum hexaborate with the application of voltage. From the SEM analysis one can determine the effect of processing conditions on the microstructural features of a sample. With the help of SEM analysis and attached EDS chemical composition and crystalline structure can also be determined. SEM is also useful in qualitative or semi-qualitative analysis of elements present in the sample. This

technique involves the addition of an assembly to scanning electron microscope and is known as EDS. Scanning electron microscopy in the present case was carried out with the help of scanning electron microscope JEOL/EO (version 1.0). The SEM study was carried out on fractured gold-sputtered sintered pellets. The elemental analysis of prepared samples was carried out using energy dispersive X-ray spectroscopy (EDS) analysis using attachment OXFORD instruments INCA-X act.

3.3.7 Electrical conductivity measurement

Impedance spectroscopy is a powerful method of characterizing electrical properties of their materials and their interfaces with electronically conducting electrodes. It can also be used to investigate the dynamics of bound or mobile charges in the bulk or interfacial regions of any material under study. Impedance spectroscopy basically studies the system response to the application of periodic ac signal with small amplitude. The real and imaginary parts of impedance with respect to frequency are measured, keeping the temperature constant. - Z″ versus Z′ plots namely Nyquist plots can be used to determine the resistance and capacitance of the samples. The temperature dependence of electrical conductivity can be analyzed by plotting the graphs log (σ T) versus 1000/T.

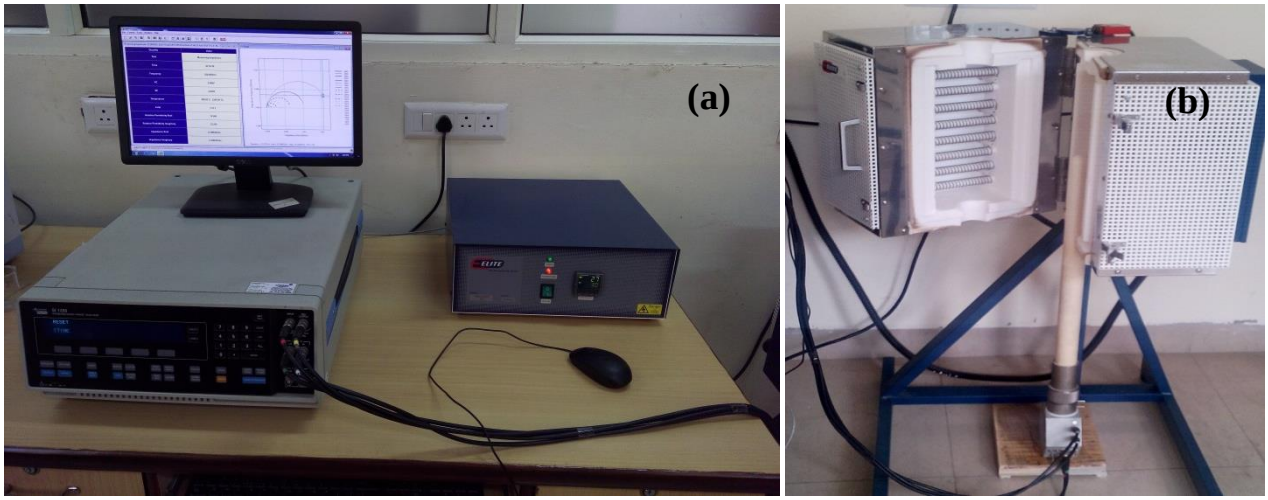

Figure 3.1 (a) SI-1260 Solartron analytical LCR meter and (b) NorEcs probostat with sample holder.

The activation energy is calculated from the slope of Arrhenius plots as follows;

$$\sigma T = \sigma_o \exp(-E_a/k_B T) \quad (3.7)$$

where σ_o is the pre-exponential factor, E_a is the activation energy, k_B is Boltzmann's constant and T is the absolute temperature [7]. The two probe ac conductivity measurements were done on gold sputtered pellets using an ac impedance spectroscopy with model SI-1260 Solartron analytical LCR meter. The measurement is performed in air by keeping the heating rate of 10 °C min^{-1} with temperature stability ±1 °C in the frequency and temperature range of 1 -10^7 Hz and 200-750 °C, respectively. The obtained results were fitted with Z-view software to get the capacitance and resistance values at different temepartures.

3.3.8 UV/vis spectroscopy

UV/vis spectroscopy deals with the interaction of radiation with matter. Absorption of light (i.e. energy) increases the energy of the molecules and causes a transition between the different electronic energy levels. Since, different molecules/ atoms absorb UV/ vis radiation at different wavelength, UV/ vis spectroscopy is used in identification of substances through the spectrum emitted from or absorbed by the sample. The value of band gap can be calculated from the absorption edge for the transmission spectra as well as reflectance spectra. According to Mott and Davis in the transmission spectra the region with absorption coefficient, α in the range 10^4 - 10^6 cm^{-1} relation (3.8) is followed.

$$\alpha h\nu = B\,(h\nu - E_g)^r \quad (3.8)$$

where $h\nu$ is the photon energy, E_g is the optical band gap, and r is the index which can have different values (2, 3, 1/2, and 3/2) depending on the transition process such as indirect allowed, indirect forbidden, direct allowed and direct forbidden transitions, respectively. B is a constant and is called the band tailing parameter. The values of the band gap can be calculated by extrapolating the linear portion of the graph between $(\alpha h\nu)^r$ and hν [8-11]. For the powder sample diffuse reflectance spectra is obtained. Since powder is a continuous

medium and can behave as an infinite medium the Kubelka – Munk relation can be applied reflectance spectrum. For an infinite layer, the infinite thickness absorption coefficient α can be related to sample reflectance (R) by the following relation as given in equation (3.9)

$$F(R) = (\alpha/s) = (1 - R)^2/2R \quad (3.9)$$

Where *R* is the reflectance and *s* is the scattering coefficient. The band gap value in different samples can be calculated by the extrapolation of the straight line $[F(R)h\nu]^n = 0$ from the graph between $[F(R)h\nu]^n$ and hν, where, *n* is the index and depends on the transition process such as indirect allowed, indirect forbidden, direct allowed and direct forbidden transitions. The values of band gaps are calculated from the graphs by taking n = 2 i.e. for direct allowed transitions. Another parameter which can be calculated from the UV spectra is the Urbach energy which is the measure of disorderdness and randomness of the material. It can be represented by the relation (3.10)

$$\alpha(\nu) = \alpha_0 \, exp \, (h\nu/\Delta E) \quad (3.10)$$

where α_0 is a constant and ΔE is the Urbach energy representing the disorderdness in the system. The value of Urbach energy can be calculated from the inverse of the slope of the linear portion of the graph between ln α and hν. Here, the Urbach energy is calculated from the graph between ln F(R) and hν. In the present work, the UV/vis analysis of the samples is done to estimate the amount of disorderdness generated in the system with the introduction of dopant atoms [12, 13].

UV- Visible diffuse reflectance spectra of the powder samples were recorded by using HITACHI U-3900 H spectrophotometer, double-beam double-monochromator system, with a spectral range from 200 – 800 nm. In the present case reflectance spectrum is taken of the powder sample by calibrating the instrument with and without standard sample by taking reflectance equal to 100 and 0%, respectively.

3.3.8 Microwave Plasma Atomic Emission Spectroscopy (MP-AES)

Microwave Plasma Atomic Emission Spectroscopy (MP-AES) was used to determine the elemental concentration of selected quenched samples. Plasma is an electrical conducting gaseous mixture containing a significant concentration of cations and anions. The concentrations of both the species cations and anions are such that the net charge approaches zero. Ions in the plasma absorb power from an external source to maintain the temperature at a level at which further ionization helps to sustain the plasma. Samples are introduced into the plasma flow by nebulizers. The fine droplets of the sample to be analyzed are carried into the plasma. Ionization interference effects of both plasma and sample are noted. In the present case, the analysis was carried out with an AGILENT MP-AES 4100, with a spectral resolution of 25-40 pm. The samples for MP-AES analysis were prepared by adding 0.1 g of sample to a solution of 10 ml nitric acid and 25 ml water. The prepared solution was heated to reduce it upto 50% of initial solution. After that, the obtained solution was diluted by adding 100 ml water. The MP-AES experiments were repeated three times for each elemental analysis.

References

1. B. D. Cullity, Elements of X Ray Diffraction Edt. 1 Prentice Hall New Jersey (2001).
2. B.H. Toby, Powder Diffraction 21 (2006) 68.
3. B. C. Smith, Fundamentals of Fourier Transform Infrared Spectroscopy Edt. 2 CRC Press USA (2003).
4. J. D. Menczel, R. B. Prime, Thermal analysis of polymers fundamentals and applications John Wiley & Sons, Inc., Hoboken, New Jersey (2009).
5. R.F. Speyer, Thermal analysis of materials Marcel Dekker, New York (1994).
6. B. L. Gabriel, SEM: A user's manual for Materials Science Amer. Soc. Metals Park Ohio USA (1985).
7. G. Kaur, M. Kumar, A. Arora, O. P. Pandey, K. Singh, J. Non-Cryst. Solids 357 (2011) 858.
8. W.W.M. Wendlant, H.G. Hecht, Reflectance Spectroscopy – Chemical Analysis 21, Interscience Publishers (John Wiley & Sons), New York (1966).
9. B. Tirloni, E. S. Lang, G. M. de Olivira, Polyhedron 62 (2013) 126.
10. V. Kumar, A. Sharma, D.K. Sharma, D.K. Dwivedi, Optik 125 (2014) 1209.
11. J. Tauc, A. Menth, J. Non Cryst. Solids 8 (1972) 569.
12. I. Pal, A. Agarwal, S. Sanghi, Indian J. Pure Appl. Phys. 50 (2012) 237.
13. R. K. W. Jr., W. Y. Hsu, J. Appl. Physics 54 (1983) 4093.

Chapter 4
Results and discussion

Doped bismuth vanadate can be a good choice as solid electrolyte for intermediate temperature solid oxide fuel cells (IT-SOFCs). It has been reported that due to the presence of inherent oxygen vacancies, $Bi_4V_2O_{11-\delta}$ exhibits good conductivity in intermediate temperature ranges (600 - 800 °C). The degree of disorderdness of the $Bi_4V_2O_{11-\delta}$ can be increased by proper doping of some metal cations at vanadium site. Depending on the degree of disorderdness and temperature, it has three types of interconvertible polymorphs α, β and γ. Out of all the three polymorphs, high temperature γ- polymorph is highly disordered and can be stabilized at room temperature [1-3]. The substitution of V by divalent cations results an increase in vacancy concentration in $(V_2O_5)^{2-}$ layer by lowering the coordination number of vanadium. Thus, highly disordered high temperature γ- polymorph can be stabilized by doping of divalent cations at V site in $Bi_4V_2O_{11-\delta}$ [4-7]. Secondly, the doping of divalent cations at V site in $Bi_4V_2O_{11-\delta}$ not only increases the total conductivity but also some times increase the density in comparison to undoped bismuth vanadate [6]. In addition to this, various researchers reported that quenching the samples from high temperature to room temperature enhances the possibility of stabilization of γ- phase to room temperature at lower dopant concentration. Thus, quenching of the samples can help in stabilization of γ-polymorph at lower amount of dopants. Considering the above points the $Bi_4V_{2-x}ME_xO_{11-\delta}$ (where $0.0 \leq x \leq 0.20$; ME= Mg^{2+}, Ca^{2+}, Sr^{2+} and Ba^{2+}) are synthesized by melt quench technique followed by sintering at 800 °C for 12 h. As given in chapter 3 (Experimental Techniques), the synthesized samples whether quenched or sintered are characterized by various techniques. The obtained results are discussed in the light of difference in ionic radii of host and dopants, oxygen vacancies, disordering and different crystalline phase stabilization in the samples.

4.1 $Bi_4V_{2-x}ME_xO_{11-\delta}$ ($0.0 \leq x \leq 0.20$; ME = Mg^{2+})

Undoped and Mg^{2+} doped, $Bi_4V_{2-x}ME_xO_{11-\delta}$ ($0.0 \leq x \leq 0.20$; ME = Mg^{2+}) samples are synthesized by melt quench technique followed by sintering at 800 °C for 12 h. The synthesized samples are characterized by following techniques. The results have been discussed in light of change in processing conditions and doping on phase stabilization, density and conductivity of the synthesized samples.

4.1.1 X-ray diffraction analysis

The rietveld refined XRD patterns of quenched and sintered samples obtained with the help of FULLPROF software are shown in Figure 4.1 and 4.2 [8]. The various refined parameters are listed in Table 4.1. The diffraction pattern of sample $Bi_4V_{2-x}Mg_xO_{11-\delta}$ (x = 0.0) exhibit a superstructure peak at ~ 24.4°. The presence of this XRD peak indicates α- phase with space group *C2/m* formation in x = 0.0 sample [8]. The XRD pattern of sintered sample (x = 0.0) could not show any appreciable change except some changes in XRD peaks broadening. In the sintered sample, XRD peaks become broader than quenched samples. On the other hand, the XRD peak at ~ 32° becomes singlet for x = 0.05- 0.20. It indicates that γ- phase with space group *I4/mmm* gets stabilized in quenched samples at room temperature [1]. The γ- phase is stabilized at lower dopant concentration as compared to earlier reported values for the similar systems [3]. Whereas, the sintering of quenched samples transforms γ to β- phase with *Amam* space group in x = 0.05, 0.10 and 0.20. After sintering, the XRD peak at ~ 32° and ~ 48° becomes doublet and singlet, respectively, in these systems [4, 8]. The transformation of γ to β- phase, after sintering, in x = 0.05, 0.10 and 0.20 samples, may be related to the oxygen vacancies and their distribution. Krok *et al.* [3] have reported similar transformation, β→γ→β, with dopant concentration in $Bi_4V_2O_{11-\delta}$ system. However, the phase transitions have been reported at higher dopant concentration as compared to the present system. Initial dopant concentration, i.e. x = 0.05 and 0.10 in $Bi_4V_{2-x}Mg_xO_{11-\delta}$ creates

whatever oxygen vacancies by doping, have some ordering. After reaching a certain amount of oxygen vacancies there might be a random distribution and leads to stabilization of γ-phase in $Bi_4V_{1.85}Mg_{0.15}O_{11-\delta}$. Further increase in dopant concentration enhances the ordering of oxygen vacancies and transform from γ to β- phase as observed in $Bi_4V_{1.80}Mg_{0.20}O_{11-\delta}$.

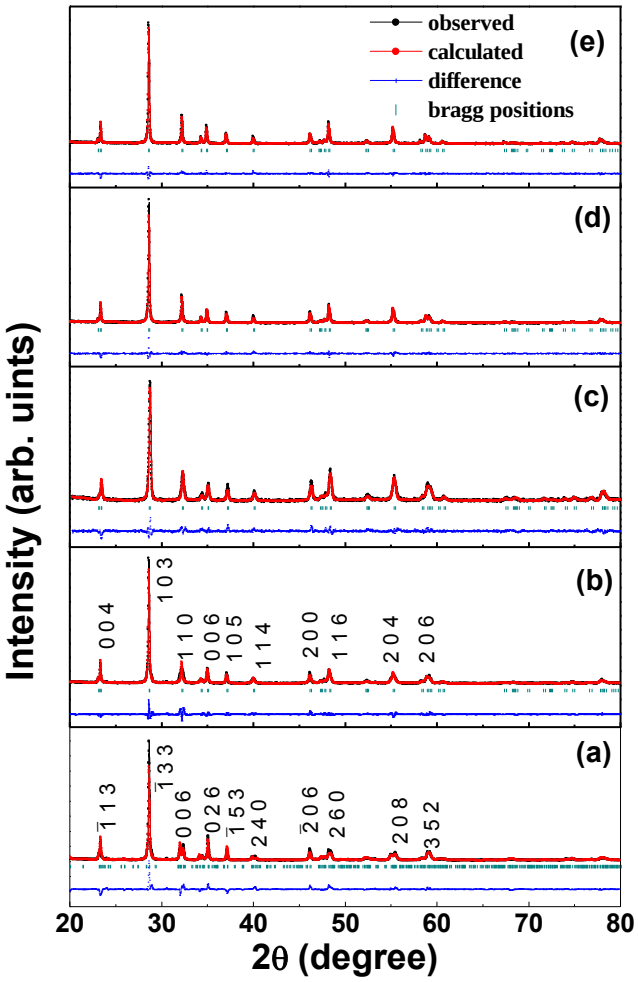

Figure 4.1 XRD patterns of quenched $Bi_4V_{2-x}ME_xO_{11-\delta}$ ($0.0 \leq x \leq 0.20$; ME = Mg^{2+}) (a) x = 0.0, (b) x = 0.05, (c) x = 0.10, (d) x = 0.15 and (e) x = 0.20.

It seems that the size difference between dopant Mg^{2+} (0.72 Å) and host V^{5+} (0.54 Å) play crucial role in phase transformations like, β→γ→β, with dopant concentration. However, the quenched samples show lower full width at half maxima (FWHM) than sintered samples of similar composition. It is the opposite trend observed in general for quenched and sintered samples. It might be associated with the reduction of V^{5+} to V^{4+}. In order to maintain the neutrality of the system, the oxygen vacancies are created, so quenched samples should have

more disordering. On the other hand, during sintering re- oxidation of V is taken place, which accompanied with the conversion of VO_4 to VO_6 polyhedra [9-11].

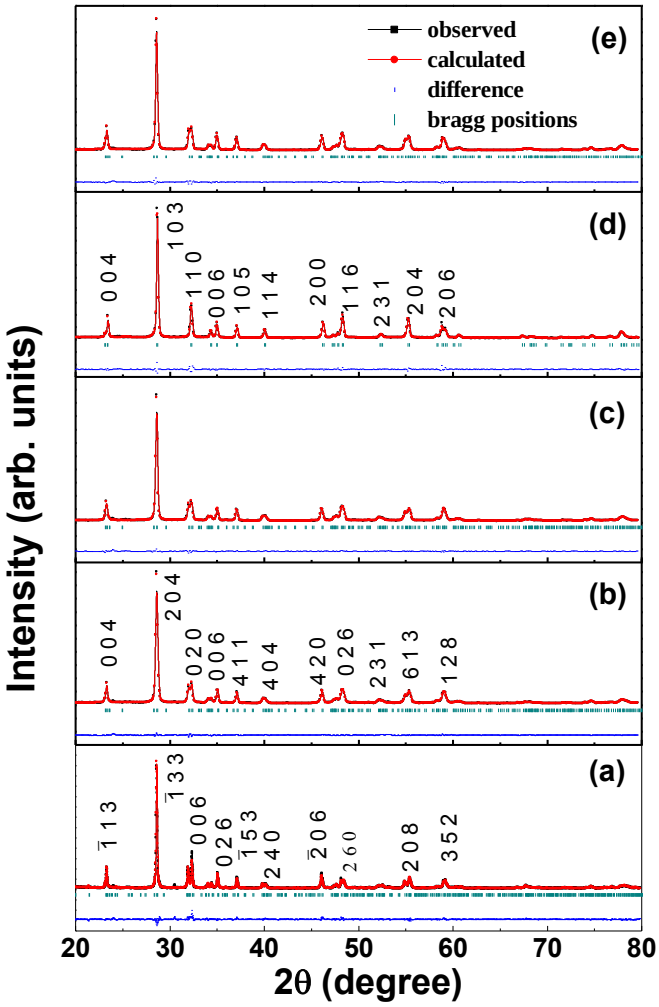

Figure 4.2 XRD patterns of sintered $Bi_4V_{2-x}ME_xO_{11-\delta}$ ($0.0 \leq x \leq 0.20$; ME = Mg^{2+}) (a) x = 0.0, (b) x = 0.05, (c) x = 0.10, (d) x = 0.15 and (e) x = 0.20.

Obviously, sintered samples contain lower oxygen vacancies than quenched samples due to oxidation of V^{4+} to V^{5+}. The lattice parameter 'c' increase with increasing doping as observed for quenched samples. This increment in the 'c' parameter can be attributed to the difference in the ionic radii of dopant cation Mg^{2+} (0.72 Å) and host cation V^{5+} (0.54 Å). Also, the increase in value of 'c' parameter can be related to the increase in oxygen deficiency with the increase in amount of doping. Actually, there are two kinds of oxygen atoms in the $(VO_{3}\square_{0.5})^{2-}$ layer equatorial and apical, whenever the lower valence cation substitutes the V^{5+}

cation the equatorial oxygen vacancies are generated and the lone pair of Bi^{3+} tend to push the apical bonds due to this compression the equatorial bonds get elongated resulting into the increase in the value of 'c' lattice parameter [12, 13]. Whereas, the decrease in 'c' parameter is observed, for sintered samples confirming the $\gamma \rightarrow \beta$ transition, with the increase in amount of doping [14, 15]. As the dopant increases the increase in unit cell volume also increases in both kinds of samples (as quenched and sintered). It can be attributed to the greater ionic radii of Mg^{2+} than V^{5+}. This kind of behaviour is also reported for β- BIMEVOXes [16, 17].

The densities of all the samples calculated using Archimedes principle are listed in Table 4.5 The strain induced in the lattice can be calculated with the help of Williamson Hall analysis [18]. Using, Williamson Hall method both crystallite size and strain induced in the lattice can be calculated. Williamson Hall method assumes that both the particle size and strain contribution to the line broadening are independent of each other. Therefore, the line broadening observed due to both the parameters can be written as the sum of both the contribution. Thus, the strain generated in the lattice can be calculated using the Williamson Hall equation as follows:

$$\beta \cos\theta = \frac{K\lambda}{D} + 4\varepsilon \, sin\theta \qquad (4.1)$$

where, β is FWHM, K is the shape parameter (0.9), λ is incident wavelength of X-rays and ε is the strain induced in the crystal lattice. The plot βcosθ versus 4sinθ was drawn and the value of strain generated in the lattice was calculated from the slope obtained from the linear fit of data [19, 20].

Table 4.1 Rietveld refined parameters for quenched and sintered $Bi_4V_{2-x}ME_xO_{11-\delta}$ ($0.0 \leq x \leq 0.20$; ME = Mg^{2+}).

Quenched samples					Goodness parameters of fitting		Sintered samples				Goodness parameters of fitting	
Composition	**a (Å)**	**b (Å)**	**c (Å)**	**Volume ($Å^3$)**	**R_{exp}**	**χ^2**	**a (Å)**	**b (Å)**	**c (Å)**	**Volume ($Å^3$)**	**R_{exp}**	**χ^2**
$Bi_4V_2O_{11-\delta}$	5.587	15.350	16.596	1423.445	6.94	2.67	5.599	15.338	16.599	1425.664	8.46	2.18
$Bi_4V_{1.95}Mg_{0.05}O_{11-\delta}$	3.929	3.929	15.372	237.310	9.04	2.03	11.077	5.593	15.362	951.711	3.64	2.82
$Bi_4V_{1.90}Mg_{0.10}O_{11-\delta}$	3.921	3.921	15.362	236.241	9.82	1.38	11.078	5.594	15.362	952.074	3.67	2.43
$Bi_4V_{1.85}Mg_{0.15}O_{11-\delta}$	3.928	3.929	15.403	237.755	9.41	1.27	3.929	3.929	15.405	237.797	3.61	3.47
$Bi_4V_{1.80}Mg_{0.20}O_{11-\delta}$	3.929	3.929	15.421	238.089	9.01	1.16	11.085	5.589	15.382	953.056	3.60	2.46

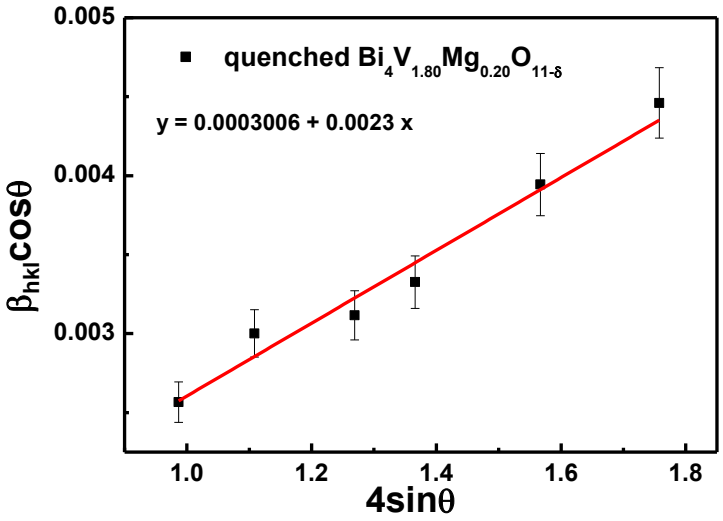

Figure 4.3 Williamson Hall plot for quenched $Bi_4V_{1.80}Mg_{0.20}O_{11-\delta}$.

The representative Williamson Hall plot for quenched $Bi_4V_{1.80}Mg_{0.20}O_{11-\delta}$ is shown in Figure 4.3. The values of strain are observed to be positive depicting the tensile strain generated in the present system. The tensile strain observed in the samples can be attributed to the greater ionic radii of dopant atom than that of host atom [21].

4.1.2 Analysis of FTIR spectra

The FTIR spectra of composition $Bi_4V_{2-x}Mg_xO_{11-\delta}$ (where x = 0.0 - 0.20) for quenched and sintered samples are shown in Figure 4.4 and 4.5. The different bands obtained in the spectra can be assigned to the vibrations of different bonds. The assignments of different bands are presented in Table 4.2. The FTIR spectra of bismuth vanadate exhibits absorption bands, namely at ~ 468 cm^{-1}, ~ 519 cm^{-1}, ~ 624 cm^{-1}, ~ 732 cm^{-1}, ~ 767 cm^{-1} and ~ 801 cm^{-1}. Bands appearing in the spectra at ~ 468 cm^{-1} and ~ 519 cm^{-1} can be due to the symmetric bending vibration of Bi-O bonds in BiO_3 pyramidal units. Whereas, the band due to the vibration of symmetric modes of V- O-V bonds can be assigned to the band at ~ 732 cm^{-1}. The vibrations due to V- O-V chains could have generated the absorption band at ~ 801 cm^{-1} [22- 25]. With the change in amount of doping and sintering the structural changes in the system are taking place as observed in FTIR spectra in Figure 4.4 and 4.5. As the amount of doping increases the shift in bands towards higher wavenumber side is observed. The shifting of bands towards

higher side can be due to the difference between the mass and size of the host and dopant [25-27]. With the increase in amount of doping the broadening in bands at ~ 727 and ~ 810 cm^{-1} is observed. The broadening of bands can be explained on the basis of addition of number of vibrational bands arising due to the variation in the bond lengths and angles. With the increase in amount of doping in quenched as well as sintered samples the bands at ~ 615 and ~ 912 cm^{-1} start disappearing. It indicates the incorporation of Mg^{2+} in VO_4 polyhedrons [28].

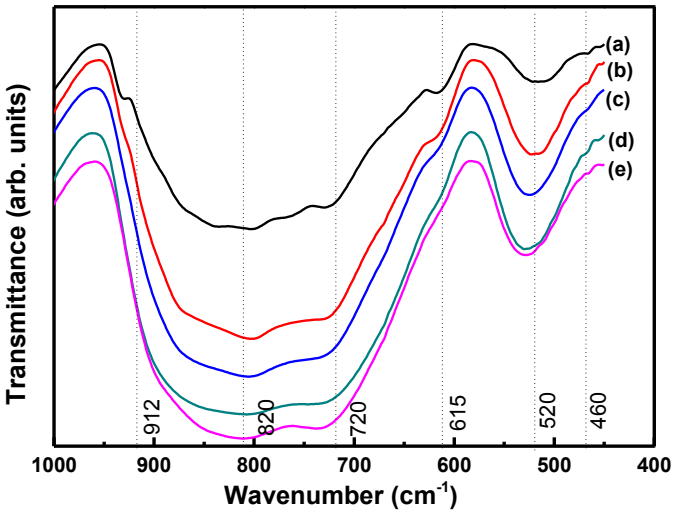

Figure 4.4 FTIR spectra for quenched $Bi_4V_{2-x}ME_xO_{11-\delta}$ ($0.0 \leq x \leq 0.20$; ME = Mg^{2+}) (a) x=0.0, (b) x=0.05, (c) x=0.10, (d) x=0.15 and (e) x=0.20.

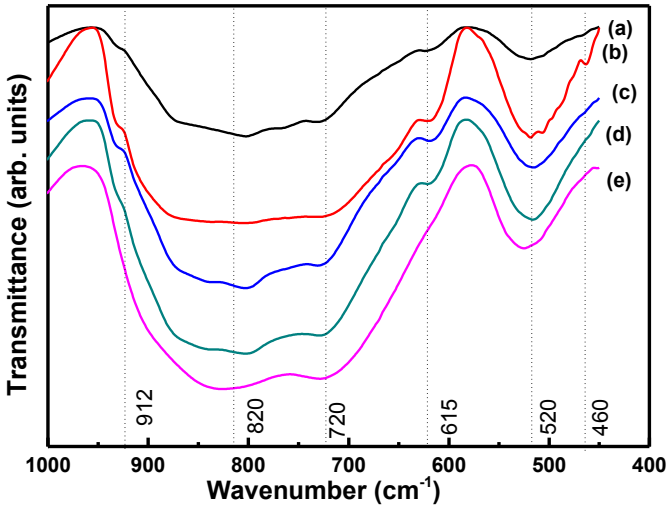

Figure 4.5 FTIR spectra for sintered $Bi_4V_{2-x}ME_xO_{11-\delta}$ ($0.0 \leq x \leq 0.20$; ME = Mg^{2+}) (a) x=0.0, (b) x=0.05, (c) x=0.10, (d) x=0.15 and (e) x=0.20.

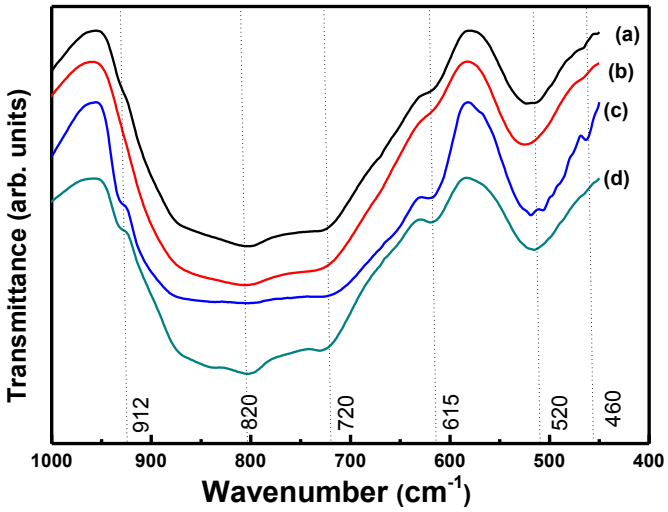

Figure 4.6 FTIR spectra for $Bi_4V_{2-x}ME_xO_{11-\delta}$ (x=0.05 and 0.10; ME = Mg^{2+}) (a) quenched x=0.05, (b) quenched x=0.10, (c) sintered x=0.05 and (d) sintered x=0.10.

The shifting of bands towards lower wavenumber with sintering might be associated with the oxygen vacancies [29]. This shifting is particularly prominent in BiO_3 band at ~ 519 cm^{-1} as shown in Figure 4.6. In addition to this, the sintered samples also exhibit sharper band at ~ 912 cm^{-1} as compared to quenched samples. It is manifested that V preferably occupy the tetrahedral sites in sintered samples.

Table 4.2 Assignment of different band positions in FTIR spectra of quenched and sintered $Bi_4V_{2-x}ME_xO_{11-\delta}$ ($0.0 \leq x \leq 0.20$; ME = Mg^{2+}).

Wavenumber (cm^{-1})	Assignment
~ 460	Bending modes of V- O-V bonds
~ 519	Symmetric bending vibrations of Bi-O bonds from BiO_6 groups
~ 616	Symmetric bending vibration of Bi-O bonds in BiO_3 polymorphs
~ 732	Symmetric modes of V- O-V bonds
~801	Vibrations due to chains of V- O-V bonds
~ 912	Vibrations of VO_4 polyhedra

4.1.3 Microstructural analysis

SEM micrographs of all the sintered samples show the intermingled grains with non-uniform size (Figure 4.7). The range and average grain size is indicated in Figure 4.8. Higher deviation of grain size from its mean value indicates that the grain size for all the samples is spread out over a large number of values [30]. The non- uniformity in the grain size can be related to the grain growth kinetics during sintering due to boundary to boundary movement. Since, the grain boundary energy depends on the grain boundary orientation and mobility [31, 32]. The smaller grain size is observed in sintered samples than quenched samples.

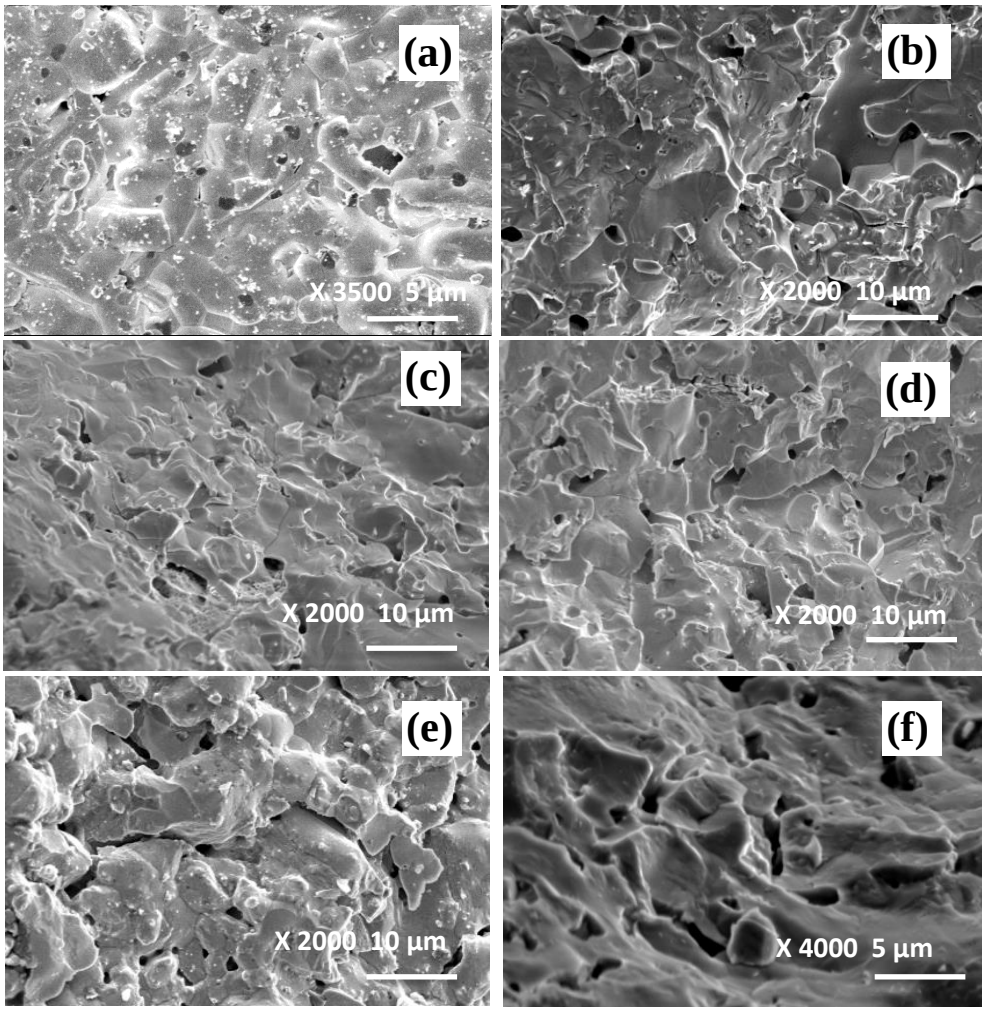

Figure 4.7 Scanning electron micrographs for $Bi_4V_{2-x}Mg_xO_{11-\delta}$ ($0.0 \leq x \leq 0.20$) $Bi_4V_{2-x}Mg_xO_{11-\delta}$ (x = 0.0, 0.05, 0.10 and 0.15 and 0.20) (a) sintered x=0.0, (b) sintered x=0.05, (c) sintered x=0.10, (d) sintered x=0.15, (e) sintered x=0.20 and (f) quenched x = 0.15.

The sintered x = 0.15; Mg^{2+} doped sample shows the smallest grain size than other samples. The smaller grain size might inhibit the transformation of highly disordered γ- phase to ordered β- phase $Bi_4V_2O_{11-\delta}$ [5]. EDS analysis was also performed to know the semi quantitate atomic and wt. % of the elements of the sintered samples. The EDS analysis of different points on the sample surface shows nearly the same elemental distribution as have taken initially (Table 4.3).

Table 4.3 Comparison of initial and obtained stoichiometry of sintered $Bi_4V_2O_{11-\delta}$ from EDS analysis.

Element	Weight% (ideal case)	Weight% (EDS data) (± 2%)
O K	15.79	17.24
V K	9.14	7.26
Bi M	75.07	75.50
Composition	**$Bi_4V_2O_{11-\delta}$**	**$Bi_4V_{1.48}O_x$**

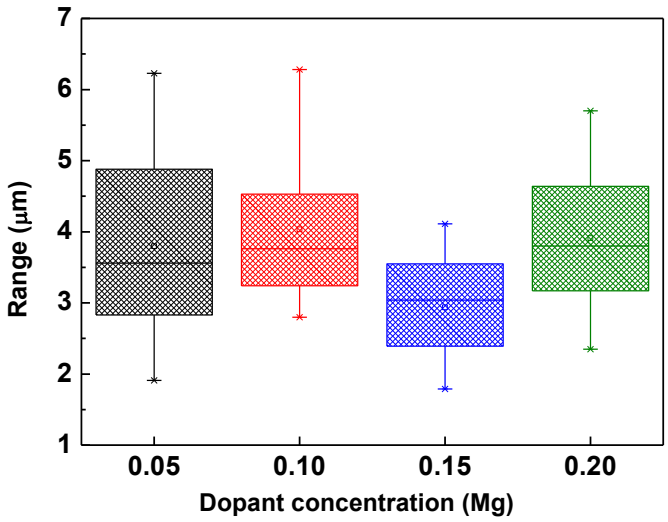

Figure 4.8 Grain size for sintered $Bi_4V_{2-x}ME_xO_{11-\delta}$ ($0.05 \leq x \leq 0.20$; ME = Mg^{2+}).

4.1.4 Dilatometry

Dilatometric analysis of the samples was carried out to check their linear expansion as well the phase transitions with respect to temperature. TECs calculated from the curves $\Delta L/L_o$ vs. temperature are shown in Figure 4.9 and 4.10 for quenched and sintered samples (x = 0.0 to 0.20) samples. The values of TECs in the temperature range of 200-700 °C are listed in Table 4.4. The higher values of TEC are observed for sintered samples as compared to quenched samples.

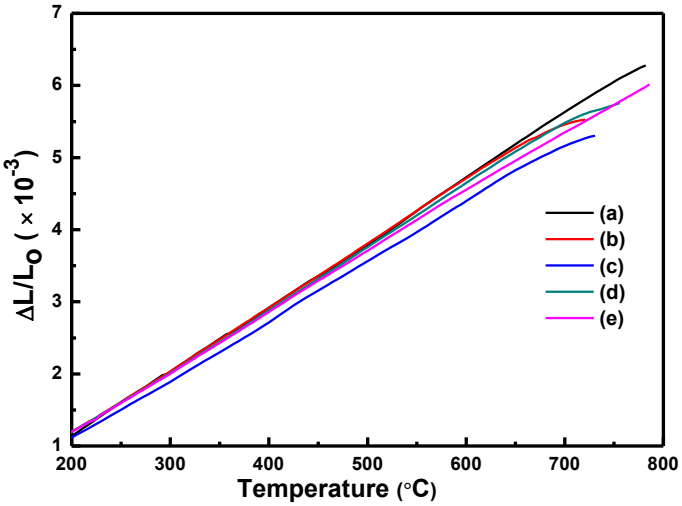

Figure 4.9 Dilatometric curves for quenched $Bi_4V_{2-x}ME_xO_{11-\delta}$ ($0.0 \leq x \leq 0.20$; ME = Mg^{2+}) (a) x=0.0, (b) x=0.05, (c) x=0.10, (d) x=0.15 and (e) x=0.20.

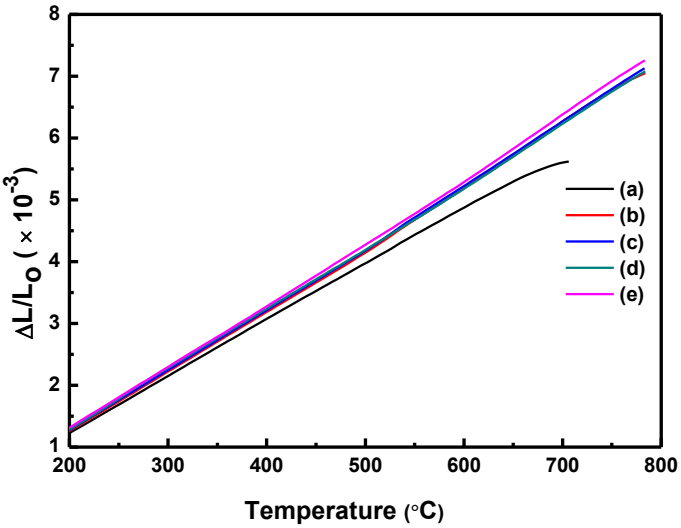

Figure 4.10 Dilatometric curves for sintered $Bi_4V_{2-x}ME_xO_{11-\delta}$ ($0.0 \leq x \leq 0.20$; ME = Mg^{2+}) (a) x=0.0, (b) x=0.05, (c) x=0.10, (d) x=0.15 and (e) x=0.20.

Usually, disordered samples show higher TEC than ordered samples (sintered samples). Since, random distribution of cations and anions leads to the asymmetric potential energy well of the disordered system. This anomaly might be related to the higher porosity with smaller grain size which leads to asymmetric potential energy well. Moreover, it is well reported in the literature that β- phase has higher TEC than γ- phase [33]. A typical representation of phase transition presented in Figure 4.11 for sample x = 0.10. The peak ~ 530 °C obtained in differential thermal expansion curve of x = 0.10 sample. It is related to β to γ- phase transition [34, 35].

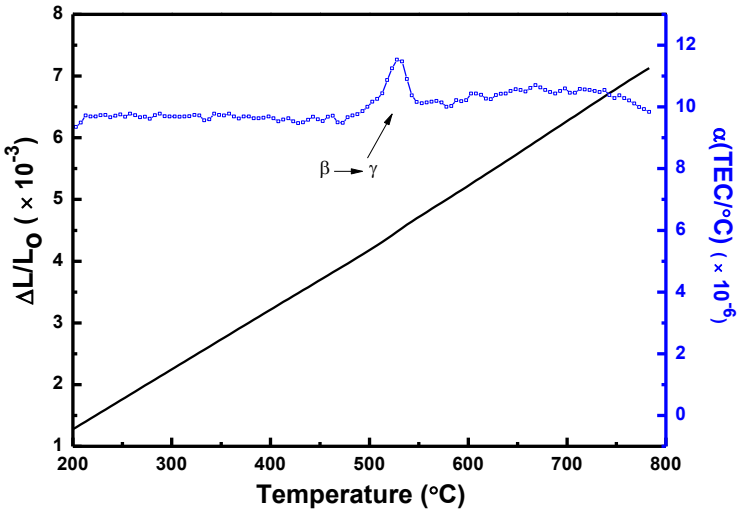

Figure 4.11 Dilatometric analysis for sintered $Bi_4V_{1.90}Mg_{0.10}O_{11-\delta}$.

The transition temperatures of all the samples were found to shift towards lower side with dopant concentration. The shifting of transition temperatures to lower side could be ascribed to the generation of asymmetry in the stoichiometry of $Bi_4V_2O_{11-\delta}$ with doping. As doping leads to the stabilization of γ- phase for a wider range of temperature. Thus, as a consequence the decrease in transition temperatures is observed [36]. Conclusively, the sintered samples have higher thermal expansion than quenched samples due to lower grain size than quenched samples (Figure 4.7).

Table 4.4 Thermal expansion coefficients for quenched and sintered $Bi_4V_{2-x}ME_xO_{11-\delta}$ ($0.0 \leq x \leq 0.20$; ME = Mg^{2+}).

Composition	As quenched samples TEC (/°C)	Sintered samples TEC (/°C)
$Bi_4V_2O_{11-\delta}$	8.8×10^{-6}	8.9×10^{-6}
$Bi_4V_{1.95}Mg_{0.05}O_{11-\delta}$	8.7×10^{-6}	9.5×10^{-6}
$Bi_4V_{1.90}Mg_{0.10}O_{11-\delta}$	8.2×10^{-6}	9.7×10^{-6}
$Bi_4V_{1.85}Mg_{0.15}O_{11-\delta}$	8.6×10^{-6}	9.5×10^{-6}
$Bi_4V_{1.80}Mg_{0.20}O_{11-\delta}$	8.4×10^{-6}	9.5×10^{-6}

4.1.5 Thermal analysis

Differential scanning calorimetry (DSC) and thermogravimetric (TG) analysis were carried out to study the various phase transitions and thermal stability of sintered samples. A typical DSC curve of the sintered sample with composition x = 0.0 exhibits two endothermic peaks corresponding to phase transformations α → β (~ 426 °C) and β → γ (~ 520 °C). On the other hand, the DSC curves (Figure 4.12 (a)) of the x = 0.05 and 0.15 sintered samples exhibit peaks, indicating the β → γ (~ 501 °C) and γ′ ↔ γ (~ 460 °C) transitions respectively.

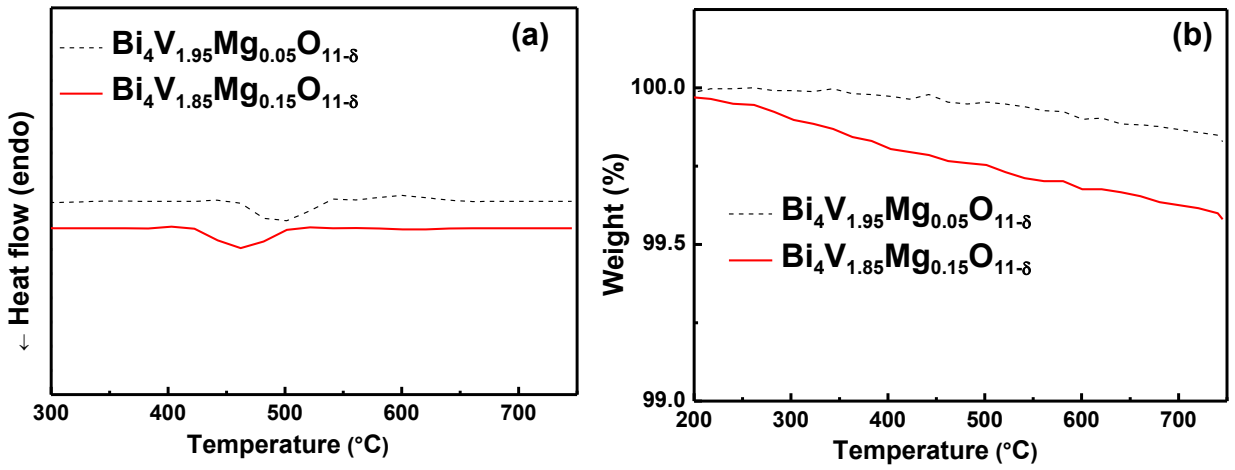

Figure 4.12 Thermal analysis for sintered $Bi_4V_{1.95}Mg_{0.05}O_{11-\delta}$ and $Bi_4V_{1.85}Mg_{0.15}O_{11-\delta}$ (a) DSC analysis and (b) TG analysis.

In general γ′ ↔ γ transformation takes place between 450 -500 °C [37]. The TG curve of the sintered x = 0.0 sample shows negligible weight loss. Similarly, doped sintered samples (Figure 4.12 (b)) show slight weight loss. This weight loss can be associated with reduction of vanadium during TGA measurement [38].

4.1.6 Electrical conductivity

The conductivity of the samples was measured by impedance analyser. The total resistance of the sample was estimated with the help of Nyquist plots, i.e. the graphs between real and imaginary parts of impedance [39]. Various kinds of Nyquist plots were fitted to various equivalent circuits as shown in Figure 4.13. For the lower values of temperature only one semicircle is obtained for all the samples. Therefore, the grain and grain boundary effect could not be distinguished.

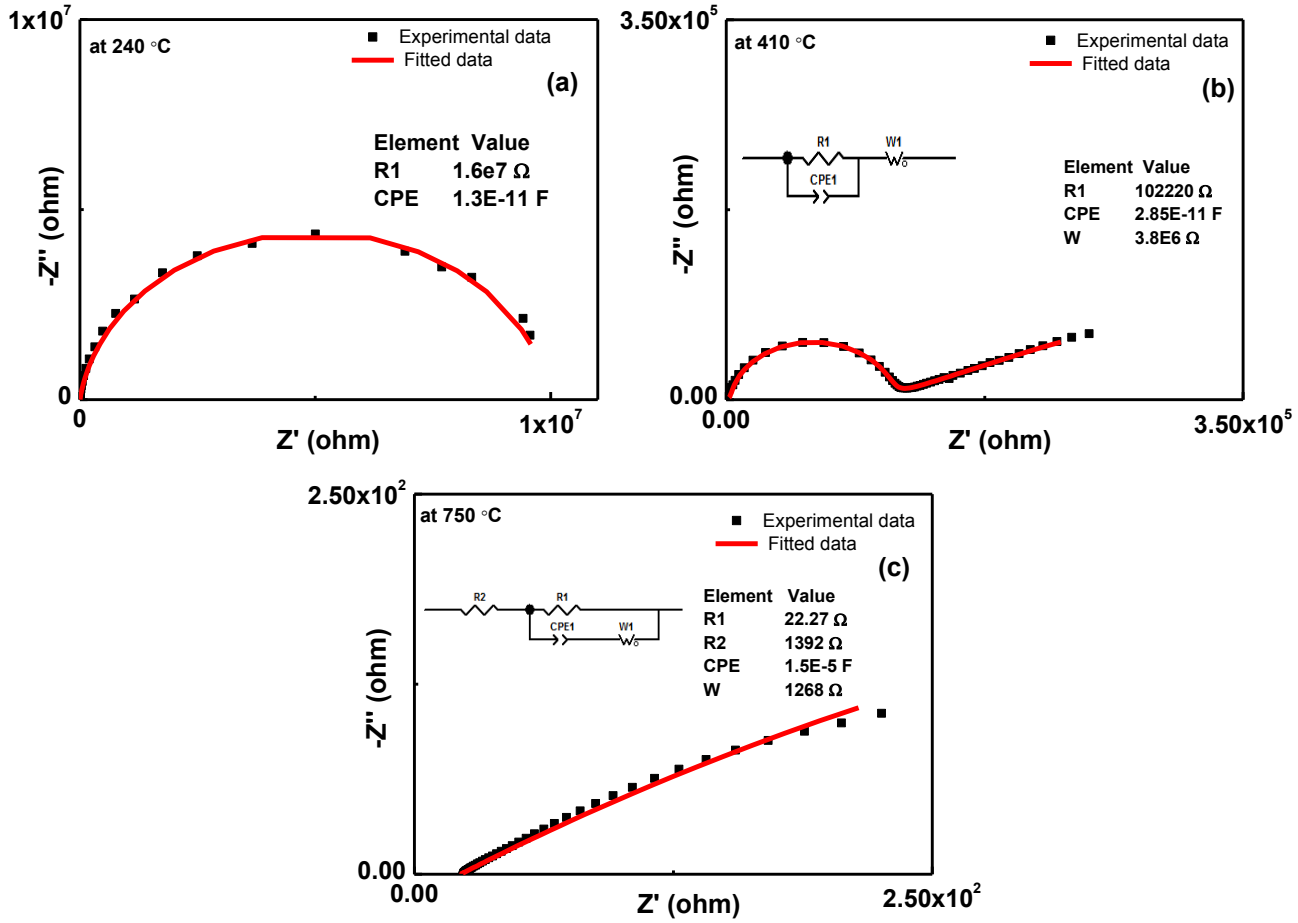

Figure 4.13 Nyquist plots and corresponding equivalent circuits for sintered $Bi_4V_{1.95}Mg_{0.05}O_{11-\delta}$ samples at different temperatures.

The value of resistance is obtained from the fitting of semicircle with R(CPE) circuit, having both the elements in parallel, where R stands for bulk resistance and CPE stands for constant phase element. At higher temperature, a straight line along with one semicircle is observed in Nyquist plot. The Warburg element in the circuit is introduced in series with the above defined R(CPE) circuit as shown in Figure 4.13 (b). The total resistance is the sum of grain and grain boundary resistance. At higher temperature (above ~600 °C), two semicircles merge to give a single arc; this kind of curve is fitted to the circuit as shown in Figure 4.13 (c). In this circuit R_1, resistance stands for grain and grain boundary resistance, Warburg element W and CPE_1 - for electrode processes [40]. The calculated conductivity at different temperature along with activation energies; E_a are listed in Table 4.5. Conductivity increases with increase in the amount of dopant due to the higher number of oxygen vacancies. However, at higher temperatures for $x > 0.10$ samples, the conductivity decreases. This phenomenon is associated with defect association and clustering with the increase in amount of doping. Also, the ordering in oxygen vacancies could have taken place with the increase in the number of oxygen vacancies with the doping amount [41]. The variation of conductivity with temperature was estimated from ln (σT) vs. 1000/T graphs [42, 43]. The increase in value of conductivity with increase in temperature can be related to the oxide ion movement. Actually, with the increase in temperature the thermal vibration energy of the oxide ion increases. This increases the movement of oxide ion movement and hence the conductivity of the samples [41]. Interestingly, the magnesium doped samples clearly show the three regions as marked in Figure 4.14. The Arrhenius plots can be divided into three regions, i.e. region I (lower temperature), region II (intermediate temperature) and region III (higher temperature). The higher conductivity values of magnesium doped samples can also be correlated with the ionic potential of the system [44]. Ionic potential is the ratio of ionic charge and size of the dopant cations.

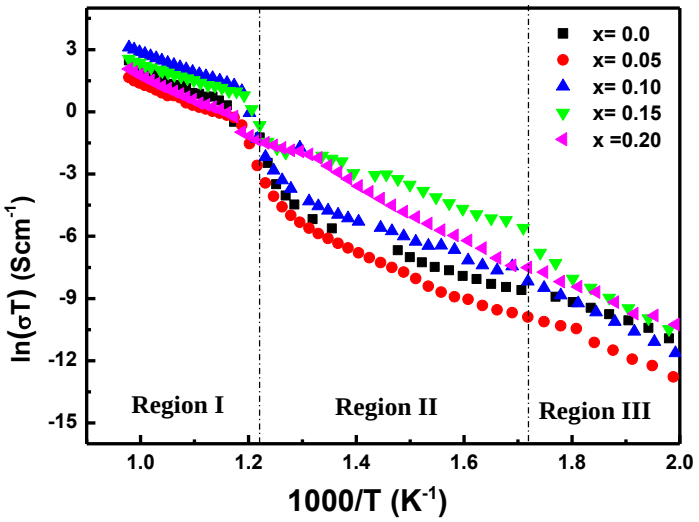

Figure 4.14 Arrhenius plots for sintered $Bi_4V_{2-x}ME_xO_{11-\delta}$ ($0.0 \leq x \leq 0.20$; ME = Mg^{2+}).

More is the ionic potential of the atom more will be its polarizability and hence conductivity. Magnesium samples possess value of ionic potential (2.78). In the present case, the lowering of value of conductivity with increase in amount of substitution can be suggested to be due to ionic potential of Mg^{2+}. As the amount of substitution Mg^{2+} increases, it could have created hindrance for the movement of oxide ions. Similarly, it has been reported by Sharma *et al.* [45] that ionic conductivity of Li^+ among various substituted cations such as Zn^{2+}, Al^{3+}, Ti^{4+} and Ge^{4+} in $Bi_4V_2O_{11-\delta}$ is lowest due to low ionic potential i.e. 1.32.

Table 4.5 Density, ionic conductivity and activation energy for sintered $Bi_4V_{2-x}ME_xO_{11-\delta}$ ($0.0 \leq x \leq 0.20$; ME = Mg^{2+}).

Composition	Density (g cm^{-3})	$\sigma_{700°C}$ (Scm^{-1}) ($\times 10^{-3}$)	E_a (eV) (200-300 °C)	E_a (eV) (300-480 °C)	E_a (eV) (570-750 °C)
$Bi_4V_2O_{11-\delta}$	7.42	5.84	0.75	0.77	1.14
$Bi_4V_{1.95}Mg_{0.05}O_{11-\delta}$	7.24	2.93	0.98	0.92	0.82
$Bi_4V_{1.90}Mg_{0.10}O_{11-\delta}$	7.21	13.7	1.04	0.97	0.82
$Bi_4V_{1.85}Mg_{0.15}O_{11-\delta}$	7.03	7.86	1.17	0.82	0.74
$Bi_4V_{1.80}Mg_{0.20}O_{11-\delta}$	7.51	4.00	0.80	1.18	1.05

4.1.7 UV/ Vis analysis

The optical band gaps of materials give idea about their nature like narrow optical band gap semiconductor, wide optical band gap semiconductor or insulator. In addition to this, the Urbach energy, can also give idea about the variation in defects. The values of optical band gap of quenched and sintered samples are calculated from the absorption edge for the transmission spectra (Figures 4.15 and 4.16). The value of optical band gap of $Bi_4V_2O_{11-\delta}$ is ~2 eV [48]. Whereas for doped $Bi_4V_2O_{11-\delta}$ is ~ 2.13, 1.94 and 1.99 eV for Ga^{3+}, As^{5+} and Mn^{2+}, respectively [30, 48].

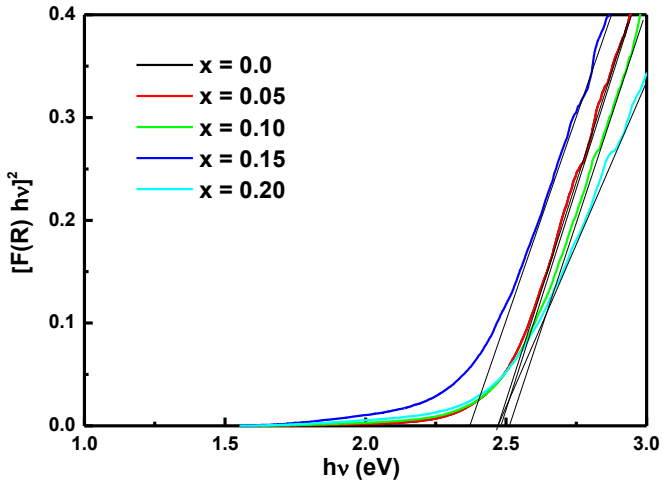

Figure 4.15 Graphical representation of the E_g values for quenched $Bi_4V_{2-x}ME_xO_{11-\delta}$ ($0.0 \leq x \leq 0.20$; ME = Mg^{2+}).

s

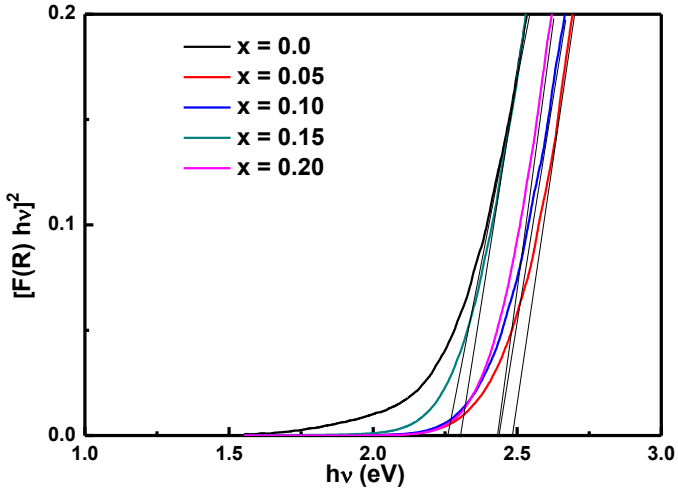

Figure 4.16 Graphical representation of the E_g values for sintered $Bi_4V_{2-x}ME_xO_{11-\delta}$ ($0.0 \leq x \leq 0.20$; ME = Mg^{2+}).

The optical band gap values of the present samples are in good agreement with the earlier reported values [47, 48]. The difference in the values of optical band gap arises due to the change in the structure of the system as a result of change in the amount of dopant [29, 30]. Lower optical band gaps are observed in the sintered samples than quenched samples which may be attributed to lower grain size and higher porosity in sintered samples (Table 4.6). The Urbach energy of the sintered samples is found to be on the lower side as compared to the quenched samples. However, the sintered samples show higher disorder than quenched samples. During sintering, the V^{4+} oxidized to V^{5+} and reduced the overall oxygen vacancies in the sintered system. It might be related to two different competitive mechanisms taking place in the sintered samples firstly, decrease in oxygen vacancies due to oxidation of V^{4+} to V^{5+} and secondly, the lower grain size with higher volume of grain boundaries lead to increase surface defects.

Table 4.6 Values of optical band gap and Urbach energy for quenched and sintered $Bi_4V_{2-x}ME_xO_{11-\delta}$ ($0.0 \leq x \leq 0.20$; $ME = Mg^{2+}$).

Composition	Quenched samples		Sintered samples	
	E_g (eV)	ΔE (eV)	E_g (eV)	ΔE (eV)
$Bi_4V_2O_{11-\delta}$	2.45	0.41	2.27	0.56
$Bi_4V_{1.95}Mg_{0.05}O_{11-\delta}$	2.45	0.49	2.45	0.23
$Bi_4V_{1.90}Mg_{0.10}O_{11-\delta}$	2.48	0.49	2.44	0.23
$Bi_4V_{1.85}Mg_{0.15}O_{11-\delta}$	2.34	0.59	2.30	0.26
$Bi_4V_{1.80}Mg_{0.20}O_{11-\delta}$	2.48	0.61	2.43	0.20

4.2 $Bi_4V_{2-x}ME_xO_{11-\delta}$ ($0.0 \leq x \leq 0.20$; ME = Ca^{2+})

Ca^{2+} doped samples are synthesized to investigate the effect of melt quench followed by sintering technique on γ- phase stabilization, phase transitions and total conductivity. It is expected that the melt quench technique will not only increase the solid solubility limit of dopant but also easily stabilize the γ- phase at room temperature.

4.2.1 X-ray diffraction analysis

The XRD patterns of $Bi_4V_{2-x}ME_xO_{11-\delta}$ ($0.0 \leq x \leq 0.20$; ME = Ca^{2+}) for all quenched samples indicate γ- phase stabilization except x = 0.0 sample. The Rietveld refined XRD patterns for quenched samples are shown in Figure 4.17.

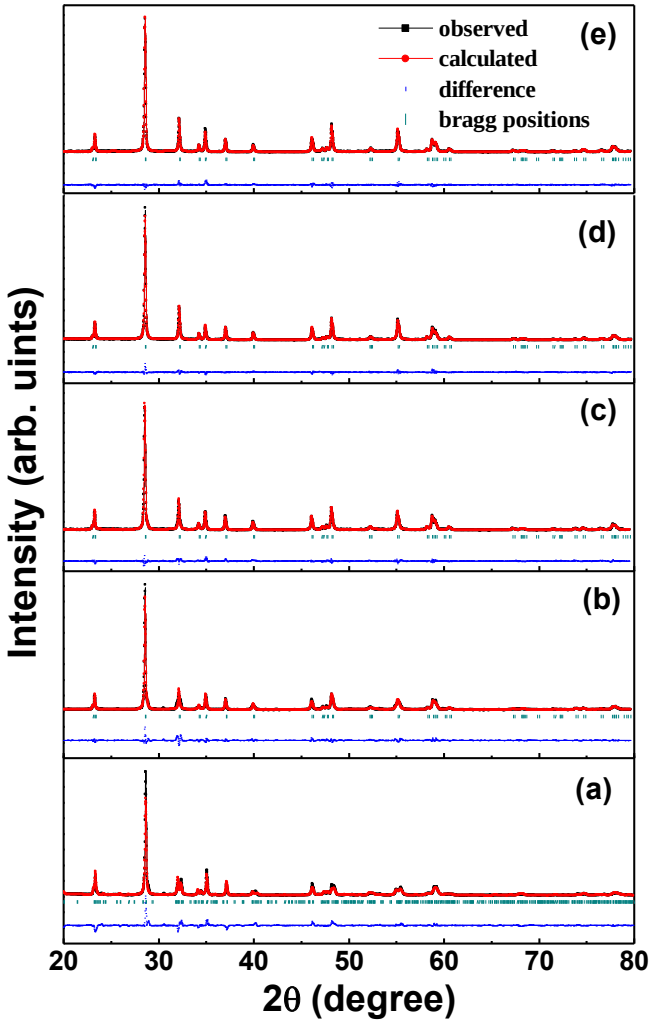

Figure 4.17 XRD patterns of quenched $Bi_4V_{2-x}ME_xO_{11-\delta}$ ($0.0 \leq x \leq 0.20$; ME = Ca^{2+}) (a) x = 0.0, (b) x = 0.05, (c) x = 0.10, (d) x = 0.15 and (e) x = 0.20.

The XRD data of all the samples was refined with *I4/mmm* space group of γ- phase [1]. The refinement parameters R_{exp} and χ are also listed in Table 4.7. Ca^{2+} doped $Bi_4V_2O_{11-\delta}$ shows β→γ phase transformation for x > 0.10 samples in case of sintered samples (Figure 4.18). The stabilization of γ- phase is observed to take place at lower dopant concentration than earlier reported dopant concentration for the similar composition [49]. The increase in 'c' parameter is observed with the increase in amount of doping. This increase in 'c' parameter could be due to the greater ionic radii of the dopant atom than host atom [50, 51]. The increase in 'c' parameter with increase in amount of dopant is also observed with the doping of Ca^{2+}, Ti^{4+}, Cr^{3+}, and Fe^{3+} in $Bi_4V_2O_{11-\delta}$ [49, 51, 52]. XRD peaks, in case of Ca^{2+} doped samples, shift towards lower 2θ values as compared to Mg^{2+} doped samples which can be suggested due to the greater ionic radii of Ca^{2+} (1.0 Å) than Mg^{2+} (0.72 Å) [21].

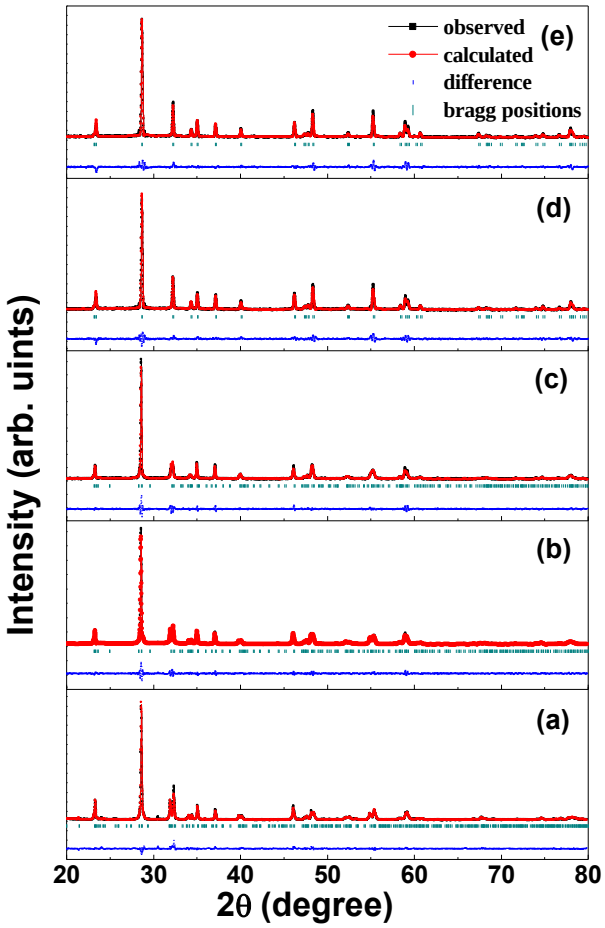

Figure 4.18 XRD patterns of sintered $Bi_4V_{2-x}ME_xO_{11-\delta}$ ($0.0 \leq x \leq 0.20$; ME = Ca^{2+}) (a) x = 0.0, (b) x = 0.05, (c) x = 0.10, (d) x = 0.15 and (e) x = 0.20.

Table 4.7 Rietveld refined parameters for quenched and sintered $Bi_4V_{2-x}ME_xO_{11-\delta}$ ($0.0 \leq x \leq 0.20$; ME = Ca^{2+}).

Quenched Samples					Goodness parameters of fitting		Sintered samples				Goodness parameters of fitting	
Composition	**a (Å)**	**b (Å)**	**c (Å)**	**Volume ($Å^3$)**	**R_{exp}**	**χ^2**	**a (Å)**	**b (Å)**	**c (Å)**	**Volume ($Å^3$)**	**R_{exp}**	**χ^2**
$Bi_4V_2O_{11-\delta}$	5.587	15.350	16.596	1423.445	6.94	2.67	5.599	15.338	16.599	1425.664	8.46	2.18
$Bi_4V_{1.95}Ca_{0.05}O_{11-\delta}$	3.933	3.933	15.385	238.092	7.67	3.03	11.079	5.5946	15.361	952.142	6.59	3.24
$Bi_4V_{1.90}Ca_{0.10}O_{11-\delta}$	3.936	3.936	15.408	238.659	7.78	1.59	11.094	5.578	15.366	950.846	6.43	3.57
$Bi_4V_{1.85}Ca_{0.15}O_{11-\delta}$	3.932	3.932	15.405	238.215	8.20	1.14	3.928	3.928	15.258	236.919	6.63	3.40
$Bi_4V_{1.80}Ca_{0.20}O_{11-\delta}$	3.933	3.933	15.412	238.435	7.61	1.33	3.927	3.927	15.370	237.087	6.59	3.66

The XRD peaks become broader with dopant concentration. As discussed in section 4.1.1. position change along with the broadness of X-ray diffraction peaks can be used to estimate the lattice strain generated in the system with the incorporation of dopant atoms. Thus, the strain induced in the lattice can be calculated with the help of Williamson Hall analysis [18]. Using, Williamson Hall method both crystallite size and strain induced in the lattice can also be calculated using equation 4.1. The strain for all the samples was calculated from the linear fit of $\beta\cos\theta$ vs. $4\sin\theta$ curves [19, 20]. The values of strain were observed to be positive depicting the tensile strain generated in the systems. The tensile strain observed in the samples can be suggested, due to the greater ionic radii of dopant atom than that of host atom in the present systems [21].

4.2.2 Analysis of FTIR spectra

FTIR spectra for quenched and sintered $Bi_4V_{2-x}ME_xO_{11-\delta}$ ($0.0 \leq x \leq 0.20$; ME = Ca^{2+}) samples were obtained. All the bands obtained are similar to that of bands in Mg^{2+} doped system. The different bands obtained in the spectra can be assigned to the vibrations of different bonds. The FTIR spectra of bismuth vanadate system exhibits absorption bands, namely at ~ 468 cm^{-1}, ~ 519 cm^{-1}, ~ 624 cm^{-1}, ~ 732 cm^{-1}, ~ 767 cm^{-1} and ~ 801 cm^{-1}. Out of which, bands appearing in the spectra at ~ 468 cm^{-1} and ~ 519 cm^{-1} are attributed to the symmetric bending vibration of Bi-O bonds in BiO_3 pyramidal units. Whereas, the band due to the vibration of symmetric modes of V- O-V bonds can be due to the band at ~ 732 cm^{-1}. The vibrations due to V- O-V chains could have generated the absorption band at ~ 801 cm^{-1} [22- 25]. With the increase in amount of dopant and sintering the structural changes in the system taking place in the system are visible in FTIR spectra. With the increase in amount of dopant the bands shift towards higher wavenumber side. This shifting of bands towards higher side can be attributed to the difference between the mass and size of the host and dopant [25-27]. As the amount of dopant increases the broadening in bands is observed. The

broadening of bands can be explained on the basis of addition of number of vibrational bands arising due to the variation in the bond lengths and angles. For both quenched as well as sintered samples, the bands at ~ 615 and ~ 912 cm^{-1} start disappearing as the doping amount is increased. It is a clear indication of the incorporation of Ca^{2+} in VO_4 polyhedrons [28].

4.2.3 Microstructural analysis

SEM micrographs of all the sintered samples indicate that grains are well grown and non-uniform in size (Figure 4.19). The range and average grain size for $Bi_4V_{2-x}ME_xO_{11-\delta}$ ($0.0 \leq x \leq 0.20$; ME = Ca^{2+}) sintered samples is shown in Figure 4.20. Higher deviation of grain size from its mean value indicates that the grain size for all the samples is spread out over a large number of values [30]. The non- uniformity in the grain size can be attributed to the grain growth kinetics during sintering due to boundary to boundary movement. Since, the grain boundary energy depends on the grain boundary orientation and mobility [31, 32]. Decrease in grain size is observed with the increase in amount of Ca^{2+} dopant. Thus, it can be suggested that Ca^{2+} is acting as grain growth inhibitor [53]. In addition to this, higher concentration of dopant particularly Ca^{2+} leads to increase the liquid phase sintering as can be observed in Figure 4.19. In comparison to Mg^{2+} doped system, the liquid phase sintering is lesser in Ca^{2+} doped systems. Since, grain boundaries are more distinguishable in Ca^{2+} doped system than Mg^{2+} doped systems. Ca^{2+} doped samples have larger grain size than that of Mg^{2+} doped samples. This larger grain size of Ca^{2+} doped samples can be related to the lower melting point of calcium doped $Bi_4V_2O_{11-\delta}$. The increased grain size trend can also be correlated with the higher values of full width at half maxima (FWHM) values for Mg^{2+} doped samples than Ca^{2+} doped samples [26]. The Energy dispersive spectroscopy (EDS) analysis was also performed to know the semi quantitative atomic and wt. % of the elements of the sintered samples. The EDS analysis of different points on the sample surface represents shows that elemental distribution is nearly same as had taken initially.

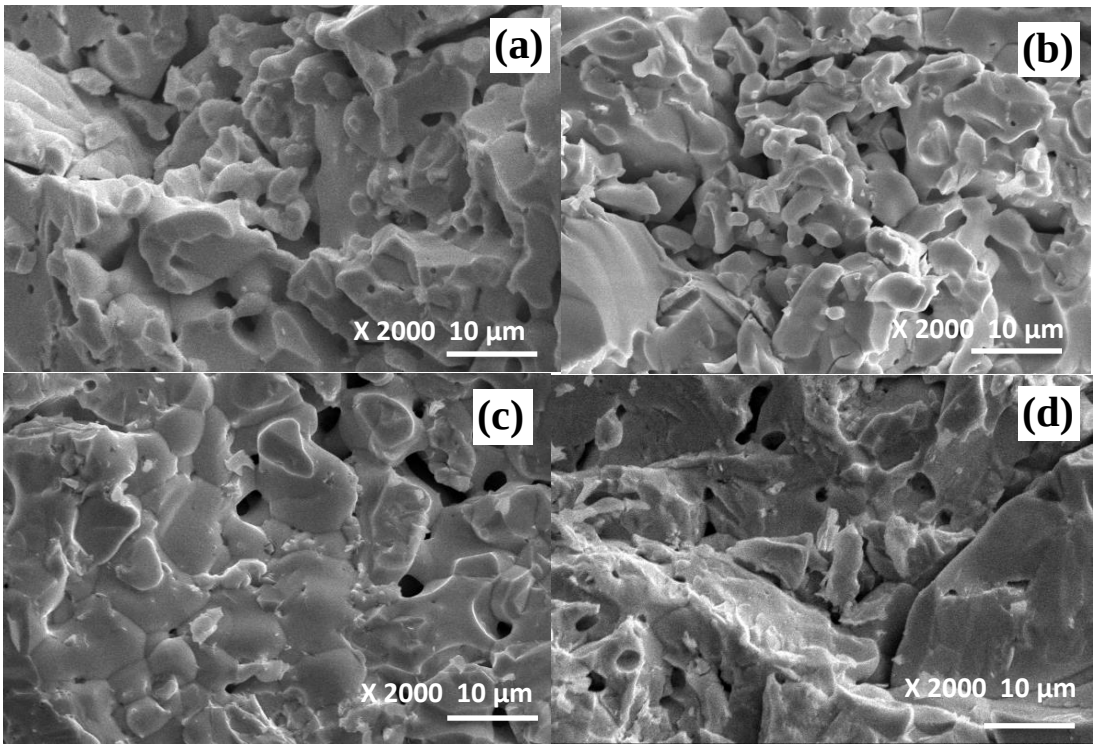

Figure 4.19 Scanning electron micrographs for sintered $Bi_4V_{2-x}ME_xO_{11-\delta}$ ($0.05 \leq x \leq 0.20$; ME = Ca^{2+}) (a) x=0.05, (b) x=0.10, (c) x=0.15 and (d) x=0.20.

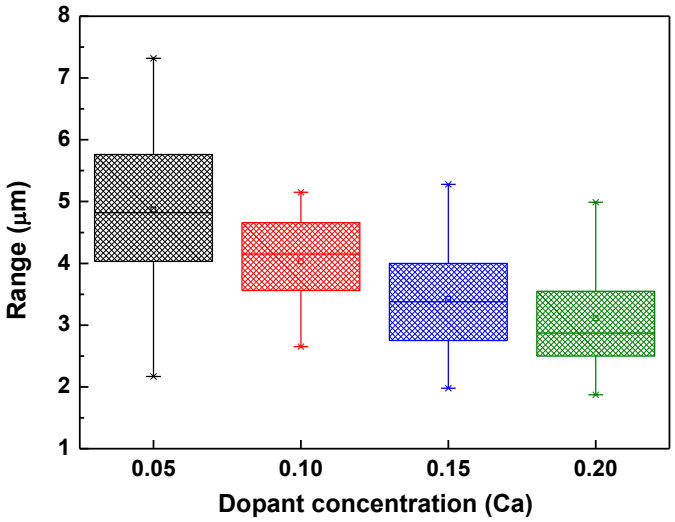

Figure 4.20 Grain size for sintered $Bi_4V_{2-x}ME_xO_{11-\delta}$ ($0.05 \leq x \leq 0.20$; ME = Ca^{2+}).

4.2.4 Dilatometry

Dilatometric analysis of $Bi_4V_{2-x}ME_xO_{11-\delta}$ ($0.0 \leq x \leq 0.20$; ME = Ca^{2+}) quenched samples was carried out to check their linear expansion with respect to temperature. TECs calculated from the $\Delta L/L_o$ vs. temperature curves for quenched $Bi_4V_{2-x}ME_xO_{11-\delta}$ ($0.0 \leq x \leq 0.20$; ME = Ca^{2+})

samples. The values of TECs in the temperature range 200-700 °C are listed in Table 4.8. The maximum value of TEC is observed for x= 0.15 sample. It can be related to the fact that, disordered samples show higher TEC than ordered samples. x = 0.15 sample shows γ- phase stabilization before and after sintering. Actually, random distribution of cations and anions leads to the non- uniform potential energy well of the system. In addition to this, no particular trend is followed in TEC values with the increase in amount of dopant. Higher values of TEC, are observed for Ca^{2+} doped samples as compared to Mg^{2+} doped samples. Thus, it can be suggested that Ca^{2+} doped samples have higher asymmetric potential well than Mg^{2+} doped samples.

Table 4.8 Thermal expansion coefficients for quenched $Bi_4V_{2-x}ME_xO_{11-\delta}$ ($0.0 \leq x \leq 0.20$; ME = Ca^{2+}).

Composition	As quenched samples TEC (/°C)
$Bi_4V_2O11-\delta$	8.8×10^{-6}
$Bi_4V_{1.95}Ca_{0.05}O_{11-\delta}$	10.4×10^{-6}
$Bi_4V_{1.90}Ca_{0.10}O_{11-\delta}$	9.9×10^{-6}
$Bi_4V_{1.85}Ca_{0.15}O_{11-\delta}$	10.6×10^{-6}
$Bi_4V_{1.80}Ca_{0.20}O_{11-\delta}$	10.2×10^{-6}

4.2.5 Thermal analysis

For Ca doped $Bi_4V_{2-x}ME_xO_{11-\delta}$ ($0.0 \leq x \leq 0.20$); sintered samples in order to study the various phase transitions and thermal stability, differential scanning calorimetry (DSC) and thermogravimetric (TG) analysis were carried out. DSC curve for $Bi_4V_{1.95}Ca_{0.05}O_{11-\delta}$ (Figure 4.25 (a)) sample indicates the transition $\beta \rightarrow \gamma$ at 560 °C. The slight increase in transition

temperature can be related to the generation of asymmetry in the stoichiometry of $Bi_4V_2O_{11-\delta}$ with doping. Whereas, $Bi_4V_{1.85}Ca_{0.15}O_{11-\delta}$, sample does not show any transition (Figure 4.21 (a)). Thus, it can be concluded that calcium doping inhibits the $\gamma \rightarrow \gamma'$ transition. This observation can be attributed to the processing parameter and ordering of oxygen vacancies in the system. Recently, Piva *et al.* [37] reported the inhibition of $\gamma \rightarrow \gamma'$ transition in γ-$Bi_2V_{0.9}Cu_{0.1}O_{5.35}$ composite with 13 and 26 wt. % yttria-stabilized zirconia. From TGA analysis the weight loss as can be observed from Figure 4.21 (b) is observed for both the samples but in case of $Bi_4V_{1.95}Ca_{0.05}O_{11-\delta}$ sample the weight loss is in two steps.

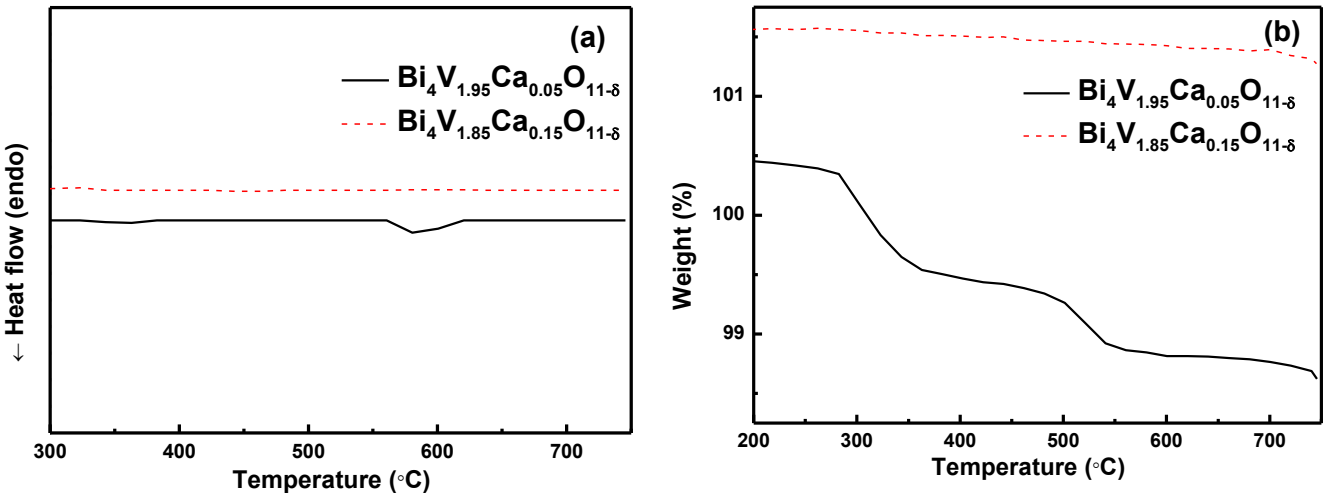

Figure 4.21 Thermal analysis for sintered $Bi_4V_{1.95}Ca_{0.05}O_{11-\delta}$ and $Bi_4V_{1.85}Ca_{0.15}O_{11-\delta}$ (a) DSC analysis and (b) TG analysis.

First weight loss is upto ~ 270 °C can be attributed to the loss of moisture. Above this temperature, the sample shows constant weight loss with a broad step at ~550 °C may be the related to the $\beta \rightarrow \gamma$ transition as observed in DSC curves of these systems. The discrepancy in the transition temperatures obtained from DSC and TG analysis is attributable to the sluggish nature of the transition. However in $Bi_4V_{1.85}Ca_{0.15}O_{11-\delta}$ constant weight loss due to reduction of vanadium is observed [38].

4.2.6 Electrical conductivity

The conductivity of the samples was measured with the help of impedance analyser. The total resistance of the sample was calculated from the graphs between real and imaginary parts of impedance i.e. Nyquist plots [39]. It has already been discussed earlier in section 4.1.6 that different kinds of Nyquist plots were fitted to different circuits to obtain the value of resistance.

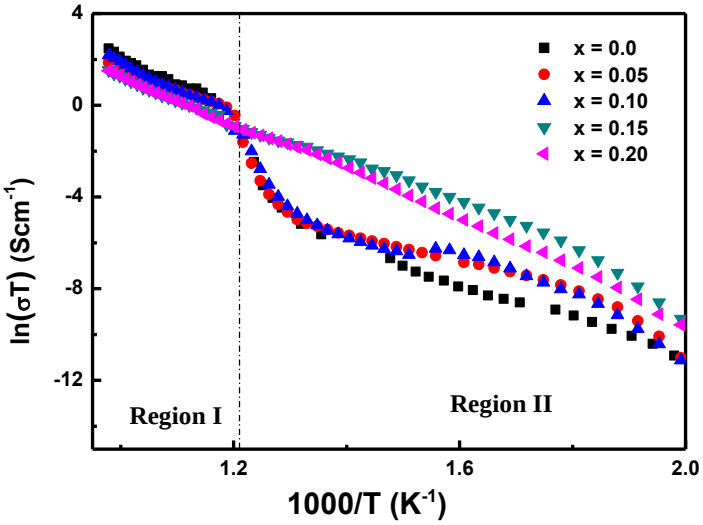

Figure 4.22 Arrhenius plots for sintered $Bi_4V_{2-x}ME_xO_{11-\delta}$ ($0.0 \leq x \leq 0.20$; ME = Ca^{2+}).

The values of conductivity at particular temperature along with activation energies; E_a are listed in Table 4.9. With increase in the amount of dopant, conductivity of samples increases. This observation can be related to the higher number of oxygen vacancies. However, for x > 0.10 sample the conductivity is observed to get decrease at higher temperature. This phenomenon might be associated with defect association and clustering taking place in the system with the increase in amount of doping. Also, the ordering in oxygen vacancies could have taken place with the increase in the number of oxygen vacancies with the doping amount [41]. The variation of conductivity with temperature was estimated from ln (σT) vs. 1000/T graphs (Figure 4.22) [42, 43]. The increase in value of conductivity with increase in temperature is related to the oxide ion movement. The thermal vibration energy of the oxide ion increases with the increase in temperature. This increases the movement of oxide ion and

hence the conductivity of the samples [41]. For Ca^{2+} doped samples with x = 0.15 and 0.20, γ ↔ γ′ transition is not observed in conductivity. This observation is in accordance with the observation of differential scanning calorimetry (DSC) (Figure 4.21 (a)). Thus, it can be said that calcium doping has inhibited the γ ↔ γ′ transition which is commonly reported in these systems. The suppression of highly disordered γ- phase to partially ordered γ′ - phase. It might be related to the liquid phase sintering that prevents oxygen ordering or clustering as compared to other samples. It has also been reported that, γ ↔ γ′ transition can be suppressed if the grain size of the samples is small enough [46, 54]. Magnesium doped samples possess higher values of conductivity than calcium doped samples at higher temperatures.

Table 4.9 Density, ionic conductivity and activation energy for sintered $Bi_4V_{2-x}ME_xO_{11-\delta}$ ($0.0 \leq x \leq 0.20$; ME = Ca^{2+}).

Composition	Density (g cm^{-3})	$\sigma_{500°C}$ (Scm^{-1}) ($\times10^{-4}$)	E_a (eV) (200 - 560 °C)	E_a (eV) (560 - 750 °C)
$Bi_4V_2O_{11-\delta}$	7.42	0.10	0.83	1.13
$Bi_4V_{1.95}Ca_{0.05}O_{11-\delta}$	7.36	0.12	0.82	0.75
$Bi_4V_{1.90}Ca_{0.10}O_{11-\delta}$	7.34	0.16	0.87	0.93
$Bi_4V_{1.85}Ca_{0.15}O_{11-\delta}$	7.28	2.55	0.83	0.83
$Bi_4V_{1.80}Ca_{0.20}O_{11-\delta}$	7.38	2.36	0.92	0.92

These higher conductivity values of magnesium doped samples can also be correlated with the ionic potential of the system. Magnesium samples possess higher value of ionic potential (2.78) than calcium doped (2.0) samples. Thus, higher values of conductivity in magnesium doped samples can also be attributed to higher ionic potential of magnesium doped samples.

4.2.7 UV/ Vis analysis

The reflectance spectra of quenched and sintered samples are shown in Figures 4.23 and 4.24. The reflectance of the samples is increasing with the increase in amount of dopant. The values of optical band gap of quenched and sintered samples are calculated from the absorption edge for the transmission spectra. The optical band gap values of all the quenched and sintered samples, along with Urbach energy are listed in Table 4.10. Urbach energy is the measure of disorderdness of the system, more is the Urbach energy more is the disorderdness of the material. From the UV/ vis analysis of the $Bi_4V_{2-x}ME_xO_{11-\delta}$ ($0.0 \leq x \leq 0.20$; ME = Ca^{2+}) quenched and sintered samples, it is observed that sintered samples represent lower optical band gap values than quenched samples. This observation can be attributed to lower grain size and higher porosity in sintered samples.

Table 4.10 Values of optical band gap and Urbach energy for quenched and sintered $Bi_4V_{2-x}ME_xO_{11-\delta}$ ($0.0 \leq x \leq 0.20$; ME = Ca^{2+}).

Composition	Quenched samples		Sintered samples	
	E_g (eV)	ΔE (eV)	E_g (eV)	ΔE (eV)
$Bi_4V_2O_{11-\delta}$	2.45	0.41	2.27	0.56
$Bi_4V_{1.95}Ca_{0.05}O_{11-\delta}$	2.42	0.16	2.14	0.18
$Bi_4V_{1.90}Ca_{0.10}O_{11-\delta}$	2.44	0.15	2.00	0.20
$Bi_4V_{1.85}Ca_{0.15}O_{11-\delta}$	2.44	0.17	2.08	0.18
$Bi_4V_{1.80}Ca_{0.20}O_{11-\delta}$	2.36	0.22	2.19	0.17

The values of Urbach energy as well as optical band gap do not follow any trend. However, the maximum value of Urbach energy among sintered doped samples ~ 0.20 eV along with minimum optical band gap ~ 2.00 eV is obtained for $Bi_4V_{1.90}Ca_{0.10}O_{11-\delta}$. The results of UV/ vis spectroscopy are also supported by the impedance spectroscopy results. Since, the maximum value of total conductivity is observed for $Bi_4V_{1.90}Ca_{0.10}O_{11-\delta}$, sintered sample. As

there is an inverse trend of the optical band gap with conductivity i.e. the value of conductivity increases with decrease in optical band gap [30].

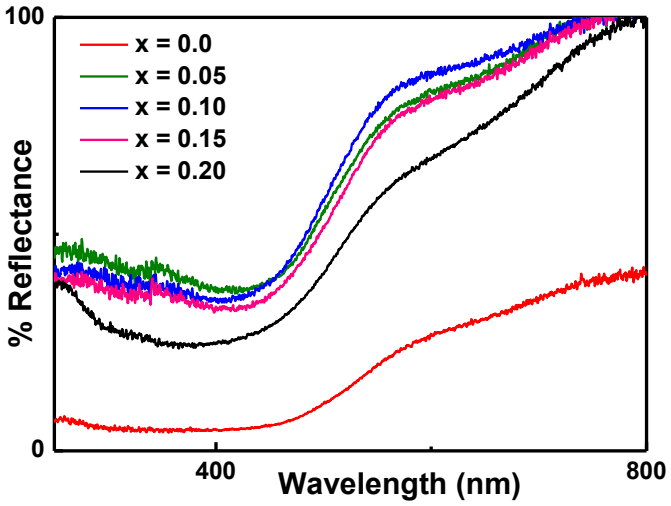

Figure 4.23 Reflectance spectra of quenched $Bi_4V_{2-x}ME_xO_{11-\delta}$ ($0.0 \leq x \leq 0.20$; ME = Ca^{2+}).

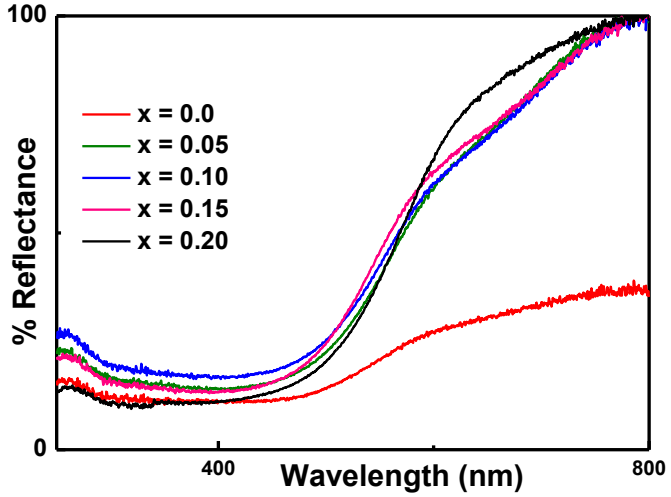

Figure 4.24 Reflectance spectra of sintered $Bi_4V_{2-x}ME_xO_{11-\delta}$ ($0.0 \leq x \leq 0.20$; ME = Ca^{2+}).

4.3 $Bi_4V_{2-x}ME_xO_{11-\delta}$ ($0.0 \leq x \leq 0.20$; ME = Sr^{2+})

$Bi_4V_{2-x}Sr_xO_{11-\delta}$ ($0.0 \leq x \leq 0.20$) composition is synthesized by melt quench route followed by sintering. The obtained samples are characterized by various techniques. The results are discussed in light of the variation of dopants, crystalline phase, structure and number of oxygen vacancies with the increase in amount of dopant.

4.3.1. X-ray diffraction analysis

The analysis of diffraction pattern of sample $Bi_4V_{2-x}Sr_xO_{11}$ (x = 0.0) represents a superstructure peak at ~ 24.4˚. The presence of this XRD peak signifies α- phase. The confirmation of phase was done with the help of rietveld refinement using FULPROF software with space group *C2/m* [8]. The phase stabilized in x = 0.0 sample remained intact even after sintering and could not show any appreciable change except some peaks broadening. The XRD patterns of quenched $Bi_4V_{2-x}Sr_xO_{11-\delta}$ ($0.05 \leq x \leq 0.20$) samples indicate the γ- phase stabilization at room temperature. The obtained XRD results clearly show the effect of processing parameters on γ- phase stabilization. Since, the superlattice peaks at ~ 24° are absent. The XRD peak at ~ 32° as shown in Figure 4.25 and 4.26 is singlet in all the samples. In the present case the solid solubility limit of Sr^{2+} is wider than the earlier report on similar system [55]. The obtained XRD patterns were fitted with space group *I4/mmm* having tetragonal structure. All the patterns were well fitted with $R_{exp} \leq 10\%$. After sintering, it is observed that, the γ- phase gets converted to β- phase in x = 0.05 sample. It has orthorhombic structure and refined with space group *Amam* [1, 2, 45, 51, 55-57]. Whereas, $0.10 \leq x \leq 0.20$ sintered samples could not show any transformation γ- phase to α or β phase. After sintering, the XRD peaks become sharper as compared to the quenched samples. As the doping concentration increases, the lattice parameters a, b and c also increase. The Rietveld refined lattice parameters are listed in Table 4.11. It is associated with the Sr^{2+} substitution for V^{5+}. Since, the ionic radius of Sr^{2+} (1.18 Å) is larger than V^{5+} (0.54 Å). Actually,

aliovalent doping gives rise to two kinds of effects; firstly it increases the tetrahedral/octahedral ratio by reducing the V^{5+} to V^{4+} which results into the reduction of unit cell volume [58, 59]. Secondly, the substitution of host cation with larger ionic radii than guest cation increases the unit cell volume. In the present study, the size difference between host V^{5+} (0.54 Å) and guest Sr^{2+} (1.32 Å) is more effective than reduction of V^{5+} to V^{4+} because the unit cell volume increases with substitution concentration.

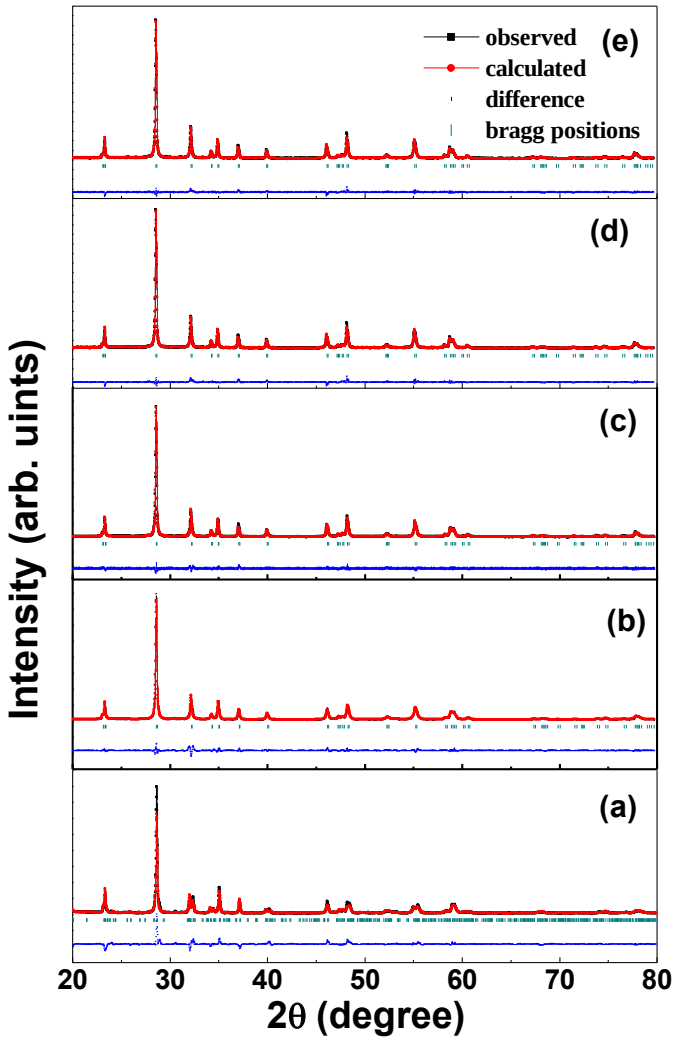

Figure 4.25 XRD patterns of quenched $Bi_4V_{2-x}ME_xO_{11-\delta}$ ($0.0 \leq x \leq 0.20$; ME = Sr^{2+}) (a) x = 0.0, (b) x = 0.05, (c) x = 0.10, (d) x = 0.15 and (e) x = 0.20.

Table 4.11 Rietveld refined parameters for quenched and sintered $Bi_4V_{2-x}ME_xO_{11-\delta}$ ($0.0 \leq x \leq 0.20$; ME = Sr^{2+}).

Quenched samples					Goodness parameters of fitting		Sintered samples				Goodness parameters of fitting	
Composition	**a (Å)**	**b (Å)**	**c (Å)**	**Volume ($Å^3$)**	**R_{exp}**	**χ^2**	**a (Å)**	**b (Å)**	**c (Å)**	**Volume ($Å^3$)**	**R_{exp}**	**χ^2**
$Bi_4V_2O_{11-\delta}$	5.587	15.350	16.596	1423.445	6.94	2.67	5.599	15.338	16.599	1425.664	8.46	2.18
$Bi_4V_{1.95}Sr_{0.05}O_{11-\delta}$	3.931	3.931	15.384	237.719	7.23	2.33	11.060	5.589	15.342	948.392	7.44	1.44
$Bi_4V_{1.90}Sr_{0.10}O_{11-\delta}$	3.933	3.933	15.402	238.251	6.83	1.52	3.933	3.933	15.373	237.813	7.14	2.93
$Bi_4V_{1.85}Sr_{0.15}O_{11-\delta}$	3.936	3.936	15.416	238.882	7.25	2.31	3.935	3.935	15.393	238.392	7.01	2.41
$Bi_4V_{1.80}Sr_{0.20}O_{11-\delta}$	3.941	3.941	15.436	239.690	7.18	1.34	3.938	3.938	15.411	238.987	7.29	2.45

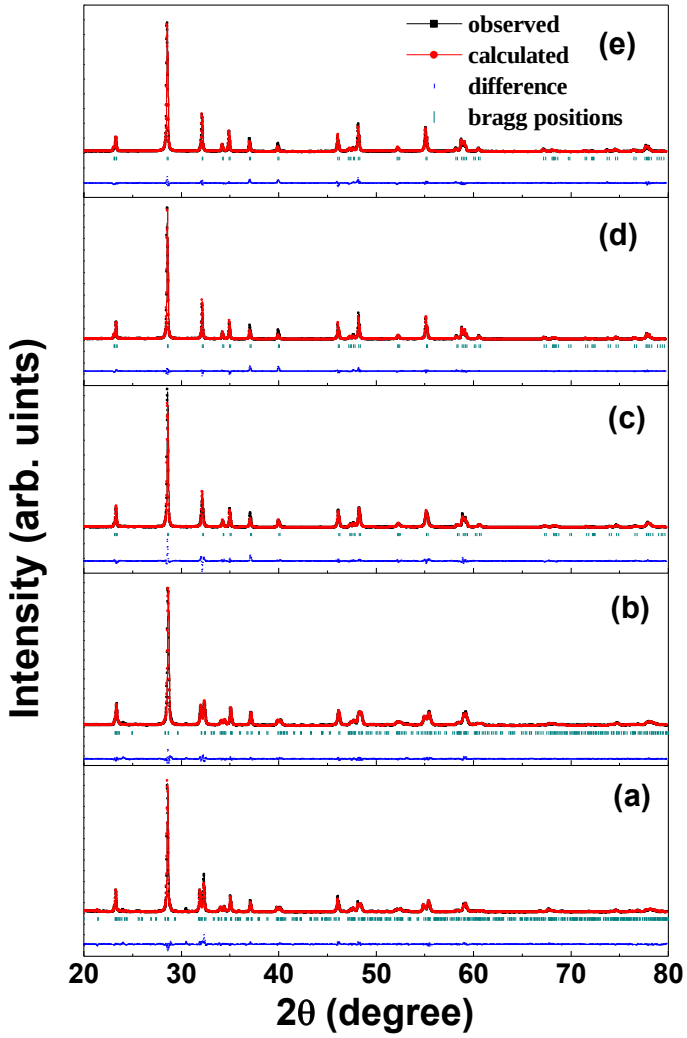

Figure 4.26 XRD patterns of sintered $Bi_4V_{2-x}ME_xO_{11-\delta}$ ($0.0 \leq x \leq 0.20$; ME = Sr^{2+}) (a) x = 0.0, (b) x = 0.05, (c) x = 0.10, (d) x = 0.15 and (e) x = 0.20.

Similar trend has also been observed for $Bi_2Sr_xV_{1-x}O_{5.5-(3x/2)-\delta}$ and $(Bi_{1-x}La_x)_4V_2O_{11-\delta}$, $Bi_4(V_{1-x}Fe_x)_2O_{11-\delta}$ [55, 57]. It is reported in literature that $Bi_4V_2O_{11-\delta}$ is a system with inherent oxygen vacancies and can accommodate most of the divalent cations irrespective of their ionic radii at vanadium site. The substitution of vanadium leads to the stabilization of γ-phase at room temperature [60, 61]. Thus, the stabilization of γ- phase at room temperature in the present case supports the substitution of V^{5+} by Sr^{2+} [10, 62]. The effect of ion radii in terms of shifting of XRD peaks towards lower 2θ values as compared to Mg^{2+} and Ca^{2+} doped samples is also observed for Sr^{2+} doped samples. The effect of Sr doping in $Bi_4V_{2-x}ME_xO_{11-\delta}$

was also investigated with the help of Williamson Hall method [19, 20]. The plot βcosθ vs. 4sinθ were used to calculate the strain for all the samples. The positive value of strain depicts the tensile strain generated in the system with doping [21].

4.3.2 Analysis of FTIR spectra

FTIR spectra of $Bi_4V_{2-x}ME_xO_{11-\delta}$ ($0.0 \leq x \leq 0.20$; ME = Sr^{2+}) before and after sintering at 800 °C for 12 h are shown in Figure 4.27 and 4.28. In bismuth vanadate based systems, different bands, at ~ 468 cm^{-1}, ~ 519 cm^{-1}, ~ 624 cm^{-1}, ~ 732 cm^{-1}, ~ 767 cm^{-1} and ~ 801 cm^{-1} are expected. Bands at ~ 468 cm^{-1} and ~ 519 cm^{-1} could be related to the symmetric bending vibration of Bi-O bonds in BiO_3 pyramidal structural units. Whereas, bands at ~ 732 cm^{-1} and ~ 801 cm^{-1} are generated due to the vibration of symmetric modes of V- O-V bonds and V-O-V chains, respectively [23]. Another band, at ~ 931 cm^{-1} is visible in the spectra of sintered samples which can be assigned to the vibrations of VO_4 polyhedra [8, 22-24]. Bands in case of quenched samples are found to be broader and diffused as compared to sintered samples. The sharpness of bands can be related to the presence of higher structural ordering in sintered than quenched samples [63].

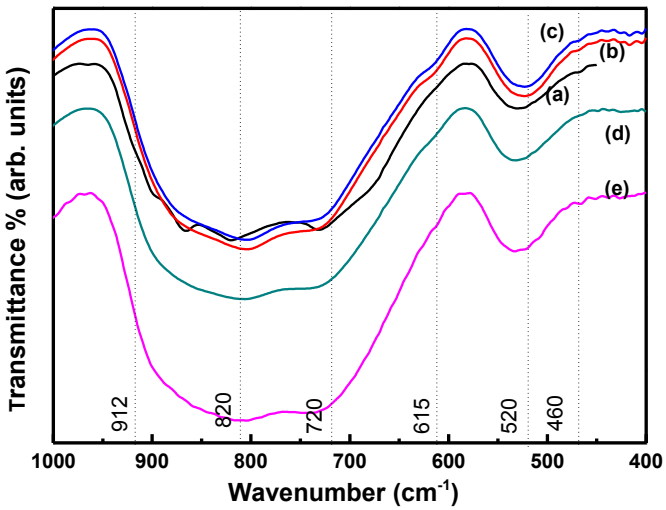

Figure 4.27 FTIR spectra for quenched $Bi_4V_{2-x}ME_xO_{11-\delta}$ ($0.0 \leq x \leq 0.20$; ME = Sr^{2+}) (a) x=0.0, (b) x=0.05, (c) x=0.10, (d) x=0.15 and (e) x=0.20.

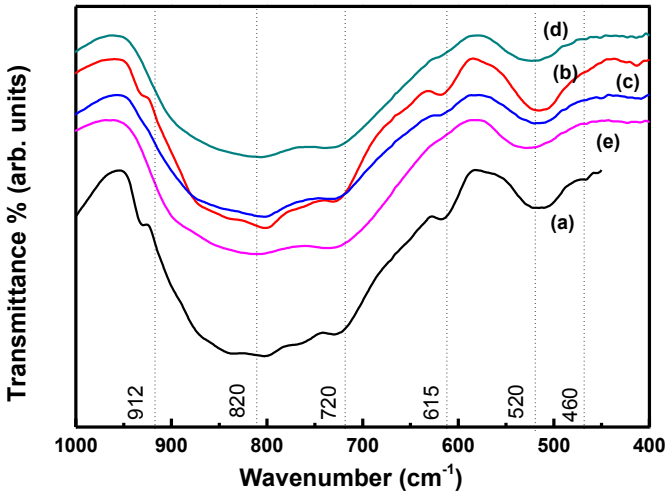

Figure 4.28 FTIR spectra for sintered $Bi_4V_{2-x}ME_xO_{11-\delta}$ ($0.0 \leq x \leq 0.20$; ME = Sr^{2+}) (a) x=0.0, (b) x=0.05, (c) x=0.10, (d) x=0.15 and (e) x=0.20.

The XRD patterns of sintered samples also become sharper than quenched samples as discussed in the previous section. The FTIR spectra clearly show that x = 0.05 sintered sample is better resolved and has sharp bands than x = 0.05 quenched sample. Obviously, x = 0.05 sample transforms to β- phase after sintering which is more ordered than γ- phase. The broadness of the FTIR bands can also be explained on the basis of addition of the sum of a number of absorption bands generated due to minor variation of bond lengths and angles [30]. FTIR analysis of the system also reveals the disappearance of band at ~ 912 cm^{-1} with increase in amount of dopant atom. This observation is attributed to the increasing occupancy of V^{5+} by Sr^{2+}. Also the broadening of V- O-V bands at ~ 820 cm^{-1} can be related to the increase in disorderdness of the system due to the substitution of V^{5+} by Sr^{2+} [24, 30].

4.3.3 Microstructural analysis

The typical scanning electron micrographs of doped sintered samples are shown in Figure 4.29. A non-uniform grain growth is observed in both the samples. The non-uniform grain growth of the grains can be related to the kinetics of the motion of particles along the boundaries of the grains [31]. In addition to this, liquid phase sintering is also observed in the both the samples. The grain size of the samples is found to increase with Sr^{2+} concentration

Figure 4.30. Therefore, the number of grain boundaries decrease, which are more resistive than grains. Thus, the conductivity of the samples increases with Sr^{2+} concentration [64-67].

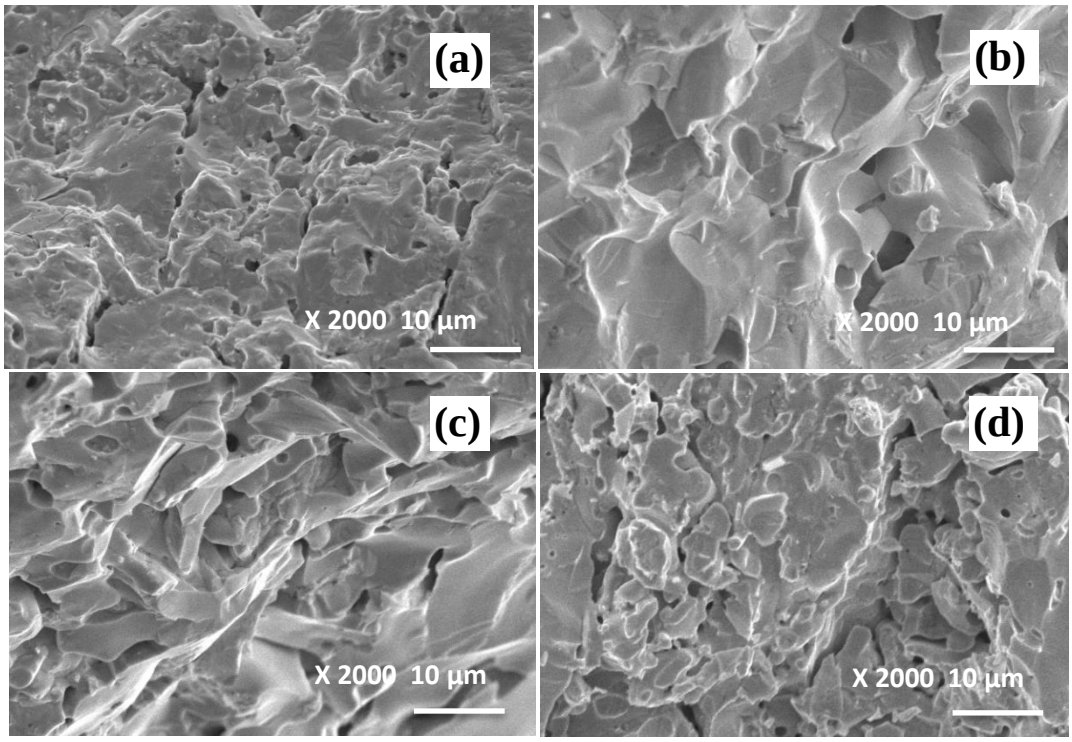

Figure 4.29 Scanning electron micrographs for sintered $Bi_4V_{2-x}ME_xO_{11-\delta}$ ($0.05 \leq x \leq 0.20$; ME = Sr^{2+}) (a) x=0.05, (b) x=0.10, (c) x=0.15 and (d) x=0.20.

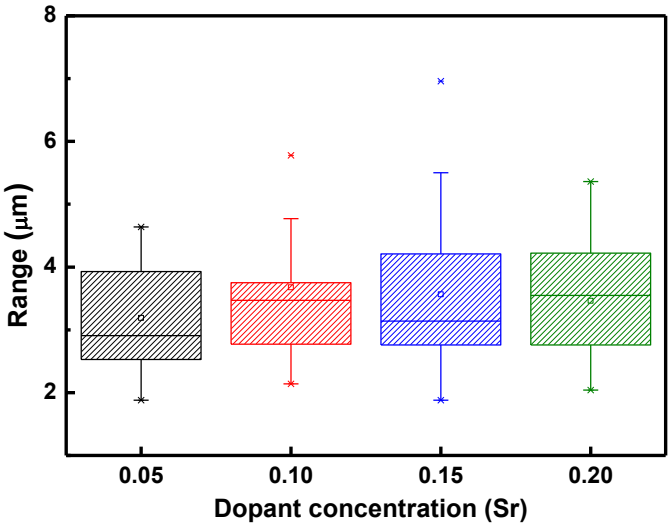

Figure 4.30 Grain size for sintered $Bi_4V_{2-x}ME_xO_{11-\delta}$ ($0.05 \leq x \leq 0.20$; ME = Sr^{2+}).

4.3.4 Dilatometry

Dilatometric analysis of $Bi_4V_{2-x}ME_xO_{11-\delta}$ ($0.0 \leq x \leq 0.20$; ME = Sr^{2+}) quenched samples was carried out to check their linear expansion with respect to temperature.

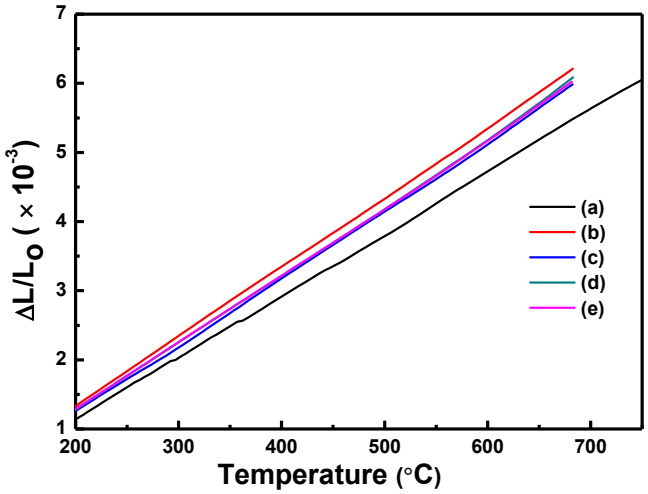

Figure 4.31 Dilatometric curves for quenched $Bi_4V_{2-x}ME_xO_{11-\delta}$ ($0.0 \leq x \leq 0.20$; ME = Sr^{2+}) (a) x=0.0, (b) x=0.05, (c) x=0.10, (d) x=0.15 and (e) x=0.20.

Table 4.12 Thermal expansion coefficients for quenched $Bi_4V_{2-x}ME_xO_{11-\delta}$ ($0.0 \leq x \leq 0.20$; ME = Sr^{2+}).

Composition	As quenched samples TEC (/°C)
$Bi_4V_2O_{11-\delta}$	8.8×10^{-6}
$Bi_4V_{1.95}Sr_{0.05}O_{11-\delta}$	10.0×10^{-6}
$Bi_4V_{1.90}Sr_{0.10}O_{11-\delta}$	9.74×10^{-6}
$Bi_4V_{1.85}Sr_{0.15}O_{11-\delta}$	9.79×10^{-6}
$Bi_4V_{1.80}Sr_{0.20}O_{11-\delta}$	9.72×10^{-6}

TECs calculated from the curves $\Delta L/L_o$ vs. temperature shown in Figure 4.31 for quenched $Bi_4V_{2-x}ME_xO_{11-\delta}$ ($0.0 \leq x \leq 0.20$; ME = Sr^{2+}) samples. The values of TECs in the temperature

range 200-700 °C are listed in Table 4.12. There is only slight difference in TEC values for all the samples. However, the maximum value of TEC is observed for x= 0.05 sample. The higher values of TEC of doped samples can be explained on the basis of greater ionic radii of dopant than host atom which leads to shallowness in asymmetric potential well.

4.3.5 Thermal analysis

In order to study the various phase transitions and thermal stability of sintered samples differential scanning calorimetry (DSC) and thermogravimetric (TG) analysis were carried out. The DSC curve of the sintered sample with composition $Bi_4V_{1.95}Sr_{0.05}O_{11-\delta}$ exhibits two endothermic peaks corresponding to phase transformations $\alpha \rightarrow \beta$ (~ 383 °C) and $\beta \rightarrow \gamma$ (~ 475 °C), respectively.

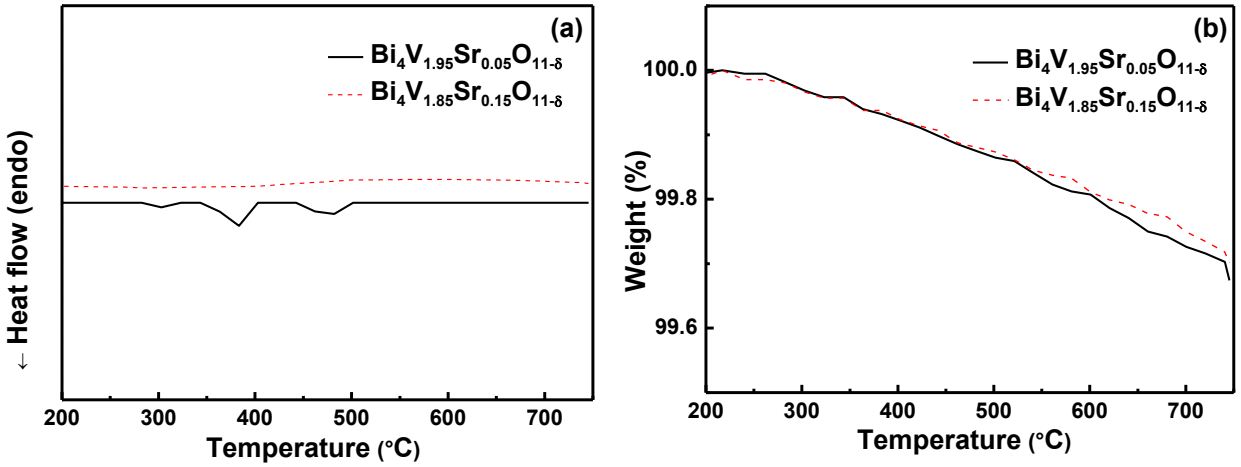

Figure 4.32 Thermal analysis for sintered $Bi_4V_{1.95}Sr_{0.05}O_{11-\delta}$ and $Bi_4V_{1.85}Sr_{0.15}O_{11-\delta}$ (a) DSC analysis and (b) TG analysis.

Whereas, no transition is observed in the DSC curves for $Bi_4V_{1.85}Sr_{0.15}O_{11-\delta}$ sample (Figure 4.32 (a)). Similar to that of Mg^{2+} and Ca^{2+} doped samples Sr^{2+} doped sintered samples (Figure 4.38 (b)) also show negligible weight loss indicating the high stability of synthesized compounds. This slight weight loss can be attributed to the reduction of vanadium during TGA measurement [38].

4.3.6 Electrical conductivity

The total conductivity of the samples was obtained using impedance analyser. The total resistance of the sample was estimated from the graphs between real and imaginary parts of impedance i.e. Nyquist plots [39]. Various kinds of Nyquist plots were fitted to various equivalent circuits as discussed in section 4.1.6.

Table 4.13 Density, ionic conductivity and activation energy for sintered $Bi_4V_{2-x}ME_xO_{11-\delta}$ ($0.0 \leq x \leq 0.20$; ME = Sr^{2+}).

Composition	Density (g cm^{-3})	$\sigma_{500°C}$ (Scm^{-1}) ($\times 10^{-4}$)	E_a (eV) (200 - 560 °C)	E_a (eV) (560 - 750 °C)
$Bi_4V_2O_{11-\delta}$	7.42	0.10	0.83	1.13
$Bi_4V_{1.95}Sr_{0.05}O_{11-\delta}$	7.35	0.03	0.83	0.71
$Bi_4V_{1.90}Sr_{0.10}O_{11-\delta}$	7.49	0.20	1.03	0.91
$Bi_4V_{1.85}Sr_{0.15}O_{11-\delta}$	7.30	0.45	0.97	0.82
$Bi_4V_{1.80}Sr_{0.20}O_{11-\delta}$	7.21	1.16	1.28	0.68

The values of conductivity at particular temperature along with activation energies; E_a are listed in Table 4.13. The increase in value of conductivity is observed with the increase in amount of dopant (Figure 4.33). Thus, it can be said that the number of oxygen vacancies is increasing with increase in doping. This increase in conductivity can also be attributed to the increase in grain size as discussed in section 4.3.3. The conductivity values obtained are in close agreement with the activation energies. The values of conductivity obtained are found to be on the lower side as compare to Mg^{2+} and Ca^{2+} doped systems.

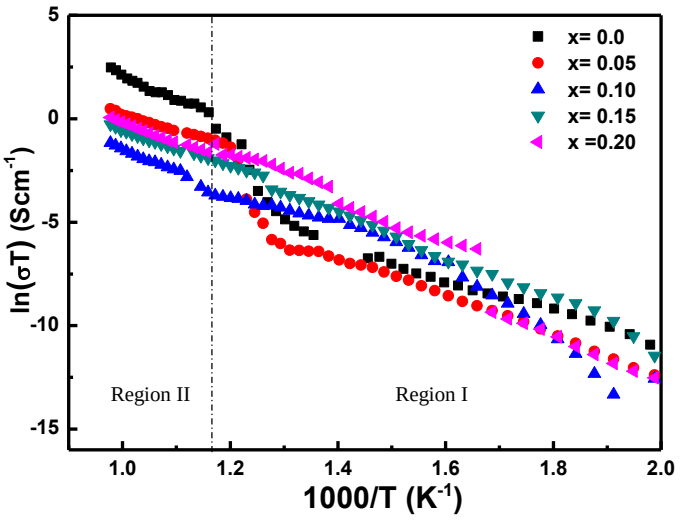

Figure 4.33 Arrhenius plots for sintered $Bi_4V_{2-x}ME_xO_{11-\delta}$ ($0.0 \leq x \leq 0.20$; ME = Sr^{2+}).

4.3.7 UV/ Vis analysis

The value of optical band gap is calculated from the extrapolation of the linear region of the graph $(\alpha\ h\ \nu)^r$ vs. hν [27, 68]. In the present case, the reflectance spectra of powdered samples were taken. The reflectance spectra obtained are shown as shown in Figures 4.34 and 4.35. Therefore, the Kubelka - Munk function was used to calculate the optical band gap. The values of optical band gap can be determined from the curves between $[F(R)h\nu]^r$ and hν. On the similar basis, Urbach energy of the system can also be calculated from the linear portion of the curve between ln F(R) and hν [69, 70]. The observed values of optical band gaps are listed in Table 4.14. The optical band gap in case of sintered samples decreases with increase in amount of doping upto x= 0.15. This can be ascribed due to the increase in the number of oxygen vacancies with the increase in amount of doping to maintain the electroneutrality of the system. As the defects and disorderdness of the system increases, the optical band gap decreases [30].

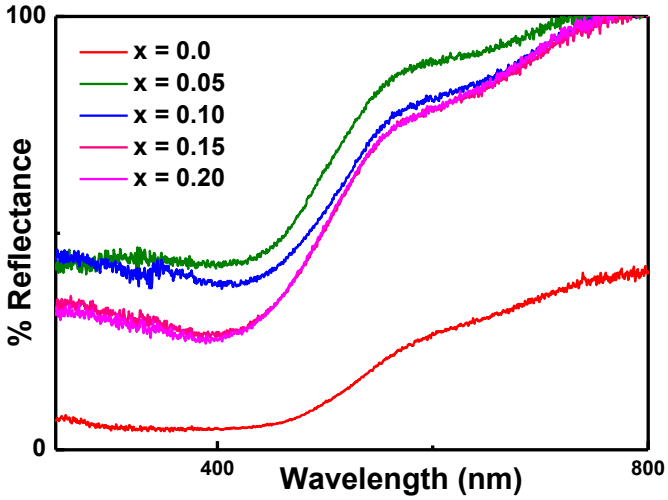

Figure 4.34 Reflectance spectra of quenched $Bi_4V_{2-x}ME_xO_{11-\delta}$ ($0.0 \leq x \leq 0.20$; ME = Sr^{2+}).

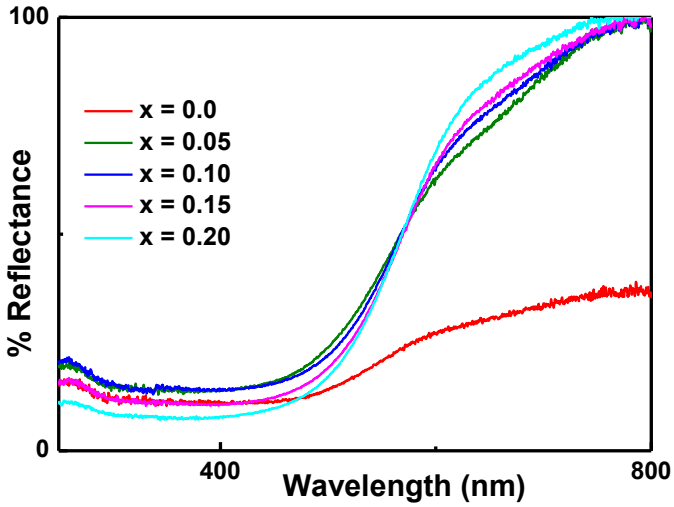

Figure 4.35 Reflectance spectra of sintered $Bi_4V_{2-x}ME_xO_{11-\delta}$ ($0.0 \leq x \leq 0.20$; ME = Sr^{2+}).

The electronegativity difference between host atom, V^{5+} (1.6) and guest atom Sr^{2+} (1.0) can also influence the optical band gap. More is the electronegativity difference between the two atoms more the valence and conduction bands shift towards each other. It leads to the decrease in optical band gap value [8, 70]. After sintering Urbach energy decreases due to some structural relaxation. In general, sintered samples have higher structural ordering than quenched samples which decrease Urbach energy as shown in Table 4.14.

Table 4.14 Values of optical band gap and Urbach energy for quenched and sintered $Bi_4V_{2-x}ME_xO_{11-\delta}$ ($0.0 \leq x \leq 0.20$; ME = Sr^{2+}).

Composition	Quenched samples		Sintered samples	
	E_g (eV)	ΔE (eV)	E_g (eV)	ΔE (eV)
$Bi_4V_2O_{11-\delta}$	2.45	0.41	2.27	0.56
$Bi_4V_{1.95}Sr_{0.05}O_{11-\delta}$	2.52	0.19	2.43	0.20
$Bi_4V_{1.90}Sr_{0.10}O_{11-\delta}$	2.49	0.20	2.39	0.16
$Bi_4V_{1.85}Sr_{0.15}O_{11-\delta}$	2.53	0.17	2.40	0.12
$Bi_4V_{1.80}Sr_{0.20}O_{11-\delta}$	2.57	0.18	2.47	0.10

XRD data and conductivity of sintered samples also support the UV/ visible data. The optical band gap values are in the semiconducting range [48]. Higher optical band gap values are observed in case of Sr^{2+} doped samples as compared to Ca^{2+} doped samples.

4.4 $Bi_4V_{2-x}ME_xO_{11-\delta}$ ($0.0 \leq x \leq 0.20$; ME = Ba^{2+})

Quenched samples exhibit higher disordering than conventionally synthesized samples. Moreover, quenched samples may accommodate high content of Ba^{2+} in the $Bi_4V_{2-x}ME_xO_{11-\delta}$ ($0.0 \leq x \leq 0.20$; ME = Ba^{2+}) system and create more oxygen vacancies in the compound. Based on the above facts, samples were synthesized by melt quench technique followed by the sintering at 800 °C for 12 hours. The obtained results are discussed in the light of vacancies disordering created by dopants and quenching.

4.4.1 X-ray diffraction analysis

The Rietveld refined X- ray diffraction patterns of quenched and sintered $Bi_4V_{2-x}ME_xO_{11-\delta}$ ($0.0 \leq x \leq 0.20$; ME = Ba^{2+}) samples are shown in Figures 4.36 and 4.37.

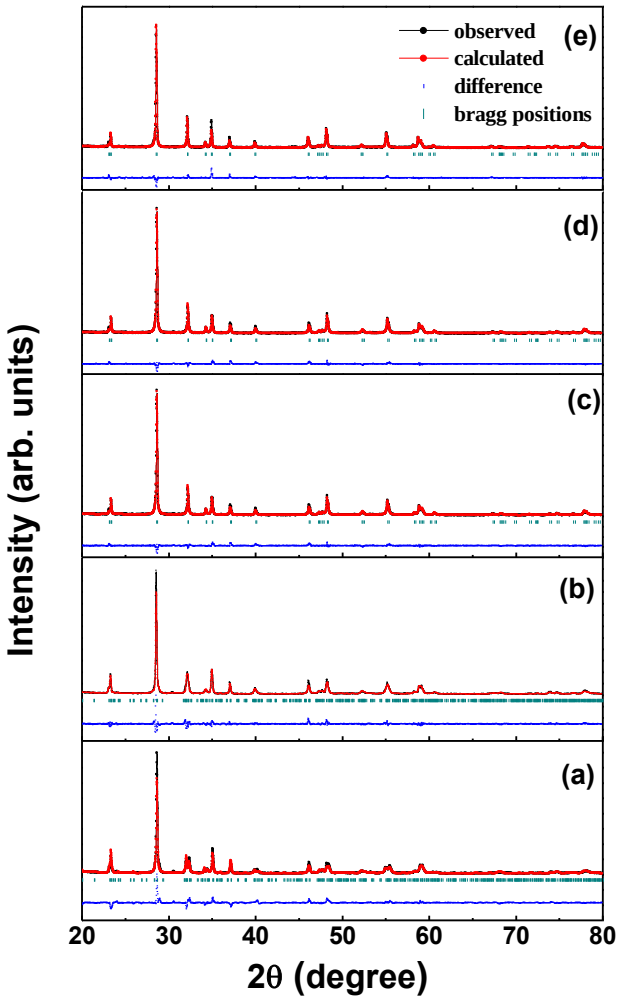

Figure 4.36 XRD patterns of quenched $Bi_4V_{2-x}ME_xO_{11-\delta}$ ($0.0 \leq x \leq 0.20$; ME = Ba^{2+}) (a) x = 0.0, (b) x = 0.05, (c) x = 0.10, (d) x = 0.15 and (e) x = 0.20.

The XRD patterns of quenched samples indicate the different crystalline phases stabilized at room temperature. These crystalline phases do not transform even after heat treatment at 800 °C for 12 h. The parameters obtained for doped and undoped samples are consistent with the earlier reported values [33, 71].

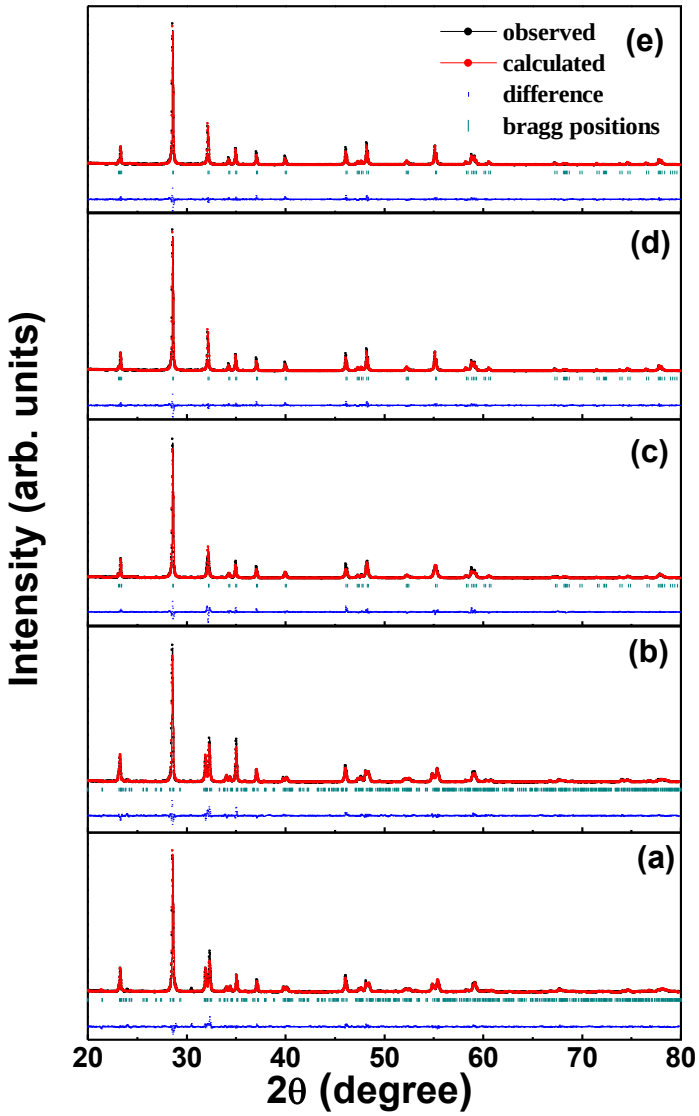

Figure 4.37 XRD patterns of sintered $Bi_4V_{2-x}ME_xO_{11-\delta}$ ($0.0 \leq x \leq 0.20$; ME = Ba^{2+}) (a) x = 0.0, (b) x = 0.05, (c) x = 0.10, (d) x = 0.15 and (e) x = 0.20.

A superstructure peak at ~ 24.4° for $0.0 \leq x \leq 0.05$ samples is observed in both quenched as well as sintered samples. As compared to all the above three series the stabilization of γ-phase takes place at higher amount of Ba^{2+} doped system. It is related to the monoclinic phase with *C2/m* space group. With increasing amount of substitution, coalescence of the

XRD peak at ~ 32° (1 1 0) is observed as shown in Figures 4.36 and 4.37. The XRD patterns of composition $0.10 \leq x \leq 0.20$ are well fitted with the tetragonal phase with *I4/mmm* space group having $\chi^2 \leq 2$. The residual parameters R_p and R_{wp} in all the cases are found to be below 10%. Thus, it has been observed that with the increasing level of substitution the present compound attains the γ- structure at room temperature due to creation of oxide ion vacancies. Similar kinds of results have been reported with various substituents such as Al^{3+}, Li^+ and Ag^+ for bismuth vanadate [59, 72]. Structurally, bismuth vanadate consists of $(Bi_2O_2)^{2+}$ and $(VO_3\square_{0.5})^{2-}$ (□: oxygen vacancies) layers. The oxygen atoms coordinated to vanadium show high multiplicity. The defect structure of $Bi_4V_2O_{11-\delta}$ emerges from the partial filling of oxygen sites in $(VO_3\square_{0.5})^{2-}$ layers. During refinement, O(1) atom is supposed to be bonded to Bi^{3+} and is fully occupied with least positional disorder. Even, the substitution at Bi site does not produce disorder [73]. Whereas, O(2), O(3) and O(4), the split oxygen positions are coordinated to V^{5+} with partial occupancy by oxygen atoms. O(2) and O(4) are apical positions and cannot be simultaneously occupied this partial filling of oxygen atoms distorts the O(3), equatorial position by converting it from ideal 4-fold to an 8-fold site. Thus, to maintain the electroneutrality the true occupancy of equatorial site is lower than 0.5. The oxygen vacancies are generated at the equatorial position in the $(VO_3\square_{0.5})^{2-}$ layer [1, 10, 35]. Hence, the vacancies are restricted in $(VO_3\square_{0.5})^{2-}$ layer at equatorial position in the system. Various refined lattice parameters are listed in Table 4.15. It is clear from the refined parameters that the lattice parameter 'a' is on the lower side in quenched samples than sintered samples, indicating the higher number of oxygen vacancies in quenched samples. Basically, oxygen ordering phenomena in $Bi_4V_2O_{11-\delta}$ is restricted to the basal plane and the substitution of lower valence atom for V^{5+} site generates oxygen vacancies in the equatorial position [71]. Thus, the loss of oxygen with generation of oxygen vacancies results in a decrease of 'a' parameter [74]. The increase in lattice parameter 'c' can be associated with

the difference between the size of dopant Ba^{2+} (1.35 Å) and host V^{5+} (0.54 Å). Similar results, have been reported for ME = Mn^{2+} [6], Zr^{4+} and Sn^{4+} doping at V site in $Bi_4V_{2-x}ME_xO_{11-x/2}$ [75]. In the present system, the lower concentration of substitution leads to stabilization of the γ- phase as compared to earlier reports on similar systems. This difference is associated with the processing techniques used. On comparing the XRD peaks of earlier discussed systems with Ba^{2+} doped samples shifting of Ba^{2+} doped sample peaks towards lower values of 2θ is observed. It might be due to the strain created in lattice because of the greater size of Ba^{2+} (1.35 Å) than Sr^{2+} (1.18 Å). This observation can be confirmed by using the Williamson Hall equation. Thus the strain induced in the lattice is calculated with the help of Williamson Hall analysis [18]. Higher values of strain are obtained for sintered samples in case of Ba^{2+} doping. Thus, from the Williamson Hall plot, it can be concluded that the strain induced by Ba^{2+} is more than any other system discussed above. The values of strain are observed to be positive depicting generation of tensile strain in the system. The tensile strain observed in the samples can be suggested, due to the greater ionic radii of dopant atom than that of host atom in the present systems [21].

Table 4.15 Rietveld refined parameters for quenched and sintered $Bi_4V_{2-x}ME_xO_{11-\delta}$ ($0.0 \leq x \leq 0.20$; ME = Ba^{2+}).

Quenched Samples					Goodness parameters of fitting		Sintered Samples				Goodness parameters of fitting	
Composition	**a (Å)**	**b (Å)**	**c (Å)**	**Volume ($Å^3$)**	**R_{exp}**	**χ^2**	**a (Å)**	**b (Å)**	**c (Å)**	**Volume ($Å^3$)**	**R_{exp}**	**χ^2**
$Bi_4V_2O_{11-\delta}$	5.587	15.350	16.596	1423.445	6.94	2.67	5.599	15.338	16.599	1425.664	8.46	2.18
$Bi_4V_{1.95}Ba_{0.05}O_{11-\delta}$	5.574	15.382	16.649	1427.372	8.46	2.53	5.599	15.355	16.612	1428.294	8.39	2.19
$Bi_4V_{1.90}Ba_{0.10}O_{11-\delta}$	3.930	3.930	15.385	237.676	8.33	1.55	3.933	3.933	15.389	238.026	8.39	2.26
$Bi_4V_{1.85}Ba_{0.15}O_{11-\delta}$	3.932	3.932	15.397	238.084	8.57	1.47	3.935	3.935	15.391	238.333	8.40	1.40
$Bi_4V_{1.80}Ba_{0.20}O_{11-\delta}$	3.939	3.939	15.413	239.118	8.44	1.60	3.939	3.939	15.419	239.272	8.32	1.56

4.4.2 Analysis of FTIR spectra

FTIR spectra of as quenched and sintered samples $Bi_4V_{2-x}ME_xO_{11-\delta}$ ($0.0 \leq x \leq 0.20$; ME = Ba^{2+}) were obtained. With increase in amount of doping the absorption bands in different spectra shift towards higher wavenumber. This can be attributed to size difference between the host atom and dopant atom. In addition to this, the larger ionic radius of dopant Ba^{2+}, increases the bond length of Ba-O bond. Thus, the absorption band shift towards larger wavenumber as also observed in the case of doped samples [26]. Usually, the FTIR spectra of undoped bismuth vanadate exhibit seven absorption bands namely at ~ 468 cm^{-1}, ~ 519 cm^{-1}, ~ 624 cm^{-1}, ~ 732 cm^{-1}, ~ 767 cm^{-1} and ~ 801 cm^{-1}. Out of them, bands at ~ 468 cm^{-1} and ~ 519 cm^{-1} can be assigned to symmetric bending vibration of Bi-O bonds in BiO_3 pyramidal units. On the other hand, the band at ~ 732 cm^{-1} is generated due to the vibration of symmetric modes of V-O-V bonds. The vibrations due to V-O-V chains belong to the absorption band at ~ 801 cm^{-1} [22-24]. In all the FTIR spectra, a band at ~ 930 cm^{-1} is also observed which can be arisen due to the vibrations of VO_4 polyhedra. With the increase in amount of doping the band at ~ 730 cm^{-1} is getting broader. Also, this band is broader in case of sintered samples when compared to the quenched samples. This broadening can be related to the sum of a number of absorption bands generated due to the variation of bond lengths and angles. These changes in the absorption bands have arisen with the introduction of Ba atoms in the undoped bismuth vanadate. Also, in the samples with $x > 0.0$ the intensity of the band at ~ 801 - 866 cm^{-1} is decreasing. This can be probably due to the cleavage of V-O-V bonds. So, the appearance of new band at ~ 864 cm^{-1} can be attributed to the formation of bonds V-O-Ba in tetrahedral coordination. It is clearly indicated that V^{5+} get replaced by Ba^{2+} in $(V_2O_4)^{2-}$ perovskite layers. All sintered samples show the blue shift in FTIR bands as compared to as quenched samples.

4.4.3 Microstructural studies

In order to compare the grain size and grain growth of sintered samples with conductivity, SEM analysis was done on all the sintered samples. Gold sputtered fractured samples were used to analyse the microstructures. A non- uniform growth of grains in undoped and doped samples is observed. For all the sintered samples, a dense shell-like structure is observed as shown Figure 4.38 (a) and (b). These features are also indicated by the arrow in Figure 4.48 (a) and (b). Sample $Bi_4V_{1.95}Ba_{0.05}O_{11-\delta}$ exhibits some micro cracks.

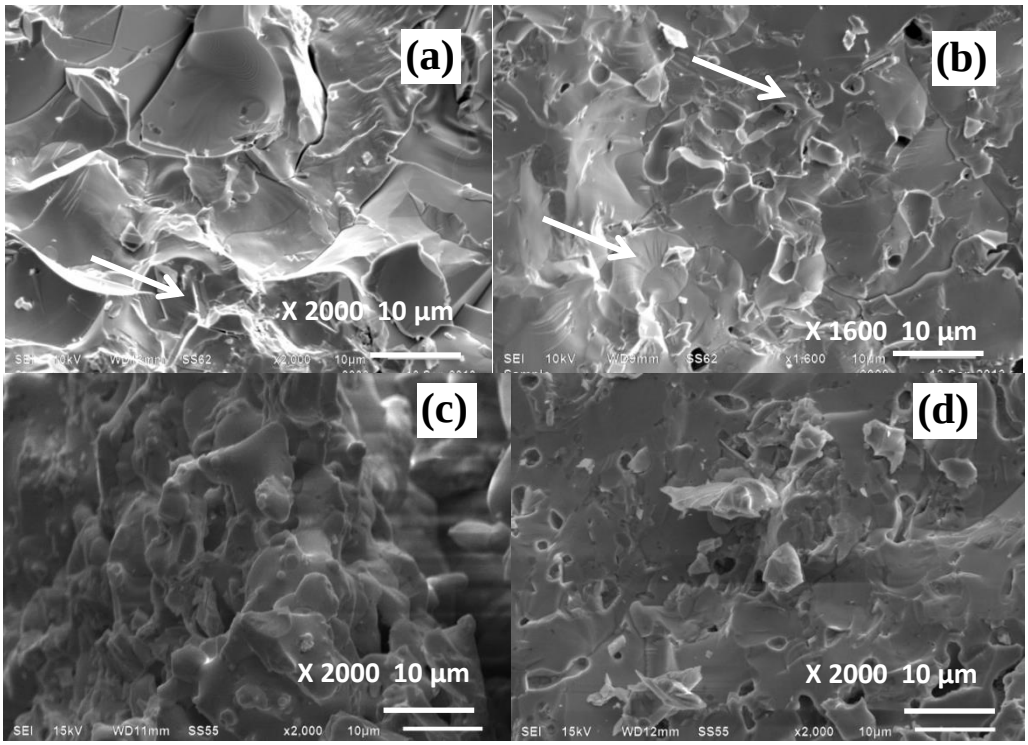

Figure 4.38 Scanning electron micrographs for sintered $Bi_4V_{2-x}Ba_xO_{11-\delta}$ ($0.05 \leq x \leq 0.20$) (a) x=0.05, (b) x=0.10, (c) x=0.15 and (d) x=0.20.

The fractures are trans-granular and this feature is common in brittle materials [76]. Well-connected grains fracture due to strain development during heat treatment of the sample. For all the samples with increasing level of substitution the faceted type grains convert to round shape grains. The grain size of all the samples is found to be non-uniform. The non-uniformity of large grains can be correlated to the kinetics of movement of particles from boundary to boundary, as the boundary energy is dependent on the grain boundary orientation

and grain boundary mobility [31]. The average grain size of samples decreases with dopant concentration. The average grain sizes for x = 0.0, 0.05, 0.10, 0.15 and 0.20 samples are 18, 11, 4.5, 4.0 and 3.0 μm, respectively. EDS was performed on the selected samples, to semi quantitatively determine the elemental content of the samples. The EDS analysis of different points of the same sample shows nearly the same elemental distribution of all the initial constituting elements. MP-AES analysis of the quenched samples was also carried out to determine the elemental concentration of bismuth, vanadium and barium as shown in Table 4.16. The Bi/ V and V/ Ba experimental ratios in all the samples are observed to be close to the theoretical values. Some variations in the ratios suggest some losses take place during synthesis process. However, these losses do not appear to affect the stabilization of the γ-phase as confirmed by the XRD results.

Table 4.16 MP-AES analysis data for $Bi_4V_{2-x}ME_xO_{11-\delta}$ ($0.0 \leq x \leq 0.20$; ME = Ba^{2+}).

Composition	Bi/V atomic fraction		V/Ba atomic fraction	
	Theoretical	Experimental	Theoretical	Experimental
$Bi_4V_2O_{11-\delta}$	2.0	2.12	---	---
$Bi_4V_{1.95}Ba_{0.05}O_{11-\delta}$	2.05	2.18	39.0	34.61
$Bi_4V_{1.90}Ba_{0.10}O_{11-\delta}$	2.10	2.19	19.0	17.90
$Bi_4V_{1.85}Ba_{0.15}O_{11-\delta}$	2.16	2.31	12.33	12.28
$Bi_4V_{1.80}Ba_{0.20}O_{11-\delta}$	2.22	2.41	9.0	9.01

4.4.4 Dilatometry

Dilatometric analysis of $Bi_4V_{2-x}ME_xO_{11-\delta}$ ($0.0 \leq x \leq 0.20$; ME = Ba^{2+}) quenched samples and sintered was carried out to check their linear expansion with respect to temperature. TECs were calculated from the linear fit of the curves $\Delta L/L_o$ vs. temperature. The values of TECs

in the temperature range 200-700 °C are listed in Table 4.17. No particular trend is followed in the TEC values for both quenched and sintered samples. However, the maximum value of TEC is observed for x= 0.05 sintered sample. It is also manifested that higher disorderdness in the material leads to higher TEC value. Thus, it can be expected that x = 0.05 sample is the most oxygen deficient or disordered sample among all the sintered samples. The higher TEC values of doped samples can be explained on the basis of greater ionic radii of dopant than host atom. Since the ionic radii of Ba^{2+} is higher than V^{5+} the TEC of doped samples increases.

Table 4.17 Thermal expansion coefficients for quenched and sintered $Bi_4V_{2-x}ME_xO_{11-\delta}$ ($0.0 \leq x \leq 0.20$; ME = Ba^{2+}).

Composition	As quenched samples TEC (/°C)	Sintered samples TEC (/°C)
$Bi_4V_2O_{11-\delta}$	8.8×10^{-6}	8.9×10^{-6}
$Bi_4V_{1.95}Ba_{0.05}O_{11-\delta}$	9.29×10^{-6}	8.80×10^{-6}
$Bi_4V_{1.90}Ba_{0.10}O_{11-\delta}$	8.73×10^{-6}	9.28×10^{-6}
$Bi_4V_{1.85}Ba_{0.15}O_{11-\delta}$	9.12×10^{-6}	8.77×10^{-6}
$Bi_4V_{1.80}Ba_{0.20}O_{11-\delta}$	8.73×10^{-6}	8.98×10^{-6}

4.4.5 Thermal analysis

Differential scanning calorimetry (DSC) and thermogravimetric (TG) analysis were carried out to study the various phase transitions and thermal stability of sintered samples. A typical DSC curve of the sintered sample with composition x = 0.0 exhibits two endothermic peaks as shown in Figure 4.39 (a) these peaks correspond to phase transformations $\alpha \rightarrow \beta$ (~ 426 °C) and $\beta \rightarrow \gamma$ (~ 520 °C). On the other hand, the DSC curve of the x = 0.15 sample does not exhibit any peaks, which clearly indicates the γ- phase stabilization at room temperature. In general $\gamma' \leftrightarrow \gamma$ phase transformation is observed in between 450-500 °C [37]. This

transformation ($\gamma' \leftrightarrow \gamma$) is not observed in DSC curves. However, the conductivity data shows the phase transition with the reduction in value of ionic conductivity ~ 560 °C. The TG curve of the x = 0.0 sintered sample shows negligible weight loss upto 300 °C. In contrast, the x = 0.05 sintered sample (Figure 4.39 (b)) shows slightly higher weight loss than for the x = 0.0 sample. The weight loss can be associated with oxygen loss due to reduction of vanadium during TGA measurement [38]. The minimum weight loss is observed in the $Bi_4V_{1.85}Ba_{0.15}O_{11-\delta}$ sample as compared to Mg^{2+}, Ca^{2+} and Sr^{2+} doped samples. Thus, $Bi_4V_{1.85}Ba_{0.15}O_{11-\delta}$ can be supposed to be the most thermally stable composition.

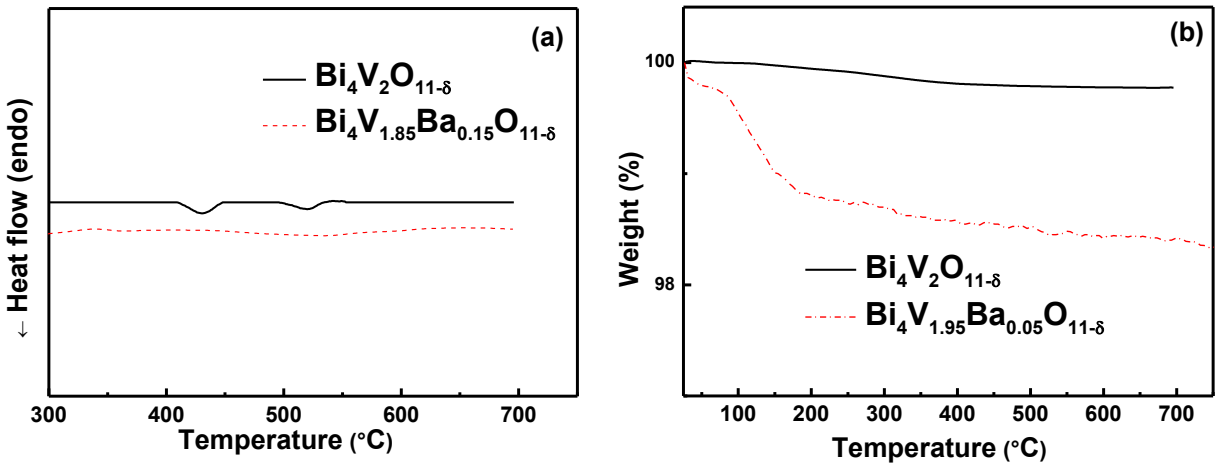

Figure 4.39 Thermal analysis for sintered (a) DSC analysis $Bi_4V_2O_{11-\delta}$, $Bi_4V_{1.85}Ba_{0.1\,5}O_{11-\delta}$ and (b) TG analysis $Bi_4V_2O_{11-\delta}$, $Bi_4V_{1.95}Ba_{0.05}O_{11-\delta}$.

4.4.6 Electrical conductivity

The values of resistance were calculated from the fitting of Nyquist plots to different circuits at different temperatures as shown in Figure 4.40. The temperature dependence of electrical conductivity is analyzed by plotting the graphs 1000/T vs. log (σ T). The activation energy is calculated from the slope of Arrhenius plots (Figure 4.41) [42, 43]. The value of resistance is found to get decrease with the increase in temperature, which is an indication of high temperature ionic conductor materials [40, 58, 78-80]. The highest value of conductivity is observed for x = 0.05 sample ~2.52 × 10^{-4} Scm^{-1} at 400 °C. At higher temperatures, as the

amount of substituent is increased slight decrease in the value of conductivity is observed which may be explained on the basis of the number of oxide ion vacancies.

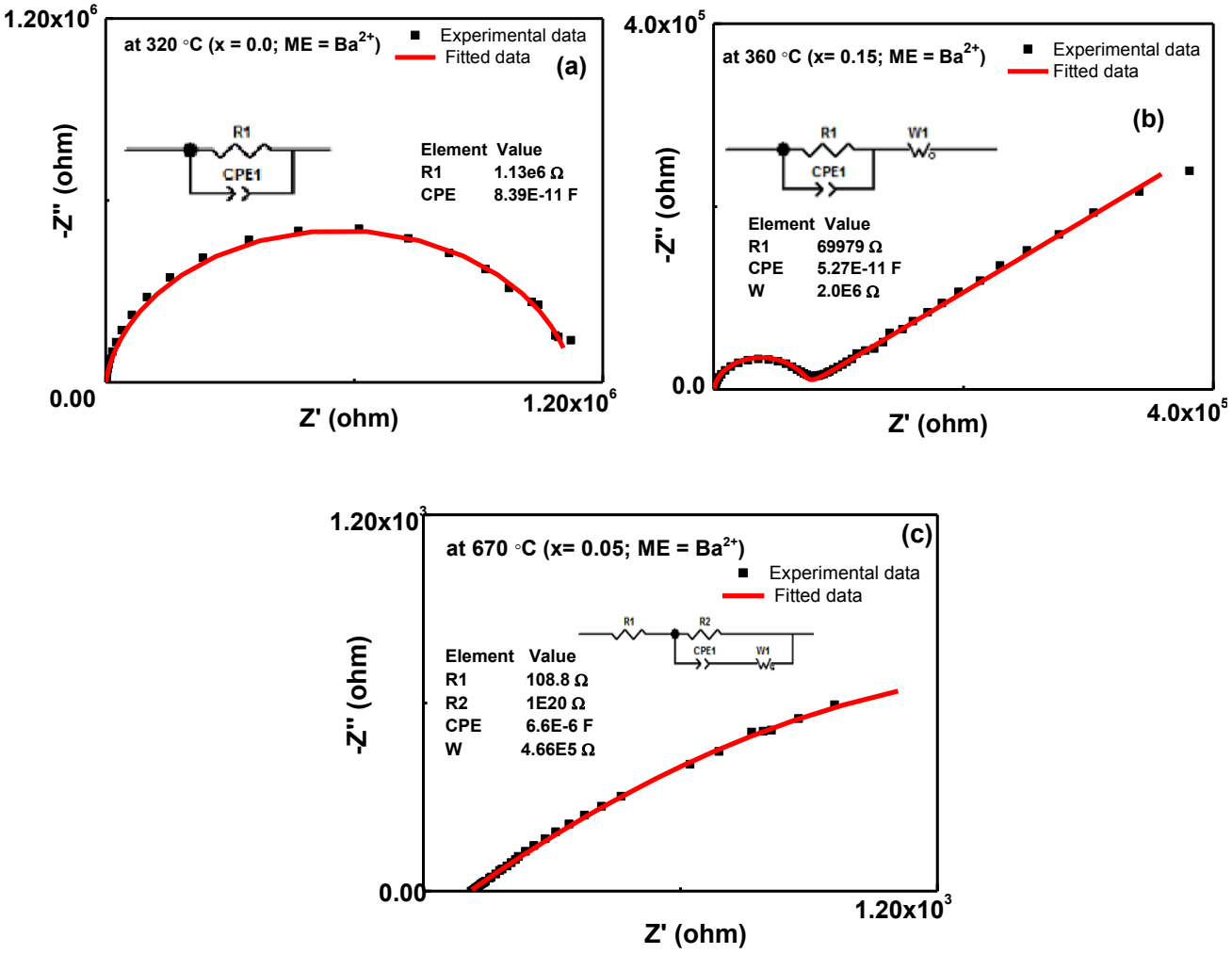

Figure 4.40 Nyquist plots and corresponding equivalent circuits for sintered $Bi_4ME_xV_{2-x}O_{11-\delta}$ ($0.0 \leq x \leq 0.20$; ME = Ba^{2+}) at different temperatures.

With the increase in value of substituent the large increase in the number of oxide ion vacancies takes place which causes the defect clustering or ordering and hence decreases the conductivity [81, 82]. Value of conductivity not only depends on the number of oxygen vacancies generated, but also on the ratio of ionic charge and size of the dopant cations called ionic potential (ϕ) [44]. Actually, more is the value of the ionic potential of an atom more will be its ion polarizability. Therefore, the value of conductivity increases with the increase in value of ionic potential. In present case, the lowering of value of conductivity with increase in amount of substitution can be suggested to be due to lower ionic potential of Ba^{2+} (1.48).

As the amount of substitution Ba^{2+} increases, it could have created hindrance for the movement of oxide ions. Similarly, it has been reported by Sharma *et al.* [45] that ionic conductivity of Li^{+} among various substituted cations such as Zn^{2+}, Al^{3+}, Ti^{4+} and Ge^{4+} in $Bi_4V_2O_{11-\delta}$ is lowest due to low ionic potential i.e. 1.32. Also, at higher temperature the large decrease in the value of conductivity for 0.10, 0.15 and 0.20 (γ- phase stabilized) samples could be thought of as a result of ordering in oxygen vacancies with the transformation of γ → γ′ (phase) with the increase in amount of substitution [3, 46]. However, this type of phase transition is not observed in DSC curve (Figure 4.39 (a)). Arrhenius plots as shown in Figure 4.41 can be divided into two linear regions region I and II, with two different values of activation energy one at higher values of temperature and second one at lower values of temperature. The values of conductivities and activation energies for different temperature ranges are listed in Table 4.18. The trend of activation energies is in accordance with the conductivity values. The various phase transformations taking place in the system can also be depicted from the change in the slope Arrhenius plots.

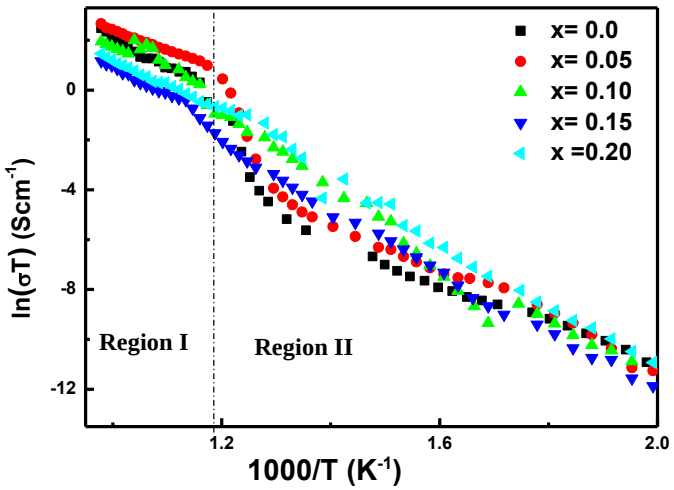

Figure 4.41 Arrhenius plots for sintered $Bi_4V_{2-x}ME_xO_{11-\delta}$ ($0.0 \leq x \leq 0.20$; ME = Ba^{2+}).

In the Arrhenius plot for x = 0.0 sample the slope change is observed ~ 462 and ~ 581 °C which are close to the peaks observed in DSC curve for x = 0.0 the slight discrepancy in the peak position can be explained on the basis of sluggishness of the transformations [59, 83].

It is observed that among all the series γ- phase is stabilized for x = 0.15 compositions and the least activation energy is observed for $Bi_4V_{1.85}Ba_{0.15}O_{11-\delta}$ sample. Thus, it would be interesting to further investigate the properties of $Bi_4V_{1.85}Ba_{0.15}O_{11-\delta}$ compound.

Table 4.18 Density, ionic conductivity and activation energy of $Bi_4V_{2-x}Ba_xO_{11-\delta}$ ($0.0 \leq x \leq 0.20$).

Composition	Density ($g\ cm^{-3}$)	$\sigma_{500°C}$ (Scm^{-1}) ($\times 10^{-4}$)	E_a (eV) (200 - 560 °C)	E_a (eV) (560 - 750 °C)
$Bi_4V_2O_{11-\delta}$	7.42	0.10	0.90	1.04
$Bi_4V_{1.95}Ba_{0.05}O_{11-\delta}$	7.16	0.25	0.98	0.74
$Bi_4V_{1.90}Ba_{0.10}O_{11-\delta}$	7.40	1.29	1.10	1.09
$Bi_4V_{1.85}Ba_{0.15}O_{11-\delta}$	7.43	1.23	1.05	0.70
$Bi_4V_{1.80}Ba_{0.20}O_{11-\delta}$	7.02	2.18	1.15	0.85

4.4.7 UV/ Vis analysis

Optical band gaps of the synthesized samples in powder form are calculated from the transmission spectra (Figures 4.42 and 4.43). The optical band gap values of all the quenched and sintered samples along with Urbach energy are listed in Table 4.19. Materials with larger Urbach energy have more tendency to convert the weak bonds into defects. Thus, higher Urbach energy more indicates higher degree of randomness in the system [84]. Quenched samples in comparison to sintered samples exhibit slightly higher Urbach energy as shown in Table 4.19. It is a manifestation of higher defects and disorderdness present in as quenched samples also supported by XRD and FTIR results. The FWHM is also higher in quenched

samples as compared to sintered samples. Similarly, broader bands are observed for as quenched samples. Interestingly, x = 0.15 sintered sample show lowest Urbach energy in comparison to all other samples indicating less randomness.

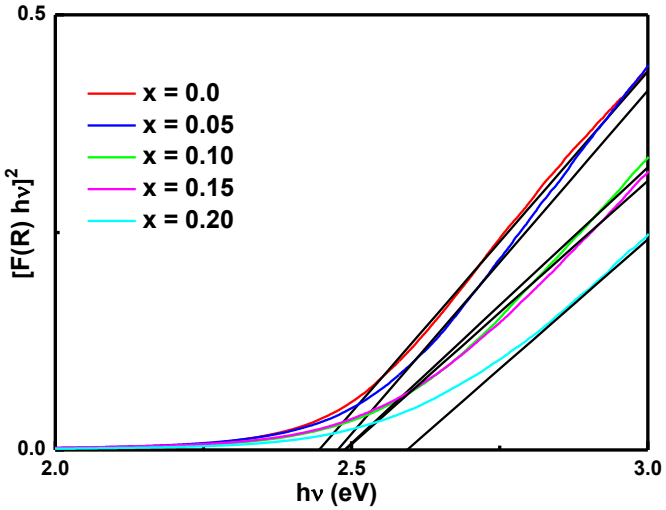

Figure 4.42 Graphical representation of the E_g values for quenched $Bi_4V_{2-x}ME_xO_{11-\delta}$ ($0.0 \leq x \leq 0.20$; ME = Ba^{2+}).

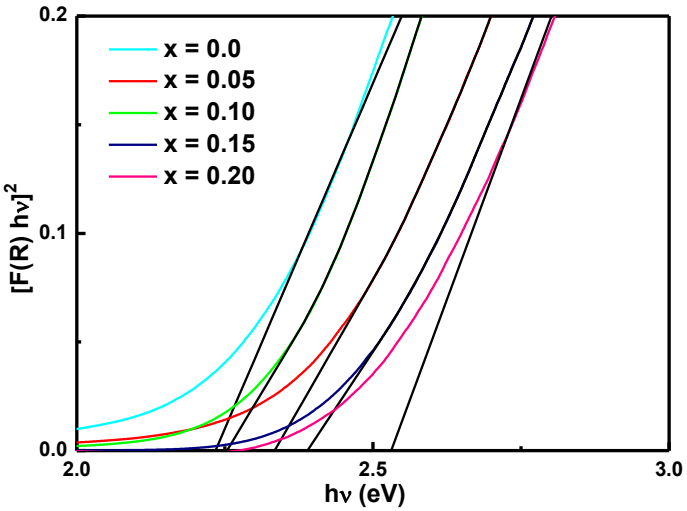

Figure 4.43 Graphical representation of the E_g values for sintered $Bi_4V_{2-x}ME_xO_{11-\delta}$ ($0.0 \leq x \leq 0.20$; ME = Ba^{2+}).

The value of optical band gap decreases with the increase in concentration of dopant upto x = 0.10 for sintered samples. The change in optical band gap can be attributed to the structural changes due to the reduction of V and generation of oxide vacancies [85]. Additionally, there is a large electronegativity difference between Ba (0.9) and V (1.6). The large difference in

the electronegativity value between the host and dopant atom shifts valence band towards conduction band. Also, the presence of defects decreases the optical band gap [86, 29].

Table 4.19 Values of optical band gap and Urbach energy for quenched and sintered $Bi_4V_{2-x}ME_xO_{11-\delta}$ ($0.0 \leq x \leq 0.20$; ME = Ba^{2+}).

	As quenched samples		Sintered samples	
Composition	**E_g (eV)**	**ΔE (eV)**	**E_g (eV)**	**ΔE (eV)**
$Bi_4V_2O_{11-\delta}$	2.45	0.41	2.27	0.56
$Bi_4V_{1.95}Ba_{0.05}O_{11-\delta}$	2.34	0.36	2.12	0.35
$Bi_4V_{1.90}Ba_{0.10}O_{11-\delta}$	2.33	0.33	2.03	0.23
$Bi_4V_{1.85}Ba_{0.15}O_{11-\delta}$	2.32	0.33	2.14	0.19
$Bi_4V_{1.80}Ba_{0.20}O_{11-\delta}$	2.39	0.32	2.37	0.22

4.5 Effect of sintering temperature

As discussed above, $Bi_4V_{1.85}Ba_{0.15}O_{11-\delta}$ is γ- phase stabilized, highly thermally stabilized, representing the lowest activation energy. Since, it has been reported by various researchers that sintering temperature has large effect on the properties of BIMEVOX system. So, in order to study the effect of sintering temperature; the sintering of quenched $Bi_4V_{1.85}Ba_{0.15}O_{11-\delta}$ sample was also performed at 700 and 750 °C for 12 h. XRD analysis on the samples sintered at 700 and 750 °C revealed the presence of γ- phase in all the samples with space group *I4/mmm* except sample sintered at 700 °C. The sample sintered at 700 °C is observed to represent the β- phase with space group *Amam*. The rietveld refined patterns are shown in Figure 4.44. All the refined lattice parameters along with goodness of fitting parameters are listed in Table 4.20.

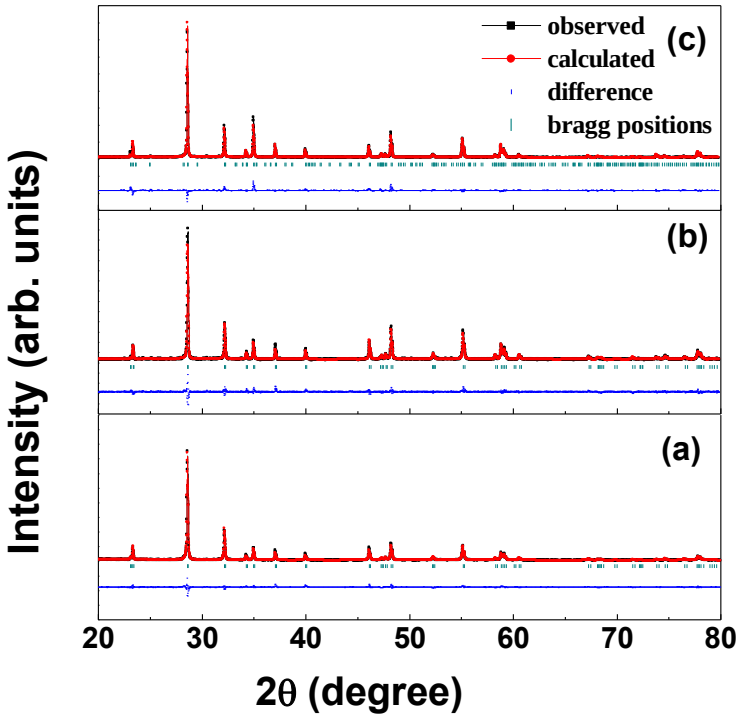

Figure 4.44 XRD patterns for $Bi_4V_{1.85}Ba_{0.15}O_{11-\delta}$ sintered sample at (a) 800, (b) 750 and (c) 700 °C.

Table 4.20 Rietveld refined parameters and density for $Bi_4V_{1.85}Ba_{0.15}O_{11-\delta}$ sintered at 700, 750 and 800 °C.

Lattice parameters					Goodness parameters of fitting		Density ($g\ cm^{-3}$)
Sintering temperature	**a (Å)**	**b (Å)**	**c (Å)**	**Volume ($Å^3$)**	**R_{exp}**	**χ^2**	
700 °C	11.133	5.569	15.397	954.718	4.99	3.36	6.73
750 °C	3.933	3.933	15.394	238.172	6.55	2.07	7.23
800 °C	3.935	3.935	15.391	238.333	8.40	1.40	7.43

The comparison of lattice parameters of samples sintered at different temperatures shows the decrease in lattice parameter 'c' with the increase in sintering temperature. Thus, it can be said that number of oxygen vacancies increase with the increase in sintering temperature due to higher possibility of reduction of V^{5+} to V^{4+}.

From the analysis of FTIR spectra of all the samples it is clear that all the bands corresponding to bismuth vanadate system are present. There is slight shift in the bands towards higher wavenumber side with the decrease in sintering temperature. It is observed that with decrease in sintering temperature, the conductivity value increases at lower temperature and decreases at higher temperature as compared to a similar sample, heat treated at 800 °C. The increase in conductivity at lower temperature might be related to the decrease in grain size as shown in SEM micrograph (Figure 4.45 (a)). Similar results have been reported by various researchers [87, 88]. However, at higher temperature the trend of conductivity can be explained on the basis of density. As at higher temperatures, the effect of processing conditions diminishes [89]. The higher values of conductivity of the sample sintered at 800 °C at higher temperature can be related to the higher density, lower porosity and well-connected grains (Table 4.20). In addition to this, $\gamma' \leftrightarrow \gamma$ phase transition largely

affects the conductivity above its transition temperature. For the sample sintered at 800 °C, the γ′ ↔ γ transformation takes place at higher temperature, stabilizing γ- phase for wider temperature range.

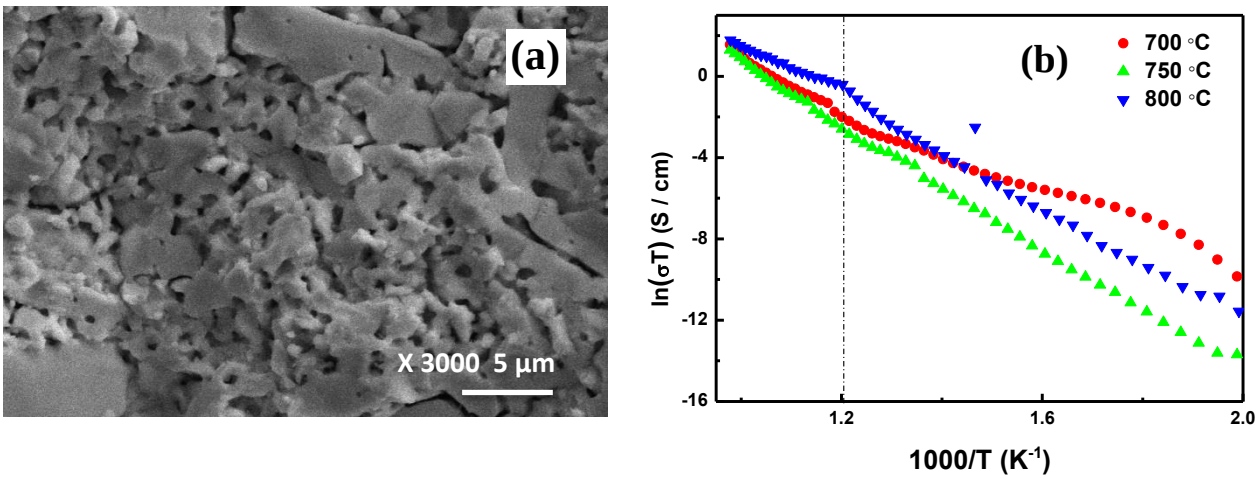

Figure 4.45 (a) Scanning electron micrograph for $Bi_4V_{1.85}Ba_{0.15}O_{11-\delta}$ sintered at 700 °C and (b) Arrhenius plot for $Bi_4V_{1.85}Ba_{0.15}O_{11-\delta}$ sintered at 700, 750 and 800 °C.

For all the doped samples γ- phase is stabilized at room temperature irrespective of dopants except $Bi_4V_{1.95}Ba_{0.05}O_{11-\delta}$ sample. With the sintering of as quenched samples at 800 °C for 12 hours, the γ- phase converts to β- phase in lower dopant concentration samples. In most of the cases for $x \geq 0.10$ γ- phase remains intact and does not convert to β- phase after sintering. During sintering liquid phase sintering has taken place in all the samples. The grain size variation with dopant concentration is observed. However, the grain size decreases in Sr^{2+} and Ba^{2+} doped samples as compared to undoped sample. The activation energy indicates that the present samples are predominantly ionic conductors. The higher ionic radii difference between host and dopant atom leads to the lower grain growth of the grains. TECs of doped samples are observed to be on higher side as compared to undoped sample.

References

1. I. Abrahams, F. Krok, J.A.G. Nelstrop, Solid State Ionics 90 (1996) 57.
2. R.N. Vannier, E. Pernot, M. Anne, O. Isnard, G. Nowogrocki, G. Mairesse, Solid State Ionics 157 (2003) 147.
3. F. Krok, I. Abrahams, M. Malys, W. Bogusz, J.R. Dygas, J.A.G. Nelstrop, A.J. Bush, Solid State Ionics 136-137 (2000) 119.
4. S. Beg, S. Hafeez, N.A.S. Al-Areqi, Physica B 405 (2010) 4370.
5. M.C. Steil, F. Ratajczak, E. Capoen, C. Pirovano, R.N. Vannier, G. Mairesse, Solid State Ionics 176 (2005) 2305.
6. R. Kant, K. Singh, O. P. Pandey, Ionics 15 (2009) 567.
7. I. Abrahams, A.J. Bush, F. Krok, G.E. Hawkes, K.D. Sales, P. Thorton, W. Bogusz, J. Mater. Chem. 8 (5) (1998) 1213.
8. F. Snchez-Bajo, F.L. Cumbrera, J. Appl. Cryst. 30 (1997) 427.
9. R.N. Vannier, G. Mairesse, F.A. Abraham, G. Nowogrocki, Solid State Ionics, 80 (1995) 11.
10. I. Abrahams, F. Krok, J. Mater. Chem. 12 (2002) 3351.
11. I. Abrahams, F. Krok, M. Malys, W. Wrobel, Solid State Ionics 176 (2005) 2053.
12. E.D. Politova, G.M. Kaleva, A.V. Mosunov, M.G. Safroneko, N.U. Venskovskii, Solid State Ionics 192 (2011) 248.
13. O. Joubert, A. Jouanneaux, M. Ganne, R.N. Vannier, G. Mairesse, Solid State Ionics 73 (1994) 309.
14. S.N. Achary, M.D. Mathews, S.J. Patwe, A.K. Tyagi, J. Mat. Sci. Lett. 18 (1999) 355.
15. R.N. Vannier, G. Mariresse, F. Abraham, G. Nowogrocki, J. Solid State Chem. 103. (1993) 441.
16. N.A.S. Areqi, S. Beg, Mater. Chem. Phys. 115 (2009) 5.

17. M. Malys, F. Krok, I. Abrahams, W. Wrobel, A. Kozanecka, J.L. Nowinski, W. Bogusz, J. R. Dygas, Phys. Stat. Sol. (A) 2 (2003) 357.
18. G.K. Williamson, W.H. Hall, Acta Metall. 1 (1953) 22.
19. M. Karolus, E. Lagiewka, J. Alloys Compd. 367 (2004) 235.
20. H. Mandar, T. Uustare, J. Aarik, A. Tarre, A. Rosental, Thin Solid Films 515 (2007) 4570.
21. S. Thakur, O.P. Pandey, K. Singh, J. Mol. Struct. 1074 (2014) 186.
22. C. Tripon, D. Toloman, M. Aluas, C. Filip, J. Ardelean, J. Optoelectron. Adv. M. 8 (3) (2006) 1129.
23. V. Dimitrov, Y. Dimitriev, A. Montenero, J. Non- Cryst. Solids 180 (1994) 51.
24. I. Ardelean, D. Rusu, J. Optoelectron. Adv. M. 10 (1) (2008) 66.
25. T.K. Patil, M.I. Talele, J. Nano- Electron. Phys. 4 (4) (2012) 040031.
26. D. Sun, X. Jin, H. Liu, J. Zhu, Y. Zhu, Y. Zhu, Ferroelectrics 355 (2007) 145.
27. G. Kaur, M. Kumar, A. Arora, O.P. Pandey, K. Singh, J. Non-Cryst. Solids 357 (2011) 858.
28. E.S. Buyanova, M.V. Morozova, J.V. Emelyanova, S.A. Petrova, R.G. Zhakharov, N.V. Tarakina, V.M. Zhukovskiy, Solid State Ionics 243 (2013) 8.
29. S. Thakur, M. Devi, K. Singh, Ionics 268 A (2014) 23.
30. G. Kaur, O.P. Pandey, K. Singh, Phys. Status Solidi A 209 (7) (2012) 1231.
31. T. Badapanda, V. Senthil, S.K. Rout, L.S. Cavalcante, A.Z., Simoes, T.P. Sinha, S. Panigrahi, M.M. de Jesus, E. Longo, J.A. Varela, Curr. Appl. Phy. 11 (2011) 1282.
32. B. Parija, S.K. Rout, L.S. Cavalcante, A.Z. Simoes, S. Panigrahi, E. Longo, N.C. Batista, Appl. Phys. A 109 (2012) 715.
33. O. Joubert, A. Jouanneaux, M. Ganne, Mater. Res. Bull. 2 (1994) 175.

34. R.N. Vannier, G. Mairesse, F. Abraham, G. Nowogrocki, E. Pernot, M. Anne, M. Bachmann, P. Strobel, J. Fouletier, Solid State Ionics 78 (1995) 183.
35. F. Abraham, M.F. Debreuille-Gresse, G. Mairesse, G. Nowogrocki, Solid State Ionics 28-30 (1988) 529.
36. C.K. Lee, C.S. Ong, Solid State Ionics 117 (1999) 301.
37. R.H. Piva, D.H. Piva, J. Venturini, R. Florianoc, M.R. Morelli, Ceram. Int. 41 (1) (2015) 171.
38. Jeong-Pyo Kim, Sung-II Jung, Young-Suk Sim, Yeon-Gil Jung, J. Korean Phy. Soc. 54 (3) (2009) 1172.
39. R.K. Lenka, T. Mahata, A.K. Tyagi, P.K. Sinha, Solid State Ionics 181 (2010) 262.
40. M.V. Morozova, E.S. Buyanova, J.V. Emelyanova, V.M. Zhukovskiy, S.A. Petrova, Solid State Ionics 192 (2011) 153.
41. S. Yilmaz, O. Turkoglu, M. Ari, I. Belenli, Ceramica 57 (2011) 185.
42. X.-Li Xia, Z.-G. Liu, J.-Hu Ouyang, Solid State Ionics 196 (2011) 1840.
43. S. Thakur, O.P. Pandey, K. Singh, Ceram. Int. 39 (2013) 6165.
44. G.H. Cartledge, J. Am. Chem. Soc. 50 (1928) 2855.
45. V. Sharma, A.K. Shukla, J. Gopalakrishnana, Solid State Ionics 58 (1992) 359.
46. C. Pirvano, M. C. Steil, E. Capoen, G. Nowogrocki, R.N. Vannier, Solid State Ionics 176 (2005) 2079.
47. M. Guillodo, J. Fouletier, L. Dessemond, P.D. Gallo, J. Eur. Ceram. Soc. 21 (2001) 2331.
48. V. Thakral, S. Uma, Mat. Res. Bull. 45 (2010) 1250.
49. S. Beg, S. Hafeez, N.A.S. Al-Areqi, Phase Transitions 83 (3) (2010) 169.
50. J.A. Dean, Lange's Handbook of Chemistry, thirteenth ed., Mc Graw-Hill Co. (1985) 3.

51. R. Kant, K. Singh, O.P. Pandey, Mater. Sci. Eng. B 158 (2009) 63.
52. O. Joubert, M. Ganne, R.N. Vannier, G. Mairesse, Solid State Ionics 83 (1996) 199.
53. S. Thakur, O.P. Pandey, K. Singh, Solid State Ionics 268 (2014) 23.
54. M. Guillodo, J. Fouletier, L. Dessemond, P.D. Gallo, Electrochim. Acta 47 (2002) 2809.
55. S. Beg, A. Al-Alas, N.A.S. Al-Areqi, J. Phys. Chem. Solids 71 (2010) 1421.
56. F. Krok, I. Abraham, D.G. Bangobango, W. Bogusz, J.A.G. Nelstrop, Solid State Ionics 86-88 (1996) 261.
57. E.D. Politova, E.A. Fortal'nova, G.M. Kaleva, A.V. Mosunov, L.I. Andronova, S.A. Andropova, M.G. Safronenko, N.U. Venskovskii, Phys. Solid State 51 (7) (2009) 1443.
58. I. Abrahams, F. Krok, M. Malys, A.J. Bush, J. Mat. Sci. 36 (2001) 1099.
59. R. Kant, K. Singh, O.P. Pandey, Int. J. Hydrogen Energ. 33 (2008) 455.
60. R.N. Vannier, G. Mairesse, F. Abraham, G. Nowogrocki, Solid State Ionics 70-71 (1994) 248.
61. Deepti, R. Kant, M.L. Singla, K. Singh, Curr. Appl. Phys. 9 (2009) 1467.
62. F. Abrahams, J.C. Boivin, G. Mairesse, G. Nowogrocki, Solid State Ionics 40-41 (1990) 934.
63. V.A.M. Brabers, Spectrochimica Acta 32 A (1976) 1709.
64. M.C. Steil, J. Fouletier, M. Kleitza, P. Labrune, J. Europ. Ceram. Soc. 19 (1999) 815.
65. S.B.R.S. Adnan, N.S. Mohamed, Electrochim. Acta 146 (2014) 598.
66. K. Shantha, K.B.R. Varma, J. Mater. Chem. 7 (8) (1997) 1565.
67. K.V.R. Prasad, A.R. Raju, K.B.R. Varma, J. Mat. Sci. 29 (1994) 2691.
68. S. Sindhu, S. Sanghi, A. Agarwal, V.P. Seth, N. Kishore, Mat. Chem. Phy. 90 (2005) 83.

69. B. Tirloni, E.S. Lang, G.M. de Olivira, Polyhedron 62 (2013) 126.

70. V. Kumar, A. Sharma, D.K. Sharma, D.K. Dwivedi, Optik 125 (2014) 1209.

71. V.M. Zainullina, V.M. Zhukovskii, E.S. Buyanova, Y.V. Emel'yanova, Russ. J. Electrochem. 52 (2) (2007) 225.

72. Y.-K. Taninouchi, T. Uda, T. Ichitsubo, Y. Awakura, E. Matsubara, Solid State Ionics 181 (2010) 719.

73. R.N. Vannier, G. Mairesse, G. Nowogrocki, F. Abraham, J. C. Boivin, Solid State Ionics 53-56 (1992) 713.

74. M.H. Paydar, A.M. Hadian, G. Fafilek, J. Mat. Sci. 39 (2004) 1357.

75. J. Yan, M. Greenblat, Solid State Ionics 81 (1995) 225.

76. D. Hassan, S. Janes, R. Clasen, J. Eur. Ceram. Soc. 23 (2003) 221.

77. Z.-G. Liu, J.-H. Ouyang, Y. Zhou, X.-L. Xia, J. Power Sources 185 (2008) 876.

78. J.K. Gill, O.P. Pandey, K. Singh, Solid State Sci. 13 (2011) 1960.

79. R. Nelson, M.H. Weatherspoon, J. Gomez, E.E. Kalu, J.P. Jheng, Electrochem. Comm. 34 (2013) 77.

80. Z.-G. Liu, J.-H. Ouyang, X.-L. Xia, J. Power Sources 195 (2010) 3261.

81. Y.V. Emel'yanova, Z.V. Salimgareeva, E.S. Buyanova, V.M. Zhukovskii, Inorg. Mater. 41 (10) (2005) 1107.

82. I. Abrahams, F. Krok, J. Mater Chem. 12 (2002) 2260.

83. C.K. Lee, A.R. West, Solid State Ionics 86-88 (1996) 235.

84. I. Pal, A. Agarwal, S. Sanghi, Indian J. Pure Appl. Phys. 50 (2012) 237.

85. C.J. Watson, A. Coats, D.C. Sinclair, J. Mater. Chem. 7 (1997) 2091.

86. F.P. Koffyberg, J. Phys. Chem. Solids 53 (10) (1992) 1285.

87. E.A. Fortalnova, V.V. Murasheva, M.G. Safronenko, N.U. Venskovskii, G.M. Kaleva, E.D. Politova, Russ. J. Phys. Chem. 82 (10) (2008) 1633.

88. N.V. Lyskov, Y.G. Metlin, V.V. Belousov, Y.D. Tretyakov Russ. J. Electrochem. 41 (5) (2005) 522.

89. W. Jibo, B. Ji, X. Zhu, Y. Cong, W. Yang, Chinese J. Catalysis 30 (9) (2009) 926.

Chapter 5
Conclusions and future scope

5.1 Conclusions

In the present study, undoped and alkaline earth metals (ME= Mg^{2+}, Ca^{2+}, Sr^{2+} and Ba^{2+}) doped $Bi_4V_{2-x}ME_xO_{11-\delta}$ ($0.0 \leq x \leq 0.20$) have been synthesized by melt quench technique followed by sintering at different temperatures for 12 hours in air. The structural, thermal, optical and electrical properties of $Bi_4V_{2-x}ME_xO_{11-\delta}$ ($0.0 \leq x \leq 0.20$; ME= Mg^{2+}, Ca^{2+}, Sr^{2+} and Ba^{2+}) have been studied using various techniques. The results are discussed in the light of disorder, oxygen vacancies as well as their correlation with microstructural changes with dopants. Following conclusions have been drawn from present study.

The X-ray diffraction analysis of all the doped quenched samples revealed the presence of γ-phase except sample $Bi_4V_{1.95}Ba_{0.05}O_{11-\delta}$. In $Bi_4V_{1.95}Ba_{0.05}O_{11-\delta}$ sample α- phase has been observed. Furthermore, the stabilization of these phases is confirmed with rietveld refinement. Sintering of quenched samples led to conversion of γ- phase to ordered β- phase, particularly at lower concentration of dopants. The conversion of γ- phase to ordered phase β-phase is observed for x = 0.05, 0.10 and 0.20; ME = Mg^{2+} and x = 0.05; ME = Sr^{2+}. It has been observed that for x = 0.15 composition, γ- phase is stabilized for all the doped samples. Higher difference between ionic radii of dopants and host atom increase the chance of γ-phase stabilization for wider range of dopant concentration. The relative density of all the sintered samples is found to be > 90% which is good for conductivity. The highest relative density of ~ 96% is obtained for $Bi_4V_{2-x}Ba_xO_{11-\delta,}$ for x = 0.15 composition among all the dopants.

Blue shift in Fourier transform infrared (FTIR) spectra is observed in sintered samples as compared to quenched samples. FTIR bands have become sharper in case of sintered samples. The broadening in quenched samples can be attributed to the total number of absorption bands generated due to the variations of bond angles and bond lengths. For quenched as well as sintered samples, the bands at ~ 615 and ~ 912 cm^{-1} start disappearing

with increase in dopant, indicating of the incorporation of dopant in VO_4 polyhedrons. In other words, the different dopants only affect the perovskite layer i.e. $[V_2O_4]^{2-}$ in the present system. Thermal expansion coefficient of all the samples was calculated and the highest TEC was observed for quenched $Bi_4V_{1.85}Ca_{0.15}O_{11-\delta}$ ~ 10.6 × 10^{-6} / °C. For sintered samples the highest TEC is ~ 9.7 × 10^{-6} / °C for $Bi_4V_{1.95}Mg_{0.05}O_{11-\delta}$ sample.

The negligible weight loss is observed for all the samples. However, the minimum weight loss is observed for $Bi_4V_{1.85}Ba_{0.15}O_{11-\delta}$ sample amongst all the samples. Decrease in grain size is observed with the increase in amount of dopant except for Sr^{2+} dopant. This implies that all of the dopants are acting as grain growth inhibitor in the system except Sr^{2+} dopant. For Sr^{2+} dopant increase in grain size is observed with the increasing amount of dopant. Furthermore, this correlates well with the increase in conductivity with increasing dopant concentration.

In intermediate temperature ranges, the conductivity of all the doped samples is higher than that of undoped sample. However, at higher temperature, it decreases for some samples due to ordering/ clustering in oxygen vacancies. For all the dopants, the increase in conductivity upto a certain concentration with increase in amount of dopant is observed. But for Sr^{2+} dopant, the increase in conductivity is observed for all the dopant concentrations. The decrease in conductivity upon increasing dopant concentration can be related to the decrease in grain size and increase in amount of grain boundaries which may inhibit the hopping of ions (except for Sr^{2+} dopant). Additionally, oxygen ordering is also responsible for lower conductivity in higher doped samples. The lowest activation energy; E_a is observed for $Bi_4V_{1.85}Ba_{0.15}O_{11-\delta}$ sample ~ 0.70 eV in the temperature range 570-750 °C. Whereas, the highest conductivity is observed for $Bi_4V_{1.90}Mg_{0.10}O_{11-\delta}$ ~ 13.7 × 10^{-3} Scm^{-1} at 700 °C. The x = 0.15 and 0.20, ME = Ca^{2+} samples could not show any $\gamma \rightarrow \gamma'$ phase transition. The optical band gap of all the samples is observed in the semiconducting range. For sintered samples the

lower values of optical band gap and Urbach energy than quenched samples are obtained. The reflectance of doped samples is higher than that of undoped sample.

Since, $Bi_4V_{1.85}Ba_{0.15}O_{11-\delta}$ represents the best phase stability and least activation energy. So, further temperature variation study has been carried out on this sample. The lowering in sintering temperature decreases the grain size, increases the porosity as well as conductivity at lower temperatures. The best conductivity is observed for the sample sintered at 800 °C in higher temperature conductivity regime (600- 750 °C).

5.2 Future Scope

After concluding the present work, it can be suggested that efforts are required for the optimization of synthesis technique in order to obtain high conductivity and thermal stability. High temperature X- ray can also be performed to investigate the various phase transformations occurring in the system. The performance of developed electrolytes can also be checked in actual configuration of SOFCs to achieve long term uninterrupted performance goals.